Modeling particle growth by condensation and deposition in turbulent mixed-phase cloud volumes

A doctoral dissertation by

Daniel G. Albuquerque

Supervisor: **Prof. Dr. Hab. Hanna Pawłowska**
Institute of Geophysics, Faculty of Physics, University of Warsaw

Co-supervisor: **Dr. Gustavo C. Abade**
Institute of Geophysics, Faculty of Physics, University of Warsaw

UNIVERSITY OF WARSAW

University of Warsaw

Warsaw 2025

to all my teachers

Acknowledgements

I would like to express my deepest gratitude to all the teachers, colleagues, and staff I have met at the Institute of Geophysics during this journey. The knowledge and passion you shared have been a constant source of inspiration throughout my doctoral work. Each lecture, discussion, and piece of advice helped shape my scientific perspective, and I feel privileged to have learned in such an environment.

Among them, I am especially indebted to Prof. Dr. Hanna Pawłowska and Dr. Gustavo Abade. Their scientific guidance has been a crucial and invaluable support. I sincerely thank Prof. Hanna for welcoming into the Geophysics Institute and making sure I always had all the necessary resources to carry on with my research activities. As for Dr. Abade, his extraordinary depth of knowledge, combined with a rare talent for conveying complex ideas in an eloquent and accessible way, has been a continual source of learning and admiration. He has always been there for me, not only in academic matters but also in those that extended far beyond research. I am profoundly grateful for his ability to see the *human being* behind the student, for his patience, and for the support he offered during challenging times. His example of kindness and humanity will remain with me as much as the scientific lessons I have received.

Finally, and most importantly, I would like to thank my wonderful wife, Livia. Words cannot fully express how vital her presence has been during these years. She has been my constant companion, offering unconditional love and unwavering support, even in the darkest of moments. Without her encouragement and patience, this work would not have been possible. Her devoted companionship has given me the strength to persevere, and I dedicate this achievement to *her*. I love you with all my heart. Thank you.

Statement of originality

I hereby declare that I have prepared this thesis without any unauthorised assistance from third parties and without using aids other than those explicitly indicated. To the best of my knowledge, all ideas and material taken directly or indirectly from other sources are properly acknowledged. This thesis has not been submitted previously, in whole or in part, for any other degree or professional qualification.

This work was carried out under the supervision of Prof. Dr. Hab. Hanna Pawłowska and Dr. Gustavo Coelho Abade and at the Institute of Geophysics, University of Warsaw.

Warsaw, 2025

Abstract

Mixed-phase clouds play a central role in the Earth's radiation budget and hydrological cycle, yet their microphysical evolution remains one of the largest sources of uncertainty in atmospheric modelling. A key difficulty arises from the interaction of turbulent fluctuations with nonlinear phase-change processes, such as the Wegener–Bergeron–Findeisen (WBF) mechanism, which are typically parameterised in large-scale models under the assumption of spatial homogeneity. A series of numerical and experimental studies suggest that neglecting subgrid fluctuations can lead to systematic biases, most notably an artificially rapid depletion of supercooled liquid water by the WBF process. At the same time, cloud measurement campaigns provide abundant observations of long-lived mixed-phase clouds that are rich in liquid water content.

This thesis develops and applies a stochastic Lagrangian parcel model to investigate the limitations of the mean-field assumption and to quantify the impact of turbulence on mixed-phase microphysics. In this framework, individual cloud droplets and ice crystals are embedded in a modelled turbulent environment, represented by Gaussian stochastic velocity fluctuations combined with a deterministic mixing model. For the purpose of representing the intrinsic heterogeneities of turbulent environments, each cloud particle carries forward its own independent history of velocity fluctuations, and is assumed to interact – growing by condensation and evaporating, while providing microphysical feedback – primarily with its immediate vicinity, with their thermodynamic and microphysical properties evolving according to fundamental conservation laws. Interactions with other particles are mediated through a modelled mixing mechanism characterised by a single timescale, tuned in accordance with inertial-range turbulence scaling laws.

Our model bridges the gap between overly simplified bulk schemes and computationally prohibitive direct numerical simulations, providing a framework of intermediate complexity within the cloud model hierarchy. By explicitly resolving subgrid-scale variability, the stochastic approach reveals extended persistence of liquid water, modified growth rates and activation of ice crystals, and a distinct supersaturation dynamics that traditional homogeneous parcel models are unable to reproduce. Although observed in an idealised framework, these effects prove robust across a range of initial conditions and turbulence intensities, indicating

that unresolved-scale turbulence might play an important role in the development of the microphysical state in mixed-phase clouds.

These results open clear opportunities for further model refinement and integration into larger-scale frameworks. Our approach allows for the replacement of the turbulent mixing model by more elaborate ones, while keeping the rest of the formulation unchanged. Most importantly, its ability to capture the impact of fluctuations on phase-change processes makes it a promising candidate for subgrid parameterisation in large-eddy simulations, where the representation of mixed-phase microphysics remains a major source of uncertainty. In this role, the present work provides both a physically grounded and computationally tractable route toward improving the fidelity of cloud models across scales.

Streszczenie

Chmury wielofazowe mają istotny udział w bilansie promieniowania Ziemi oraz w globalnym cyklu hydrologicznym, jednak ich rozwój na poziomie mikrofizycznym stanowi główne źródło niepewności w modelowaniu procesów atmosferycznych. Trudność wynika głównie z oddziaływania pomiędzy fluktuacjami turbulentnymi a procesami przemian fazowych o charakterze nieliniowym, takimi jak mechanizm Wegenera–Bergerona–Findeisena (WBF), które w modelach wielkoskalowych są zazwyczaj parametryzowane przy założeniu jednorodności przestrzennej. Wyniki licznych badań numerycznych i eksperymentalnych wskazują, że pomijanie fluktuacji o skalach mniejszych niż rozmiar siatki prowadzi do błędów systematycznych, w szczególności do sztucznie przyspieszonego zaniku przechłodzonej wody w wyniku procesu WBF. Jednocześnie pomiary dostarczają licznych obserwacji sprzecznych z powyższymi założeniami ukazując istnienie długo utrzymujących się chmur wielofazowych bogatych w wodę w stanie ciekłym.

W niniejszej rozprawie opracowano i zastosowano stochastyczny model parcelowy typu Lagrange'a, mający na celu zbadanie ograniczeń założenia o uśrednionym polu oraz ilościową ocenę wpływu turbulencji na mikrofizykę wielofazową. W tym podejściu pojedyncze krople wody i kryształy lodu są osadzone w modelowanym środowisku turbulentnym, które opisano jako połączenie gaussowskich, stochastycznych fluktuacji prędkości oraz deterministycznego modelu mieszania. W celu wiernego odwzorowania niejednorodności charakterystycznych dla środowiska turbulentnego, każdy element chmury zachowuje własną, niezależną historię fluktuacji prędkości i oddziałuje – poprzez wzrost na skutek kondensacji oraz parowanie utrzymując jednocześnie mikrofizyczne sprzężenie – przede wszystkim ze swoim najbliższym otoczeniem. Właściwości termodynamiczne i mikrofizyczne tych elementów podlegają przekształceniom zgodnym z podstawowymi prawami zachowania. Interakcje pomiędzy różnymi elementami są realizowane za pomocą modelowanego mechanizmu mieszania, opisanego pojedynczą skalą czasową, dobraną w oparciu o prawa skalowania obowiązujące w zakresie bezwładnościowym turbulencji

Opracowany model stanowi pomost pomiędzy nadmiernie uproszczonymi schematami zbiorczymi, a kosztownymi obliczeniowo symulacjami bezpośrednimi (DNS), oferując narzędzie do modelowania chmur o umiarkowanej złożoności. Dzięki jaw-

nemu odwzorowaniu zjawisk o skali mniejszej niż rozmiar siatki podejście stochastyczne pozwala zaobserwować zjawiska, których tradycyjne, jednorodne modele parcelowe nie są w stanie odtworzyć, takie jak wydłużona obecność przechłodzonej wody w stanie ciekłym, zmodyfikowane tempo wzrostu i aktywacji kryształów lodu, a także odmienna dynamika przesycenia. Choć wyniki te zostały uzyskane w ramach uproszczonego schematu, wykazują one odporność na zmiany warunków początkowych i intensywności turbulencji, co sugeruje, że turbulencja w mniejszej, nie modelowanej skali może odgrywać istotną rolę w rozwoju stanu mikrofizycznego chmur wielofazowych.

Uzyskane rezultaty otwierają nowe możliwości rozwoju modelu oraz jego integracji z wielkoskalowymi schematami. Zaproponowane podejście umożliwia zastąpienie obecnego modelu mieszania turbulentnego bardziej zaawansowanymi rozwiązaniami, przy jednoczesnym zachowaniu niezmienionej struktury pozostałych elementów modelu. Najważniejszą cechą opracowanej metody jest jej zdolność do uchwycenia wpływu fluktuacji na procesy przemian fazowych, co czyni ją obiecującym narzędziem do parametryzacji w skalach mniejszych niż rozmiar siatki w symulacjach metodą dużych wirów (LES) gdzie odwzorowanie mikrofizyki wielofazowej pozostaje jednym z głównych źródeł niepewności. W tym kontekście model przedstawiony w niniejszej pracy stanowi zarówno fizycznie ugruntowane, jak i obliczeniowo efektywne podejście, które może znacząco poprawić wierność odwzorowania modeli chmurowych w szerokim zakresie skal.

Contents

List of Figures

List of Tables

List of Symbols

Acronyms

CCN	cloud condensation nuclei
DNS	direct numerical simulation
DSD	droplet size distribution
GCM	general circulation model
INP	ice-nucleating particles
LCL	lifting condensation level
LEM	linear-eddy model
LES	large-eddy simulation
LWC	liquid water content
NWP	numerical weather prediction
PSD	particle size distribution
SDM	super-droplet method
SGS	subgrid-scale
SIP	secondary ice production
TKE	turbulent kinetic energy
WBF	Wegener–Bergeron–Findeisen process

Greek Symbols

Δ_ℓ	amount of water condensed during one simulation timestep [kg]
η_B	Batchelor length scale [m]
ϕ_i	ice particle fraction (N_i/N)
ρ_ℓ	density of liquid water [$\mathrm{kg\,m^{-3}}$]
ρ_d	density of dry air [$\mathrm{kg\,m^{-3}}$]
σ_{S_ℓ}	standard deviation of supersaturation with respect to liquid water (S_ℓ)
τ_Δ	eddy turnover time at scale Δ [s]
τ_ℓ	liquid-phase relaxation time [s]
τ_i	ice-phase relaxation time [s]
τ_m	characteristic mixing time scale for scalars (model parameter) [s]
τ_p	particle response time (inertial relaxation time of a particle) [s]
θ_c	condensed water potential temperature [K]
θ_v	virtual potential temperature [K]
φ_k	phase indicator for particle k (1 for liquid, 0 for ice)

Latin Symbols

$\mathbf{F}_h$ hydrodynamical drag force on a sphere immersed in Stokes flow [N]

$\mathbf{U}$ flow velocity vector [$\mathrm{m\,s^{-1}}$]

$\mathbf{V}$ particle velocity vector [$\mathrm{m\,s^{-1}}$]

$\mathcal{D}_\ell$ temperature-corrected vapour diffusivity for droplets [$\mathrm{m^2\,s^{-1}}$]

$\mathcal{D}_i$ temperature-corrected vapour diffusivity for ice particles [$\mathrm{m^2\,s^{-1}}$]

$\mathcal{D}_T$ thermal diffusivity of air [$\mathrm{m^2\,s^{-1}}$]

$\mathcal{D}_v$ diffusivity of water vapour in air [$\mathrm{m^2\,s^{-1}}$]

$\mathcal{R}_d$ specific gas constant for dry air [$\mathrm{J\,kg^{-1}\,K^{-1}}$]

$\mathcal{R}_v$ specific gas constant for water vapour [$\mathrm{J\,kg^{-1}\,K^{-1}}$]

C_τ scalar-to-velocity time scale ratio

c_p specific heat capacity at constant pressure (for dry air) [$\mathrm{J\,kg^{-1}\,K^{-1}}$]

e_ℓ saturation vapour pressure over liquid water [Pa]

e_i saturation vapour pressure over ice [Pa]

$e_{s,0}$ saturation vapour pressure at the triple point of water [Pa]

$e_{s,\ell}$ saturation vapour pressure with respect to liquid water [Pa]

$e_{s,i}$ saturation vapour pressure with respect to ice [Pa]

L_f latent heat of water fusion [$\mathrm{J\,kg^{-1}}$]

L_s latent heat of water sublimation [$\mathrm{J\,kg^{-1}}$]

L_v latent heat of water vaporization [$\mathrm{J\,kg^{-1}}$]

m_α mass of water in phase α (ice or liquid water)[kg]

M_d molar mass of dry air [$\mathrm{kg\,mol^{-1}}$]

m_d mass of dry air [kg]

m_k mass of condensate in the k-th super-droplet [kg]

N	total number of cloud particles in the adiabatic parcel
N_{sd}	number of super-droplets in the adiabatic parcel
Q_k	local water vapour mixing ratio for particle k
q_v	parcel-average water vapour mixing ratio (equivalent to $\langle Q_k \rangle$)
$q_{s,\ell}$	saturation mixing ratio with respect to liquid water
$q_{s,i}$	saturation mixing ratio with respect to ice
$q_{v,0}$	initial water vapour mixing ratio (at ground level)
r_α	parcel-average mixing ratio of phase α (ice or liquid water)
r_ℓ	parcel-average liquid water mixing ratio
R_c	critical droplet radius [m]
r_c	parcel-average total condensate mixing ratio
R_d	dry radius of aerosol [m]
r_i	parcel-average ice mixing ratio
R_k	radius of the k-th droplet/particle [m]
r_t	parcel-average total water mixing ratio (all three phases)
$R_{d,k}$	dry radius of the k-th aerosol particle [m]
R_{eq}	equilibrium droplet radius [m]
S_ℓ	supersaturation with respect to liquid water
S_c	critical supersaturation with respect to liquid water
S_i	supersaturation with respect to ice
$S_{\ell,eq}$	equilibrium supersaturation with respect to liquid water
$S_{\ell,k}$	local supersaturation with respect to liquid water for particle k
$S_{i,k}$	local supersaturation with respect to ice for particle k
T_∞	ambient far-field temperature [K]

T_f	freezing temperature of a droplet [K]
T_s	saturated parcel temperature after condensation [K]
T_v	virtual temperature [K]
U_Δ	characteristic eddy velocity at scale Δ [$\mathrm{m\,s^{-1}}$]
v_s	particle's terminal sedimentation velocity [$\mathrm{m\,s^{-1}}$]
W_k	Wiener process for particle k [$\mathrm{s^{-1/2}}$]
w_k	vertical velocity component of particle k [$\mathrm{m\,s^{-1}}$]
z_k	vertical position of particle k [m]

1

Introduction

1.1 Problem statement

Clouds play a central role in regulating Earth's climate. By modulating the planetary albedo and exerting a strong influence on the longwave radiation budget, they contribute substantially to the uncertainty in estimates of climate sensitivity. In recognition of this, the *Fifth Assessment Report of the Intergovernmental Panel on Climate Change* (IPCC AR5) devotes an entire chapter to clouds and aerosols, highlighting their dominant role in shaping climate forcing. In particular, it stresses that cloud feedback remain the largest single source of uncertainty in model projections of climate change (Boucher et al., 2013). Despite decades of research, accurately quantifying the climatic role of clouds has proven elusive because their properties depend on non-linear interactions between microphysical, dynamical, and radiative processes that span a wide range of spatial and temporal scales.

This difficulty is reflected in the limitations of current climate models. **?** posed the provocative question "What are climate models missing?", arguing that the inability to represent critical cloud processes undermines the credibility of climate sensitivity estimates. They contend that progress in climate modelling will remain constrained until the representation of clouds, and their coupling with dynamics and radiation, is significantly improved. Among cloud types, mixed-phase clouds have emerged as especially important in this context, both for their radiative effects and for the difficulties they pose to models.

Mixed-phase clouds, which consist of supercooled liquid droplets coexisting with ice crystals, are particularly common in high-latitude regions and over the Southern Ocean. Their thermodynamic phase composition exerts a strong control on shortwave reflection and hence on Earth's energy balance. Because ice particles are generally larger and less reflective than liquid droplets, even modest changes in liquid fraction can substantially alter cloud albedo. Storelvmo (2017) reviews aerosol–cloud–climate interactions, underscoring that mixed-phase and ice clouds are at least as susceptible to aerosol perturbations as warm clouds, but remain far less understood. She highlights that aerosols acting as ice nuclei can dramatically shift phase partitioning, thereby altering cloud lifetime and radiative properties, yet current models capture these processes poorly. This makes mixed-phase clouds a "new frontier" in constraining aerosol effects on climate.

Observational evidence confirms the climatic importance of persistent supercooled liquid in mixed-phase clouds. Tan et al. (2016) analysed satellite retrievals and found that climate models systematically underestimate the fraction of supercooled liquid water in mixed-phase regimes. Their results show that when constrained by observations, mixed-phase clouds imply a stronger positive shortwave feedback, which translates into a higher equilibrium climate sensitivity. This suggests that longstanding model biases in phase partitioning have direct implications for projections of future warming. In other words, the degree to which models allow supercooled liquid to persist strongly influences their climate sensitivity estimates.

Despite these findings, many models continue to misrepresent the persistence of liquid in mixed-phase conditions. Cesana et al. (2012) used CALIPSO lidar observations to document the ubiquity of low-level liquid-containing Arctic clouds. When these data were compared against climate models, it became evident that models often glaciate such clouds too rapidly, producing ice-dominated states inconsistent with observations. This glaciation rate bias leads to deficiencies in simulated radiative fluxes at the surface and contributes to systematic errors in modelled Arctic climate feedbacks.

A similar picture emerges from the Southern Ocean. Furtado (2018) provides a detailed analysis of how mixed-phase clouds are parametrized in general circulation models. He shows that deficiencies in representing subgrid processes, such as the balance between turbulent variability and microphysical sinks of liquid water, lead to rapid dissipation of mixed-phase layers. The consequence is a lack of supercooled liquid, which causes insufficient shortwave reflection and biases in surface heat fluxes. In coupled models, this bias contributes to longstanding errors in sea surface temperature and sea-ice extent across the Southern Hemisphere. Most importantly, Furtado demonstrates that incorporating more physically-based subgrid treatments of mixed-phase microphysics can substantially reduce these biases, pointing the way towards model improvement. Observational studies further highlight the magnitude of this problem. McCoy et al. (2014) reconstructed shortwave reflection over the Southern Ocean from an integrated satellite dataset, showing that cloud albedo is highly sensitive to the partitioning between liquid and ice.

Their work demonstrates that seasonal variations in liquid fraction explain much of the observed variability in shortwave reflection, providing a benchmark against which models can be evaluated. Taken together, Cesana et al. (2012), Furtado (2018), and McCoy et al. (2014) reveal a consistent story: models underrepresent supercooled liquid, overpredict glaciation, and consequently underestimate the reflective power of mixed-phase clouds.

Mixed-phase clouds are both climatically significant and especially problematic, as their radiative impact depends on the persistence of supercooled liquid. Observations (Tan et al. (2016); Cesana et al. (2012); McCoy et al. (2014)) show that liquid persists far more often than models allow, and reviews (Storelvmo (2017); Boucher et al. (2013)) confirm that this misrepresentation contributes to the largest source of uncertainty in climate projections. Modelling studies Furtado (2018) identify the subgrid microphysical assumptions responsible for rapid glaciation and show that improvements are possible. As emphasized by **?**, until cloud processes such as these are captured with greater fidelity, climate sensitivity estimates will remain highly uncertain.

The persistent bias towards excessive glaciation is therefore not just a technical deficiency, but *a fundamental barrier to credible climate prediction*. Addressing this problem requires approaches that represent the turbulent variability and stochasticity that govern cloud microphysics at unresolved scales. It is within this broader context that the present work situates itself.

1.2 Existing approaches and their limitations

1.2.1 Mean-Field Models and the WBF Mechanism

Early studies of mixed-phase cloud microphysics relied on mean-field (spatially homogeneous) parcel models to describe phase changes. In such models, all cloud particles experience the same average conditions (temperature, supersaturation, etc.), which enabled analytical descriptions of fundamental processes but imposed severe simplifications. A cornerstone of these models is the Wegener–Bergeron–Findeisen (WBF) process, named after Wegener (1911), Bergeron (1935), and Findeisen (1938). The WBF mechanism describes how ice crystals grow rapidly at the expense of supercooled liquid droplets when both phases coexist in a closed, unchanging environment. This occurs because the saturation vapour pressure over liquid water is higher than that over ice at the same subfreezing temperature, making an environment that is subsaturated for liquid but still supersaturated for ice. Under those conditions, water vapour preferentially deposits onto ice crystals while adjacent droplets evaporate, eventually repartitioning all water into the ice phase. Classical theory thus predicts that a mixed-phase cloud in static conditions will inevitably glaciate: the liquid droplets completely evaporate, leaving only ice and vapour. This WBF process has long been considered the primary pathway for precipitation formation and glaciation in mixed-phase clouds.

However, the mean-field assumption leads to a simplified view that struggles to reconcile with atmospheric observations. In situ studies show that mixed-phase cloud layers can persist much longer than mean-field models would suggest. For example, parcel-model calculations indicate that a stratiform cloud with moderate ice crystal concentrations ($10^2 - 10^3 L^{-1}$) and modest liquid water content ($< 0.5 gm^{-3}$) should completely glaciate via the WBF mechanism within on the order of 20–40 minutes. In reality, extensive observations (including in Arctic stratocumulus) have found supercooled liquid layers enduring for many hours or even days under apparently steady conditions [e.g. Shupe et al. (2006); Fridlind et al. (2012); Zhang et al. (2018)]. This disparity highlights a key limitation of the mean-field approach: it ignores the dynamical and spatial heterogeneity present in real clouds. Mean-field models effectively overestimate the efficiency of WBF-driven glaciation by assuming perfectly uniform conditions. Consequently, the classic homogeneous parcel model cannot represent scenarios where some regions of grid box remain liquid while others glaciate. It lacks the ability to capture local fluctuations that can sustain liquid water pockets. As a result, traditional models predict far more rapid and complete glaciation than nature often produces.

In summary, the classical mean-field paradigm – built on the WBF process and spatially averaged conditions – established important baseline mechanisms for mixed-phase cloud evolution, but it tends to over-glaciate clouds and cannot explain the longevity and coexistence of liquid and ice observed in real clouds. These discrepancies motivated the development of dynamical criteria and stochastic approaches, as discussed next.

1.2.2 Dynamical Criteria for Mixed-Phase Cloud Persistence

One fundamental consequence of the mean-field assumption is an extreme sensitivity of cloud phase evolution to the large-scale ascent rate. In a uniform updraught, strong cooling can replenish supersaturation and delay the onset of WBF glaciation, whereas a weak updraught allows ice to consume the available vapour quickly, inhibiting liquid growth. Heymsfield (1977) was among the first to argue that a sufficiently strong updraught could maintain a cloud in a mixed-phase state that would otherwise collapse to an all-ice state. He showed that there exists a minimum updraught speed below which supercooled droplets cannot be sustained in an ice-containing cloud parcel.

Building on early insights by Heymsfield (1977), Korolev and Mazin (2003) derived an analytical condition for the critical updraught velocity needed to sustain liquid water in a rising parcel that already contains ice. In essence, a threshold vertical velocity above which adiabatic cooling can continually replenish water vapour faster than ice crystals deplete it. Below this threshold, any mixed-phase volume would eventually lose all liquid to the growing ice crystals; above it, droplets would keep forming and surviving alongside ice. Korolev and Field (2008) expanded this framework by formally defining two necessary conditions for persistent mixed-phase clouds: (1) the cloud parcel's upward velocity must exceed a minimum value to activate and sustain liquid droplets, and (2) the parcel must reach a sufficient altitude for droplet activation to occur in the first place. Only when both conditions are met can a long-lived mixed-phase equilibrium be achieved. In the same study, Korolev and Field (2008) demonstrate through parcel simulations that if an ice-containing air parcel experiences sustained oscillations or turbulence, it can repeatedly regenerate liquid water and reach a statistically steady mixed-phase state. They did not assume the cloud was in steady-state equilibrium initially. Instead, they showed that non-steady (time-dependent) evolution can lead to a new equilibrium where neither phase overtakes the other. This suggested that real mixed-phase clouds might self-regulate into a long-lived configuration if dynamical forcing continuously perturbs the system. Korolev and Field proposed analogous threshold conditions – in terms of minimum amplitude and frequency – for the motion of a parcel, as an attempt to explain mixed-phase persistence in vertically oscillating clouds (as in shallow convection or gravity waves).

In the same vein, Pinsky et al. (2014, 2015, 2018) presented a series of studies analysing phase transitions in an idealized rising parcel. These works derived closed-form expressions for key metrics like the glaciation time (the time until all liquid evaporates) and the critical vertical velocity needed to sustain liquid water. Pinsky et al. (2014) analytically investigated the overall glaciation timescale in a mixed-phase parcel, offering formulas for how quickly a cloud would glaciate under various conditions. Similarly, Pinsky et al. (2015) considered an adiabatic parcel ascending at constant speed and obtained an explicit formula for the minimum updraught (as a function of ice crystal concentration and other parameters) above which droplets will form and survive in an ice-seeded volume. That critical velocity criterion from Pinsky's analysis was consistent with the earlier numerical findings and even reinforced conclusions from field observations – namely, that both a sufficiently strong updraught and a limited ice population are required to maintain liquid water in cold clouds. Their 2018 follow-up expanded the theoretical framework, examining the interplay of microphysical rates and confirming the earlier threshold-based predictions in a more general context.

1.2.3 Stochastic Subgrid-Scale Modelling Approaches

Motivated by the idea from Korolev and Field (2008), that oscillatory vertical motion could explain mixed-phase persistence, Field et al. (2014) developed a stochastic description that served as basis for their subgrid parametrization used in a general circulation model (GCM) (Furtado et al., 2016).

Admittedly, taking into account the effect of high-frequency vertical velocity oscillations on the development of microphysical states is a step forward in comparison to relying solely on resolved velocity field provided by the GCM. However, accounting for *temporal* variability is not enough. The stochastic subgrid scheme by Field et al. (2014) and Furtado et al. (2016) has a common feature with the approaches described previously: the mean-field assumption for microphysics, where a fluctuating (stochastic) supersaturation is *uniformly* experienced by a large collection of cloud particles within a simulation grid box of several metres in extent.

All these approaches show that the ability of a cloud to maintain supercooled water under the mean-field assumption depends not just on temperature, but on *large scale dynamical forcing* and history of the air parcel. This strong dependence on vertical velocity is expected in mean-field models, but it underscores their deficiency: At length scales comparable to typical grid resolutions, turbulent motions can *locally* invigorate or suppress phase transitions beyond what a bulk value would imply, rendering the homogeneity assumption a gross approximation.

Modelling studies that go beyond the mean-field approximation and attempt to represent the intricate mixed-phase microphysics in a turbulent environment are still scarce (Korolev et al., 2017). A step towards more refined modelling has been done recently by Hoffmann (2020) by simulating the microphysics of a mixed-phase system using a Lagrangian (cloud-particle-based) version of the linear-eddy model (LEM) (Kerstein, 1988). In the LEM, turbulent advection and molecular diffusion of temperature and water vapour are treated simultaneously. Molecular diffusion of scalars is treated by solving the corresponding diffusion equation on a one-dimensional grid, which is periodically rearranged and compressed (using the so-called “triple map”) to simulate turbulent advection. Using the LEM to represent inhomogeneities in the thermodynamic fields, Hoffmann (2020) shows that the WBF process may be delayed in entraining mixed-phase cloud parcels with high concentration of ice particles (exceeding 100 to $1,000L^{-1}$).

1.3 Research objectives and approach

The focus in this work is to investigate the resilience of mixed-phase adiabatic cloud parcels by using a microphysical representation that is free from the mean-field assumption underlying numerous earlier studies of liquid-ice interaction [e.g., Korolev and Mazin (2003); Pinsky et al. (2014, 2015, 2018)]. Our representation accounts for variability of the temperature and vapour fields in the turbulent cloud environment. The *temporal and spacial* variability in the cloud particle growth conditions is represented by using a Lagrangian microphysical scheme, where temperature and vapour mixing ratio are Lagrangian stochastic variables attached to each cloud particle. These variables obey certain stochastic differential equations that we describe in detail later. The procedure used here borrows ideas from probability density function (PDF) methods (Pope, 1985) under the Lagrangian framework, commonly used in turbulent combustion flow research. Stochastic models have been used in the study of droplet spectrum broadening in warm (ice-free) cloud volumes [e.g., Sardina et al. (2015); Grabowski and Abade (2017); Abade et al. (2018); Sardina et al. (2018)]. These models directly resolve supersaturation fluctuations (owed to the stochasticity of vertical velocity) as the prognostic variable. In this work, the variability of ambient growth conditions is described in terms of stochastic temperature and vapour mixing ratio – supersaturation is *diagnosed*. This approach is more convenient to treat mixed-phase cloud systems. Earlier mean-field models [e.g., Korolev and Mazin (2003); Pinsky et al. (2014, 2015, 2018)] and ours consider idealised conditions and share a number of simplifying assumptions: we consider an adiabatic (non-entraining) cloud volume, where ice particles are spherical, and several microphysical processes such as sedimentation, aggregation of ice crystals, coalescence of liquid droplets, and riming are neglected. In contrast, our particle-based microphysics representation is significantly less idealised, and differs from the aforementioned models in many aspects. First, we directly resolve the growth of individual liquid droplets and ice particles by condensation/deposition, as we shall describe later. Therefore, we are free from the assumption that cloud particles are monodisperse, as in earlier studies. More specifically, our solution of the growth equations directly resolves the activation and deactivation of liquid droplets (as solvent and curvature effects are taken into account). Also, we explicitly resolve the heterogeneous and homogeneous freezing of liquid droplets and possible melting of ice particles. These processes are not represented in the earlier studies mentioned herein.

It must be emphasized that some large eddy simulations (LES) of mixed-phase clouds – for example, see Kaul et al. (2015) – are free from the drawbacks of the mean-field approximation because they do not resolve the growth of cloud particles explicitly, but use a bulk parametrisation of the microphysics that artificially maintains supercooled water in the grid box by imposing a temperature-dependent liquid water fraction $\mu = r_\ell/(r_\ell + r_i)$, where r_ℓ and r_i are the mixing ratios of liquid and ice respectively. In general, the parametrisations of the liquid fraction used in bulk schemes encapsulate a variety of unrepresented microphysical processes (such as ice nucleation, freezing of supercooled droplets, melting of ice particles, local variability of the condensation environment), and contain parameters that are tuned to make the overall scheme consistent with observations. We use the scheme by Kaul et al. (2015) as a reference for comparison against other microphysical models, including our Lagrangian stochastic model. This parametrisation assumes that the thermodynamic phase partitioning between condensed water phases (i.e., liquid and ice) is uniquely determined by the mean temperature in each grid box. The partitioning between water vapour and condensate phases in the work of Kaul et al. (2015) is done via a mixed-phase saturation adjustment procedure based on the aforementioned temperature-dependent parametrisation of the liquid fraction μ. The computation of μ implies the specification of a sampling volume, i.e., the grid box volume, and with it, an associated spatial averaging length scale. When representing subgrid processes, the inclusion of such characteristic length scale as a model parameter is of utmost importance for determining the characteristic time scales and statistical properties of the unresolved variables.

In earlier studies based on a non-turbulent adiabatic parcel model with mean-field microphysics [e.g., Korolev and Mazin (2003); Pinsky et al. (2014, 2015, 2018)], no length scale associated with the cloud parcel is specified. However, the omission of this parameter does not allow it to be unrestricted. Indeed, it is *implicitly bounded*, by both the spatial homogeneity assumption and the droplet number concentration per unit volume, as we shall later discuss.

In contrast, our turbulent adiabatic parcel has a characteristic linear size Δ, the length scale at which our cloud volume is assumed to acquire its mean turbulent kinetic energy (TKE) at a given rate ε per unit mass. This length is a crucial parameter to assess the validity of the mean-field assumption, i.e, to assess whether it is reasonable to assume a well mixed, spatially homogenous environment in terms of temperature, humidity, and consequently supersaturation. Furthermore, the length scale Δ specifies the linear extent of the sampling volume over which relevant microphysical information is determined. Since the aim our cloud parcel experiments is to provide insights into subgrid modelling of the microphysics in large-eddy simulations (LES) of clouds, it is reasonable to assume that Δ is within the range of typical LES grid spacing. Thus, Δ lies in the inertial range of cloud turbulence and usually varies from several metres to several tens of metres. Such a large volume in a turbulent cloud will *inevitably* contain cloud particles experiencing different adiabatic cooling rates, arising from turbulent fluctuations in the vertical velocities. This is the main source of variability in the particle growth conditions in our adiabatic (non-entraining) parcel model.

The results of the theoretical study presented in this thesis, also published in Abade and Albuquerque (2024), demonstrate the significant role of unresolved turbulence in explaining the persistence os mixed-phase clouds, and, conversely, how neglecting it by assuming spatial homogeneity at subgrid scales leads to a strong bias in the WBF effect. By introduction of a characteristic turbulent mixing time scale, paired with stochastic velocity fluctuations, we demonstrate that a weaker coupling between local scalar fields (i.e., experienced by each individual particle), and their respective parcel-wide averages facilitates liquid activation despite the presence of growing ice crystals. Stochastic fluctuations enable spatially and temporally sparser activations, softening the requirement of minimum average supersaturation for droplet activation. Additionally, deviations from the mean allow for sustained liquid growth in the presence of ice, while also enabling increased activation of ice nucleating particles (INP).

Our model was able to sustain a mixed-phase state for several hours, revealing that the dynamical criteria for mixed-phase persistence developed in earlier studies [e.g. Korolev and Mazin (2003); Korolev and Field (2008); Pinsky et al. (2014, 2015, 2018)] are not applicable to large-scale averaged volumes. Rather, our results suggest the unresolved, subgrid-scale turbulent composition of updraughts and downdraughts play an important role in maintaining long-lived mixed-phase systems, as opposed to the LES-resolved mean updraughts. The stochastic microphysical approach developed herein lays the foundation for the development of subgrid parametrisation schemes that address the shortcomings of current models, leading to potential advancements in cloud modelling and our understanding of climate.

1.4 Thesis outline

The remainder of this thesis is structured as follows. Chapter 2 introduces the adiabatic parcel model, an idealised framework that isolates cloud microphysical processes by prescribing parcel motion and eliminating external heat or mass exchange. Chapter 3 develops a bulk microphysics scheme for warm and mixed-phase clouds based on the mean-field assumption and a temperature-dependent phase partitioning parametrization, providing baseline results for the subsequent approaches. Chapter 4 then presents a mean-field Lagrangian microphysics approach, explicitly resolving the microphysical growth equations for individual cloud droplets and ice crystals in a homogeneous parcel. These results highlight the strong glaciation bias under the mean-field assumption and motivates the stochastic approach. Building on this foundation, chapter 5 introduces a stochastic Lagrangian microphysics model that incorporates turbulent fluctuations, capturing subgrid-scale variability and demonstrating its impact on condensational growth and mixed-phase cloud evolution. Finally, chapter 6 synthesises the key findings, situates them in the broader context of cloud microphysics and turbulence, and concludes the thesis with implications and prospects for future research.

2

The Adiabatic Parcel Model

In this chapter we present an idealised framework: *the adiabatic cloud parcel.* Put simply, it constitutes a container for the microphysical models of increasing complexity described in chapters 3, 4, and 5, where they can be put on a spotlight and compared, isolated from the overwhelming complexity of more comprehensive cloud models.

Atmospheric clouds are complex, multi-scale systems in which several interdependent physical and chemical processes occur simultaneously. These processes directly influence the micro and macro-scale properties of clouds. In this study, we focus primarily on the microphysical description of clouds, more specifically on condensational growth of cloud particles. In order to objectively assess the influence of a variety of microphysical models on cloud properties, it is wise to simplify our cloud model as much as possible. In doing so, one gains control over the external parameters that drive microphysical processes. By making use of an adiabatic cloud parcel model with prescribed motion, we are able to ensure that all microphysical models are subject to the same external forcing. In such scenario, differences in the cloud microphysical structure are more easily identified and attributed to differences in the microphysics modeling, rather than to secondary processes, such as large scale convection, entrainment of dry air, radiative interaction and so forth. We do, however, acknowledge the limitations of such approach, as well as the need for validation of a microphysical description in a fully coupled and dynamic cloud simulation.

An adiabatic cloud parcel, as the name suggests, is an idealized model conceived to explain the basics of cloud physics, and also a very convenient framework to evaluate cloud micro-physical models. In essence, it is a closed system comprised of moist air, kept in mechanical equilibrium with the environment at all times. The parcel move around in a stratified atmosphere, but without ever exchanging mass or heat with its surroundings. Due to vertical pressure gradients, the parcel experiences cooling and heating along its trajectory as a result of adiabatic expansion and compression, respectively, thus creating the necessary conditions for droplet activation/deactivation and condensational growth/evaporation to take place. The parcel's bulk (or average) state can be defined as

$$\mathbf{S} = \{p(z), \;\; T, \;\; q_v, \;\; r_\ell, \;\; r_i\}, \tag{2.1}$$

where z is the height relative to the ground level, p is the atmospheric pressure, T is the thermodynamic temperature, and q_v, r_ℓ and r_i are respectively the mixing ratios of vapour, liquid and ice, defined in terms of the mass ratios

$$r_\alpha = \frac{m_\alpha}{m_d}, \quad \alpha = v, \; l, \; i, \tag{2.2}$$

where m_d stands for the mass of dry air in the mixture.

Because of the assumption of mechanical equilibrium, the pressure of the parcel is equal to the environmental one, which is assumed to be a function of height only. Additionally, because of the assumption of no mass exchange, the total amount of water and air inside the parcel is constant, which results in

$$r_t = q_v + r_\ell + r_i = constant. \tag{2.3}$$

The change in temperature inside the parcel will be influenced by a few different mechanisms. The first one is adiabatic cooling or heating, which is related to pressure changes along the parcel's trajectory as a direct consequence of environmental stratification. In fact, adiabatic cooling is the main mechanism responsible for increasing local saturation during updraughts, which eventually leads to the onset of droplet condensation. Once condensation starts, however, another source of temperature change comes into play: the release of latent heat, which counteracts the adiabatic cooling effect.

The first law of thermodynamics in terms of enthalpy for a dry adiabatic air parcel reads

$$dh = \frac{dp}{\rho}. \tag{2.4}$$

By means of the ideal gas equation of state, one can easily derive Poisson's relation

$$Tp^{-\kappa} = constant, \tag{2.5}$$

with $\kappa = \mathcal{R}_d/c_p$ where $\mathcal{R}_d$ is the individual dry air constant and c_p is its specific heat at constant pressure. In other words, this means that temperature is fully determined by the pressure profile and consequently is also a function of height only. For this reason, it is common practice in atmospheric sciences to define a temperature that is conserved in adiabatic processes, known as potential temperature. From equation 2.5 one can define a reference state, where the pressure is p_0, usually taken as approximately the standard atmospheric pressure at sea level, and the temperature is denoted by θ. On the other side of the equality, we represent an arbitrary state (T, p), so that

$$\theta p_0^{-\kappa} = T p^{-\kappa}, \tag{2.6}$$

and thus

$$\theta = \frac{T}{\Pi}, \quad \text{where} \quad \Pi = \left(\frac{p_0}{p}\right)^{-\kappa} \tag{2.7}$$

is called the potential temperature, that is, the temperature the air would attain if it were adiabatically brought to the reference pressure. The Π factor is called the Exner function. From equation 2.4, one can derive that, for an ideal gas,

$$\frac{dT}{T} - \frac{\mathfrak{R}_d}{c_p}\frac{dp}{p} = \frac{\delta q}{c_p T}, \tag{2.8}$$

which after some rearrangement, yields

$$d \ln\left(T P^{-\mathfrak{R}_d/c_p}\right) = d\ln\theta = \frac{\delta q}{c_p T}. \tag{2.9}$$

Equation 2.9 affirms that, in the absence of heat exchange, θ is conserved. In the scope of the adiabatic parcel model, the only contribution to δq on the right-hand side of equation 2.9 would come from the release of latent heat, which is fully determined once a microphysical model is chosen. Unlike pressure, which is externally imposed, the mixing ratios q_v, r_ℓ, and r_i, as well as θ, are coupled to the microphysical processes and change dynamically as these processes evolve in time.

One might be tempted to determine the time progression of the parcel's height, $z(t)$, as the result of net buoyancy forces. However, this approach would defeat the purpose of our framework, which is to ensure that all microphysical models are subject to the same external forcing. For this reason, we prescribe the vertical velocity $w(t)$, and consequently $z(t)$ is obtained by simple integration with the appropriate initial condition.

The micro-physical processes will dictate the rates of change of r_ℓ, r_i, q_v and θ due to phase change processes, such as condensation, evaporation, vapour deposition, sublimation, freezing and melting. The way these processes evolve in time and how they affect the mixing ratios, and particle size distributions (if applicable) depends on the assumptions made in the microphysical model. Specific models will be described and discussed in chapters Other known micro-physical processes such as aggregation, rhyming and splintering are not considered in this study, as we focus on the impact of turbulent mixing on condensation dynamics.

2.1 Environmental Profiles

As previously mentioned, our air parcel interacts with its environment solely via pressure, since heat and mass exchanges are not present. An environmental pressure profile can be determined by means of the hydrostatic balance hypothesis, which can be mathematically expressed as

$$\nabla p = -\rho g \hat{\mathbf{e}}_{\mathbf{z}}, \tag{2.10}$$

where ρ is the air density, which varies with height, g is the modulus of the gravitational acceleration and $\hat{\mathbf{e}}_{\mathbf{z}}$ is the vertical unit vector pointing upwards. Additionally, we make use of the ideal gas law in the following form

$$p = \rho \mathcal{R}_d T_v, \tag{2.11}$$

where $\mathcal{R}_d = R/M_d$ is the specific gas constant for dry air, that is, the universal gas constant divided by the average molar mass of dry air, and T_v is the virtual temperature, given by

$$T_v = T\left(\frac{1 + r/\varepsilon}{1 + r}\right) \approx T(1 + 0,61q_v), \tag{2.12}$$

where $\varepsilon = \mathcal{R}_d/\mathcal{R}_v$ is the ratio between the specific gas constants for dry air and water vapour respectively(Rogers and Yau, 1989).

By using the definition of the potential temperature (eq. 2.7) together with equation 2.11, one can derive the following relation:

$$p^{\kappa-1}dp = -\frac{gp_0^{\kappa}}{\mathcal{R}_d}\frac{dz}{\theta_v(z)}, \tag{2.13}$$

where θ_v is the virtual potential temperature, defined analogously to T_v. The left-hand side of equation 2.13 above can be integrated analytically, yielding

$$p(z) = \left(p_0^{\kappa} \quad - \quad \frac{gp_0^{\kappa}}{c_p}\int_0^z \frac{dz'}{\theta_v(z')}\right)^{1/\kappa}, \tag{2.14}$$

where p_0 is the atmospheric pressure at $z = 0$, which does not necessarily coincide with p_0. Since $\theta_v(z) = \theta(z)[1 + 0.61q_v(z)]$, equation 2.14 provides the pressure profile, given the environmental profiles of potential temperature and vapour mixing ratio are available.

2.2 Microphysical Closure

The adiabatic parcel model presented so far still requires a closure, as we haven't provided equations to describe the phase change processes that take place as the parcel travels across different altitudes. As mentioned earlier, predicting the time evolution of the microphysical state of the cloud parcel, as well as its bulk properties, requires the adoption of a microphysical model. In a simplified approach, one could assume phase equilibrium, i.e., that phase changes occur much faster than any other process in the system and thus can be considered to instantly reach equilibrium. As we will soon discuss, this assumption is rather strong, as droplet growth time scale is not negligible. This can be accounted for in particle-based models, as the one developed in this thesis. The equations below, however, result from simple balances of mass and energy, and thus do not depend on the choice of a microphysical model. Starting from the mass conservation law, we may take the time derivative of equation 2.3, which yields

$$\frac{dq_v}{dt} + \frac{dr_\ell}{dt} + \frac{dr_i}{dt} = 0, \tag{2.15}$$

where each term on the left-hand side can be broken down as follows:

$$\begin{aligned} \frac{dq_v}{dt} &= -\langle\dot{C}\rangle - \langle\dot{D}\rangle, \\ \frac{dr_\ell}{dt} &= \quad \langle\dot{C}\rangle - \langle\dot{F}\rangle, \\ \frac{dr_i}{dt} &= \quad \langle\dot{D}\rangle + \langle\dot{F}\rangle. \end{aligned} \tag{2.16}$$

Here, $\langle\dot{C}\rangle$, $\langle\dot{D}\rangle$ and $\langle\dot{F}\rangle$ are the average rates of condensation, deposition and freezing, respectively. These quantities are determined by the microphysical model, which should contain equations to describe those processes. Note that $\langle\dot{C}\rangle$, $\langle\dot{D}\rangle$ and $\langle\dot{F}\rangle$ are dependent on the parcel's environmental variables T, p, and q_v, making the equations fully coupled.

The second point of closure is in the energy equation, where changes in the potential temperature are caused by the release and absorption of latent heat by the condensate phases. This coupling occurs via the RHS of equation 2.8, but before we expand dq in terms of the phase changes, let us do some rearrangement. If we divide equation 2.8 by the corresponding infinitesimal time difference in which the state changes occur, we obtain

$$\frac{1}{T}\frac{dT}{dt} = \frac{R}{c_p}\frac{1}{p}\frac{dp}{dz}\frac{dz}{dt} + \frac{1}{c_pT}\frac{dq}{dt}, \tag{2.17}$$

where we have used the chain rule to force the appearance of two important terms: the vertical pressure gradient and the vertical velocity. Assuming hydrostatic balance and making use of the ideal gas law, one obtains

$$\frac{dT}{dt} = -\frac{g}{c_p}w + \frac{1}{c_p}\frac{dq}{dt}, \tag{2.18}$$

where w is the parcel's vertical velocity. The ratio $-g/c_p$ is typically called the adiabatic lapse rate. Equation 2.18 already clearly illustrates what has been previously mentioned, that the rate of change of the parcel's mean temperature will deviate from the adiabatic lapse rate due to the influence of latent heat.

Finally, by writing the rate of heat exchange between the parcel's air and the condensate phases in terms of the phase change rates, the equation for temperature reads

$$\frac{dT}{dt} = -\frac{g}{c_p}w + \frac{L_v}{c_p}\langle\dot{C}\rangle + \frac{L_s}{c_p}\langle\dot{D}\rangle + \frac{L_f}{c_p}\langle\dot{F}\rangle, \tag{2.19}$$

where L_v, L_s and L_f are the latent heats of vaporization, sublimation and fusion, respectively, which by convention are all positive values as these processes result from an increase in the energy of the system.

Given that a microphysical model provides us with precise information on how $\langle\dot{C}\rangle$, $\langle\dot{D}\rangle$ and $\langle\dot{F}\rangle$ depend on the environmental parameters, equations 2.16 and 2.19 determine the time evolution of the parcel's state, since w is prescribed and consequently so is the pressure p. Details on different approaches to microphysical modelling are given in the following chapters.

3

Bulk Microphysics

Having established the adiabatic parcel model as a controlled framework to isolate and examine cloud microphysical processes, we now turn to the choice of closure formulations that govern phase changes within the parcel – the microphysical models. The most widely used approach in large-scale simulations is bulk microphysics, which provides computationally efficient closures under simplified assumptions. In this chapter we introduce a bulk parameterization scheme, first in the context of warm clouds and subsequently extended to mixed-phase conditions, thereby offering a natural baseline against which more detailed microphysical schemes can later be compared.

Bulk methods typically yield values of r_ℓ and r_i based on a couple of simplifying assumptions, namely mechanical and phase equilibrium (Lozar and Mellado, 2014). The mechanical equilibrium assumption greatly simplifies the transport equations by neglecting the drift between phases, while phase equilibrium means that phase changes occur infinitely fast, eliminating the need to describe the dynamics of particle nucleation and growth altogether, while providing a closure to microphysics equations. The main advantage of such methods is the fact that they are computationally very inexpensive in comparison to Lagrangian particle-based or Eulerian bin microphysics models, which explains their vast use in large scale simulations. Particle-based methods, on the other hand, are computationally more intensive, but yield a more precise and detailed description of the microphysics, allowing for the representation of many complex physical and chemical processes.

As a frame of reference for our future simulations, we consider a one-moment bulk microphysics model based on a *saturation adjustment* scheme from Grabowski and Smolarkiewicz (1990). In essence, this model neglects the time scale of condensation, so that any amount of water vapour above the saturation limit is instantly converted into condensate. Moreover, the only calculated microphysical properties are the liquid water mixing ratio r_ℓ, and the ice mixing ratio r_i. Additional characteristics of the cloud particle population, such as number concentration, average size, and other higher-order statistics are unavailable except through ad hoc parametrizations. These mixing ratios measure the liquid water or ice mass per unit mass of dry air, thus being proportional to the average particle volume, linked to the third moment of the particle size distribution – hence the term: one-moment bulk model (More on that in chapter 4).

3.1 Warm Cloud

As an introduction to the main reasoning of this scheme, let us consider the warm case, i.e., when the condensate phase contains only liquid water. In the following section we expand the model to include the ice phase.

Initially, our parcel starts at ground level, unsaturated. This initial state may be expressed by

$$z = z_0, \quad T = T_0, \quad q_v = q_{v,0}, \quad r_\ell = 0, \tag{3.1}$$

with $q_{v,0} < q_{s,\ell}(T_0,\ p(z_0))$. As we prescribe a vertical motion to the parcel, bringing it up across the stratified environment, q_v remains constant while $q_{s,\ell}$ decreases with the decrease of both pressure and temperature. Eventually, the parcel reaches a point where

$$q_v = q_{s,\ell}(T,\ p(z)). \tag{3.2}$$

The height at which this happens for the first time is the so called lifting condensation level (LCL). If we proceed with the vertical ascent above the LCL, saturation adjustment should ensure that equation 3.2 holds true, i.e. that the parcel remains at saturation conditions while building up on liquid condensate. Because of the release of latent heat, which affects the rate of change of the parcel's temperature, analytical calculation of r_ℓ is not feasible. However, one can obtain it through iterative calculations. To do so, we discretize our time domain:

$$t^{(n)} = t^{(0)} + n\Delta t, \quad n \in \mathbb{N}. \tag{3.3}$$

Eventually, during the parcel's ascent there will be an instant $t^{(n+1)}$ where for the first time $q_v^{(n+1)} > q_{s,\ell}(T^{(n+1)},\ p(z^{(n+1)}))$. In order to impose the saturation condition, we must find the amount of water that condensed during the interval $(t^{(n)},\ t^{(n+1)})$. In other words, we must find $\Delta_\ell = r_\ell^{(n+1)} - r_\ell^{(n)}$ such that

$$q_v^{(n+1)} \equiv q_v^{(n)} - \Delta_\ell = q_{s,\ell}\Big(T(\Delta_\ell),\ p\Big(z^{(n+1)}\Big)\Big), \tag{3.4}$$

where $T(\Delta_\ell)$ is the temperature attained by the parcel after the condensation process, given by

$$T(\Delta_\ell) = \Pi^{(n+1)}\theta^{(n)} + \frac{L_v \Delta_\ell}{c_p}. \tag{3.5}$$

The two terms on the RHS of 3.5 can be interpreted respectively as the temperature of the parcel at height $z^{(n+1)}$ before condensation takes place plus the increase in temperature caused by the release of latent heat. Additionally, by combining the ideal gas law and Dalton's law of partial pressures, one can show that

$$q_{s,\ell}(T,p) = \frac{\varepsilon e_{s,\ell}(T)}{p - e_{s,\ell}(T)}, \tag{3.6}$$

where $e_{s,\ell}(T)$ is the saturation vapour pressure, obtained as the analytical solution to Clausius-Clapeyron equation:

$$\frac{de_{s,\ell}}{dT} = \frac{L_v}{\mathcal{R}_v}\frac{e_{s,\ell}}{T^2}, \tag{3.7}$$

which yields

$$e_{s,\ell}(T) = e_{s,0} \exp\left\{ -\frac{L_v}{\mathcal{R}_v}\left(\frac{1}{T} - \frac{1}{T_0}\right)\right\}, \tag{3.8}$$

where $e_{s,0} \equiv e_{s,\ell}(T_0)$ and T_0 is the temperature of the triple point of water.

One can now solve equation 3.4 by defining a function $F(\Delta_\ell)$ as

$$F(\Delta_\ell) = q_{s,\ell}(T(\Delta_\ell), p(z^{(n+1)})) - q_v^{(n)} + \Delta_\ell. \tag{3.9}$$

The problem now consists in finding the root of F. This can be done, for example, with the Newton-Raphson method, where we start with an initial guess Δ_0 and iterate according to

$$\Delta_\ell^{(i+1)} = \Delta_\ell^{(i)} - \frac{F(\Delta_\ell^{(i)})}{F'(\Delta_\ell^{(i)})} \tag{3.10}$$

until convergence is reached. Here $F'(\Delta_\ell)$ denotes the first derivative of $F(\Delta_\ell)$.

Whenever evaporation occurs ($\Delta_\ell < 0$), we must ensure that all mixing ratios remain greater than or equal to zero by imposing

$$\Delta_\ell = \min\{-\Delta_\ell^*,\ \ r_\ell^{(n)}\}, \tag{3.11}$$

where Δ_ℓ^* is obtained as a solution to equation 3.4. In doing so, we ensure that the amount of evaporated water during one time step never exceeds the total amount of liquid water in the parcel.

Once Δ_ℓ is determined, the parcel's properties can be updated accordingly:

$$\begin{aligned} r_\ell^{(n+1)} &= r_\ell^{(n)} + \Delta_\ell, \\ q_v^{(n+1)} &= q_v^{(n)} - \Delta_\ell, \\ \theta^{(n+1)} &= \theta^{(n)} + \frac{L_v}{c_p \Pi^{(n+1)}} \Delta_\ell. \end{aligned} \tag{3.12}$$

Note that the quantity Δ_ℓ can be expressed in terms of the condensation rate as $\langle \dot{C} \rangle \Delta t$. The choice of the potential temperature as a state variable here is convenient due to its conservation in the absence of condensation. In our Lagrangian stochastic model, as we will discuss in chapter 5, tracking the conventional temperature is more sensible, as makes explicit the source of temperature stochasticity that comes from the adiabatic cooling term.

The results shown in figure 3.1 were generated using the above described scheme and constant vertical profiles of $\theta = 269$ K, and $q_v = 1.5$ g kg^{-1}. In this simulation, the parcel starts at ground level with an initial state equivalent to the external environmental state. Vertical velocity is set to 1 m/s. It should be noted, however, that vertical velocity has no influence on the parcel state in this model. Imposing a saturation state above the condensation level essentially means that condensation is regarded as an instant process. In other words, the system is considered to be in phase equilibrium. As a consequence, the parcel state depends on z only, making all the processes fully reversible.

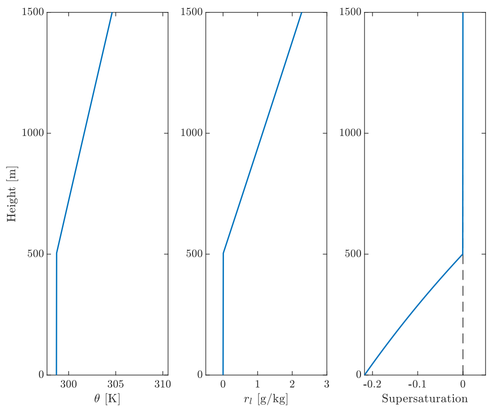

Figure 3.1: Vertical profiles of potential temperature, liquid water mixing ratio and saturation for a rising adiabatic parcel with saturation adjustment scheme.

3.2 Mixed-phase Cloud

As mixed-phase clouds are the main object of study of this thesis, we have now present a mixed-phase saturation adjustment scheme developed by Kaul et al. (2015). It can be regarded as mixed-phase version of the scheme presented in section 3.1. For this formulation, it is convenient to have a definition of potential temperature that is conserved not only under adiabatic processes, but also under processes involving phase changes. By combining equations 2.16 and 2.19 and using the relationship $L_s = L_v + L_f$, we may obtain

$$\frac{d\ln\theta}{dt} = \frac{L_v}{c_pT}\frac{dr_\ell}{dt} + \frac{L_s}{c_pT}\frac{dr_i}{dt}. \tag{3.13}$$

Thus the condensed water potential temperature defined as

$$\theta_c = \theta\exp\left(-\frac{L_v}{c_pT}r_\ell - \frac{L_s}{c_pT}r_i\right) \tag{3.14}$$

is a conserved quantity for temperature independent latent heats (Tripoli and Cotton, 1981).

At any given moment, the amount of condensate in the parcel may be given by

$$r_c = r_i + r_\ell = \max\left\{r - \bar{q}_s(T,p),\ \ 0\right\}, \tag{3.15}$$

where r is the total water mixing ratio, and $\bar{q}_s$ is the vapour saturation mixing ratio for the mixed-phase parcel, given by

$$\bar{q}_s(T,p) = \mu\, q_{s,\ell}(T,p) + (1-\mu)q_{s,i}(T,p). \tag{3.16}$$

Here, $q_{s,\ell}$ and $q_{s,i}$ are the vapour saturation mixing ratios relative to the liquid and ice phases respectively, and μ is the liquid water fraction in relation to the total condensate mass. This quantity may be parametrized in terms of other state variables. Here, we follow Kaul et al. (2015) and use

$$\mu(T) = \left(\frac{T-T_c}{T_w-T_c}\right)^n, \quad T_c \le T \le T_w, \tag{3.17}$$

with threshold temperatures $T_w = 235$ K, $T_c = 273$ K and $n = 0.1$. For temperatures outside the transition interval, we define $\mu(T \le T_c) = 0$ and $\mu(T \ge T_w) = 1$. The threshold temperatures are known physical constants, namely the heterogeneous and homogeneous freezing temperatures at standard atmospheric pressure. The only adjustable parameter in equation 3.17 is the exponent n, which is adjusted to provide a good agreement with mixed-phase cloud observations.

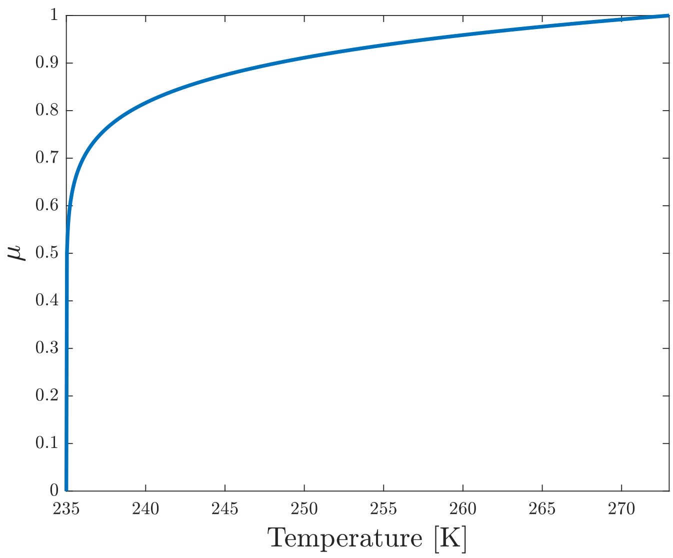

Figure 3.2: Temperature parametrization of liquid water fraction. The n exponent is adjusted to provide good agreement with mixed-phase cloud observations (Kaul et al., 2015).

The mixing ratios for each condensate phase are obtained in terms of the total condensate r_c and the liquid water fraction μ as follows:

$$\begin{aligned} r_\ell(T,p) &= \mu(T)\; r_c(T,p), \\ r_i(T,p) &= [1-\mu(T)]\; r_c(T,p). \end{aligned} \tag{3.18}$$

The formulation above guarantees that, for every (T, p), we obtain $S \leq 0$. Analogously to what was done for the warm case, we may now make use of equation 3.14 to determine the temperature T_s that satisfies the energy balance by preserving the original value of θ_c. In other words, we are now looking for the root of

$$\mathcal{F}(T) = \theta_c - \frac{T}{\Pi(p)} \exp\left[-\frac{L_v}{c_p T} r_\ell(T,\; p) - \frac{L_s}{c_p T} r_i(T,\; p) \right]. \tag{3.19}$$

Similarly to the warm case, the parcel's temperature T_s such that $\mathcal{F}(T_s) = 0$ can be obtained numerically. Note that the root of $\mathcal{F}(T)$ depends solely on the initial conditions θ_c and r, and the hydrostatic pressure $p(z)$. This results, once more, in the state of the parcel being ultimately a function of height only. The formulation above is general and covers also warm clouds ($\mu(T) = 1$), and ice clouds, i.e. $\mu(T) = 0$.

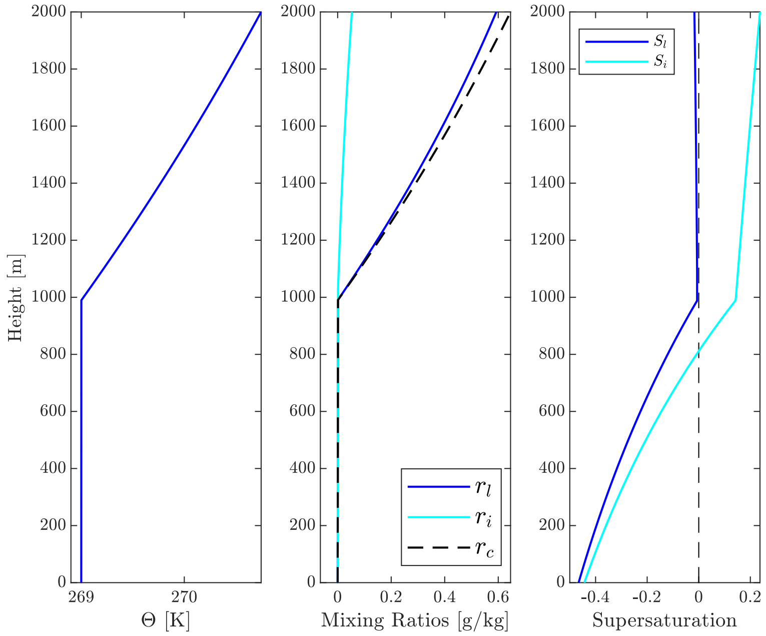

Figure 3.3: Vertical profiles of potential temperature, liquid and ice mixing ratios, and supersaturation for the mixed-phase bulk model. The parcel predominantly consists of liquid water, as a consequence of the empirically adjusted phase partitioning function. As a consequence, the system remains close to liquid water saturation, while supersaturation with respect to the ice phase grows up to 20%.

The profiles of θ, r_ℓ, r_i, S_ℓ and S_i can be observed in figure 3.3. As a consequence of the temperature parametrization of μ, liquid water makes up most of the condensate phase for a wide range of temperatures. Accordingly, the parcel's mean saturation $\bar{q}_s$ is very close to S_ℓ, while the ice phase experiences significant supersaturation. This might seem paradoxical at first, given that such conditions would lead to strong condensational growth of the ice phase, with simultaneous evaporation of the liquid phase. However, it is important to note that the parametrization of μ as a simple function of temperature is an attempt to reproduce observed mixed-phase states while circumventing the description of a multitude of underlying microphysical processes that lead to those states. In the next chapter, we introduce a a particle-based approach, in which we describe the dynamics of droplet growth in detail.

4

Mean-field Lagrangian Microphysics

While bulk microphysics offer a computationally efficient means of representing cloud processes, their reliance on strong equilibrium assumptions and limited prognostic variables highlights important shortcomings. In particular, they cannot provide explicit information about droplet size distributions, which is essential for connecting microphysics to observable cloud properties, and predicting other phenomena such as precipitation. To overcome these limitations, the current chapter introduces a Lagrangian particle-based formulation under the mean-field assumption. This approach allows for a more detailed representation of droplet growth, including solute and surface tension effects, and provides the framework for examining activation processes and liquid-ice phase partitioning under the mean-field assumption.

The fundamental assumption of saturation adjustment schemes is that the time scale of condensation is negligibly short. In other words, saturation is attained instantly, regardless the vertical velocity, particle concentration or droplet sizes. Although an attractive option for large-scale models due to their computational tractability, bulk microphysics tend to be oversimplified and often rely on ad hoc parametrizations calibrated against observational data. This makes it challenging to estimate several quantities of interest that depend on higher order momenta of the cloud's particle size distribution (PSD). For instance, several integral warm cloud properties can be expressed as moments of the droplet size distribution (DSD). Let $n(R)\,\mathrm{d}R$ denote the number concentration of droplets with radii between R and $R + \mathrm{d}R$. The k-th moment of the DSD is then defined as

$$M_k \;=\; \int_0^\infty R^k\, n(R)\,\mathrm{d}R. \tag{4.1}$$

Different physical quantities of interest are directly related to specific moments. For example, the *liquid water content (LWC)* is proportional to the third moment,

$$\mathrm{LWC} \;=\; \frac{4\pi\rho_\ell}{3}\,M_3, \tag{4.2}$$

where ρ_ℓ is the density of liquid water. The *extinction coefficient* relevant for radiative transfer depends on the second moment, while the *radar reflectivity factor* is proportional to the sixth moment,

$$Z \;\propto\; M_6 \;=\; \int_0^\infty R^6\, n(R)\,\mathrm{d}R. \tag{4.3}$$

Because higher-order moments give increasingly large weight to the largest droplets, measurements such as radar reflectivity are dominated by the presence of relatively few but large particles, whereas lower-order moments (e.g. M_0, M_1) describe number concentration and mean size. This hierarchy of moments provides a compact framework linking microphysical processes to remote-sensing observables and bulk cloud properties.

For this reason, a cloud model that resolves particle growth and explicitly provides a distribution of sizes for droplets and ice particles is of great interest. With detailed PSD information, one can more accurately predict the radiative properties that determine how clouds influence Earth's energy budget. Furthermore, the evolution rates of microphysical processes such as precipitation, collision coalescence, riming, and condensational growth itself are strongly affected by particle size.

In the present chapter, we describe a Lagrangian micro-physical scheme (Shima et al., 2009) based on the dynamics of droplet growth by condensation. Other microphysical processes, such as collision-coalescence, droplet breakup, riming, and precipitation are out of the scope of this thesis. Here, we focus on describing the droplet and ice diffusional growth dynamics under the mean-field approximation, a hypothesis that will be confronted with our stochastic approach in chapter 5. Particle freezing and melting mechanisms are also implemented and described later in the current chapter. These mechanisms allow our system to naturally transition between a warm, mixed-phase, or an ice cloud volume as temperature and humidity dynamically evolve.

4.1 Growth equation of liquid droplets

Here we introduce the condensational growth equation for liquid droplet, obtained by solving the coupled heat and mass diffusion problem for a spherical droplet immersed in quiescent moist air. The result is a differential equation for the droplet radius R, whose change rate is driven by supersaturation:

$$\frac{dR}{dt} = \frac{1}{R}\mathcal{D}_\ell\left[\langle S_\ell\rangle - \frac{A}{R} + \frac{B}{R^3}\right]. \tag{4.4}$$

Here, $\mathcal{D}_\ell$ a diffusion coefficient corrected to account for the effect of latent heat release on the temperature of the surrounding air (Rogers and Yau, 1989). The full expression for $\mathcal{D}_\ell$ reads:

$$\mathcal{D}_\ell = \left[\frac{\mathcal{R}_v T_\infty \rho_\ell}{\mathcal{D}_0 e_{s,\ell}(T_\infty)} + \frac{L_v \rho_\ell}{K_0 T_\infty}\left(\frac{L_v}{\mathcal{R}_v T_\infty} - 1\right)\right]^{-1}, \tag{4.5}$$

where T_∞ is the undisturbed far-field temperature and $\mathcal{D}_0$ is the water vapour diffusion coefficient, assumed constant for the temperature range considered in our application. The $\langle S_\ell\rangle$ term in equation 4.4 is the parcel's average supersaturation with respect to pure water over a flat surface, given by

$$\langle S_\ell\rangle = \frac{e}{e_{s,\ell}(\langle T\rangle)} - 1. \tag{4.6}$$

Two important physical phenomena are considered in the derivation of equation 4.4: The *solute effect* and the *surface tension effect*. Droplet condensation typically initiates on the surface of microscopic aerosol particles – called cloud condensation nuclei (CCN) – often constituted of water soluble minerals. As a result, each droplet is in fact a weak mineral solution, whose equilibrium vapour pressure is influenced by the solute's concentration. The term proportional to B in equation 4.4 accounts for the so-called solute effect, also known as Raoult's Law (Raoult, 1882). Dissolved mineral particles compete with water molecules for space on the droplet's free surface, reducing water activity, and lowering the equilibrium vapour pressure.

The surface tension effect, known as the Kelvin effect [see Thomson (1871)], accounts for the effect of surface tension on the equilibrium vapour pressure due to the droplet's surface curvature. This effect is stronger in smaller droplets, where the surface curvature is more pronounced. Surface tension acts by increasing the droplets' internal pressure, resulting in an abrupt pressure change across the surface – represented mathematically as a discontinuity – that facilitates evaporation. In equation 4.4, this is accounted for by the term multiplied by coefficient A. Together, these two terms compose the equilibrium supersaturation for a spherical droplet formed around a soluble aerosol particle, given by

$$S_{\ell,eq}(R) = \frac{A}{R} - \frac{B}{R^3}, \tag{4.7}$$

with

$$A = \frac{2\sigma}{\rho_\ell \mathcal{R}_v \langle T \rangle} \approx 10^{-3} \mu m, \tag{4.8}$$

where σ is the water surface tension coefficient, and

$$B = \kappa R_d^3, \tag{4.9}$$

where κ is the hygroscopicity factor of the solute and R_d is the dry radius, i.e, the radius the soluble substance would attain if shaped as a compact sphere (Petters and Kreidenweis, 2007). Together, the Kelvin effect and Raoult's Law are the two main drivers of a mechanism called droplet activation (Köhler, 1936). While the solute effect lowers the required supersaturation, facilitating condensational growth, the surface tension effect poses an obstacle by increasing the required supersaturation.

Because the coefficients A and B are always positive, $S_{\ell,eq}(R)$ exhibits a positive maximum value for $r > 0$. The radius at which this maximum occurs is called the droplet's critical (or activation) radius, given by

$$R_c = \sqrt{\frac{3B}{A}}. \tag{4.10}$$

The maximum value for $S_{\ell,eq}(R)$ is called the critical (or activation) saturation, given by

$$S_c = S_{\ell,eq}(R_c) = \sqrt{\frac{4A^3}{27B}}. \tag{4.11}$$

Figure 4.1a displays the shape of $S_{\ell,eq}(R)$, known as the Köhler curve (Köhler, 1936), and illustrates the activation mechanism. For values of environmental saturation $\langle S_\ell \rangle < S_c$ (green dashed line), the branch of the curve to the left of R_c is stable, meaning that droplet sizes will stabilize at R_{eq} such that $S_{\ell,eq}(R_{eq}) = \langle S_\ell \rangle$. This equilibrium point corresponds to the left green intersection point on the upper plot. Droplets with $R > R_{eq}$ will imply $S_{\ell,eq} > \langle S \rangle$, which according to equation 4.4 results in the reduction of the radius (i.e. evaporation) over time. Likewise, a droplet with $R < R_{eq}$ will experience a small condensational growth until equilibrium is restored. Particles in those conditions, known as haze particles, are typically smaller than 1 µm and contain a very small but stable amount of water.

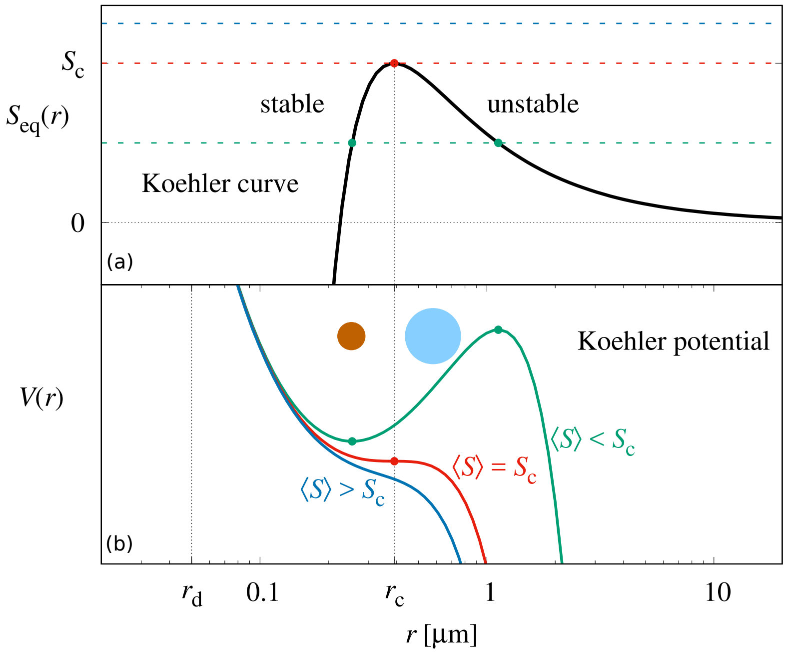

Figure 4.1: Droplet activation: The Köhler curve and Köhler potential [Source: Abade et al. (2018)]. Figure shows the equilibrium supersaturation $S_{\ell,eq}(R)$, and the Köhler potential, $V(R)$, as functions of the droplet radius, R. In the upper panel, droplet size is stable on the left branch of the curve, corresponding to haze particles, i.e., aerosol particles with a stable an relatively small amount of liquid water condensed around it. On the right branch, droplet size is unstable, with perturbations towards the right leading to continuous growth, while perturbations towards the left tend to lead the droplet back to its haze particle state. On the panel below, the Köhler potential curves illustrate size stability for different scenarios, as the droplet radius changes in the direction that locally minimizes the potential.

Upon eventual exposure to a supercritical environmental saturation ($\langle S \rangle > S_c$), a haze particle will grow beyond its activation (critical) radius and become activated. These are referred to as cloud particles or cloud droplets. On the right branch, because of the negative slope of $S_{\ell,eq}(R)$, the droplet radius is unstable. Droplets with $R < R_{eq}$ will shrink down and stabilize at the left (stable) branch, while cloud droplets with $R > R_{eq}$ will grow indefinitely for a constant $\langle S \rangle$. That condition, however, implies a replenishment of water vapour at the same rate it is being consumed by the growing droplet (everything else kept constant). In a more realistic scenario, the surrounding air saturation is affected by condensation, providing a negative feedback loop. Droplets will then tend to stabilize their activated size once $\langle S_\ell \rangle = S_{\ell,eq}(R)$ is observed.

This mechanism may also be described in terms of a Köhler potential V (Abade et al., 2018), defined by

$$-\frac{\partial V}{\partial X} \equiv 2\mathfrak{D}_\ell \left[\langle S_\ell \rangle - \frac{A}{X^{1/2}} + \frac{B}{X^{3/2}} \right], \tag{4.12}$$

where the right-hand side is equivalent to the RHS of equation 4.4, written in terms of $X \equiv R^2$. Solving for V and switching back to variable R one gets

$$V(R) = 4\mathfrak{D}_\ell \left[-\frac{1}{2}\langle S_\ell \rangle R^2 + AR + \frac{B}{R} \right]. \tag{4.13}$$

The shape of $V(R)$ is shown on the lower panel of figure 4.1. Now it becomes clear that when the environmental saturation is lower than the critical one (green curve), the droplet is trapped in a potential well and cannot grow beyond the size of a haze particle. Once the critical saturation is reached (red curve), the potential barrier becomes flat, allowing the droplet to activate.

Equations 4.9 and 4.11 show an inverse relation between R_d and S_c. Köhler observed this and postulated that, due to their lower value of S_c, larger aerosol particles would activate first and prevent the smaller ones from activating by reducing the amount of available water vapour. Thus there would be a "selection of nuclei". This phenomenon, often referred to as the *lucky droplet effect*, is indeed observed in simulations when droplets with different R_d grow under the same environmental conditions, however it is significantly overrepresented in the mean-field approach, as we shall later discuss.

A typical distribution of dry radii encountered in a cloud takes the shape of a log-normal curve. In our study, the variability of aerosol sizes is obtained by sampling R_d from a log-normal distribution

$$f(R_d) = \frac{1}{R_d \sigma \sqrt{2\pi}} \exp\left\{ -\frac{[\ln(R_d/\tilde{R}_d)]^2}{2\sigma^2} \right\}, \tag{4.14}$$

with median $\tilde{R}_d = 7.5 \times 10^{-2}$ µm, and logarithmic standard deviation $\sigma = 0.47$, which are within the typical range for aerosol size distributions in marine clouds (Ueda et al., 2016). To obtain the values of R_d for each particle, we use the inverse sampling technique, which consists of drawing a random number ξ from a uniform distribution and finding R_d such that $F(R_d) = \xi$, where $F(R_d)$ is the cumulative distribution function obtained by integration of 4.14,

$$F(R_d) = \frac{1}{2} + \frac{1}{2}\,\mathrm{erf}\left[\frac{\ln(R_d/\tilde{R}_d)}{\sqrt{2}\sigma} \right]. \tag{4.15}$$

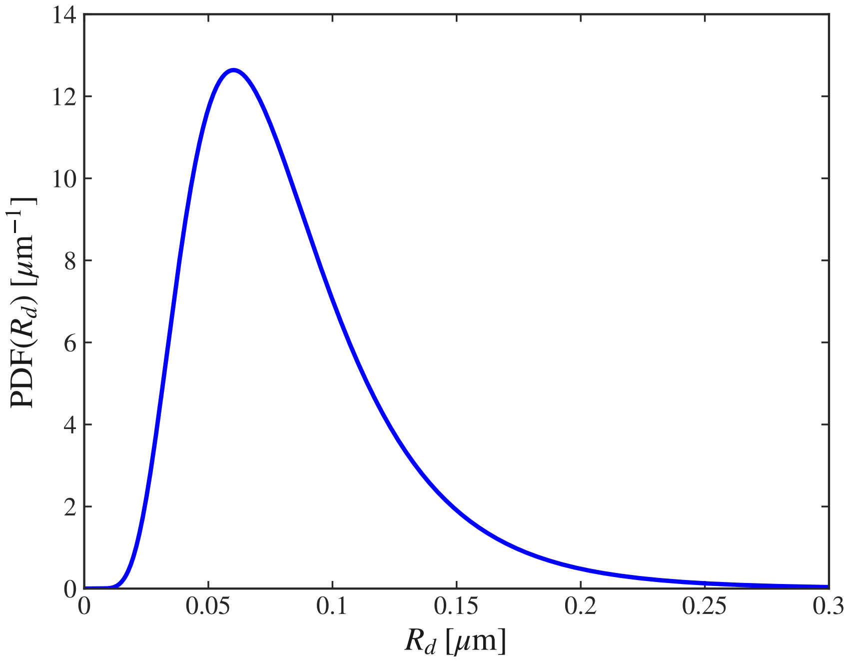

Figure 4.2: A typical dry radius distribution. $\tilde{R}_d = 7.5 \times 10^{-2}$ µm and $\sigma = 0.47$ (Ueda et al., 2016)

4.2 The Super-droplet Method

Typical droplet number concentration in clouds ranges from about 10^7 to 10^9 m^{-3} (i.e. 10^1–10^3 cm^{-3}) in clean to moderately polluted environments (Rogers and Yau, 1989). Representing every single one of them in a computer model is incredibly expensive, and will most likely continue to be so for decades to come. For instance, a domain with a grid box size of 100m x 100m x 10m would contain anywhere from 10^{13} to 10^{14} particles per box. Not only would this be impractical, but having information about each individual cloud particle would be superfluous. Ultimately, one only needs a number of particles that is large enough to be representative of the real population.

Current synoptic-scale simulations still have spatial resolutions limited to approximately 1 km at best. Populating such coarse grids with particles, even if feasible, would still fail to capture the small-scale (sub-grid) variability in temperature and humidity fields, which causes these particles to have diverse growth histories. For those reasons, planetary weather simulations heavily rely on parametrization of cloud microphysics. A Lagrangian approach, despite its technologically constrained scope of application, has unique advantages. It allows for more natural, intuitive, and accurate descriptions of several microphysical phenomena such as droplet coalescence and breakup, rhyming, and immersion freezing. This is because a particle-based approach allows the model to keep track of a complex set of particle state variables, such as position, velocity, aerosol mass, composition and chemical properties, and the amount of liquid water or ice.

Aiming to seize the benefits of Lagrangian models while keeping computational costs tractable, Shima et al. (2009) introduced the super-droplet method (SDM), which consists of representing large groups of droplets as one single computational object, the so called super-droplet. The number of real droplets represented by each super-droplet is called the multiplicity factor (ξ), which can be different for each super-droplet and may change over time as a result of physical processes such as coalescence and breakup. This method was initially designed to deal with the description of collision/coalescence processes in particle-based models. At the same time, it enables a detailed description of the micro-physics in terms of aerosol physical and chemical properties, and is also very convenient in our description of a stochastic micro-physical scheme, to be detailed in the next chapter.

Unlike in the collision-coalescence problem, our model results are insensitive to ξ, and the microphysical processes treated here do not modify ξ over time. Thus, for simplicity we adopt the same multiplicity for every particle. The value set for every super-droplet upon simulation initialization is

$$\xi = \frac{N}{N_{sd}}, \tag{4.16}$$

where N is the total number of real droplets and N_{sd} is the number of computational super-droplets, both applicable to each grid box.

The mass of condensate contained in one super-droplet is given by

$$m_k = \xi \rho_\ell \frac{4}{3}\pi (R_k^3 - R_{d,k}^3), \tag{4.17}$$

where ρ_ℓ is the density of liquid water and $R_{d,k}$ is the dry radius of the k-th super-droplet. Consequently, the liquid water mixing ratio can be expressed as

$$r_\ell = \frac{1}{m_d} \sum_{k=1}^{N_{sd}} m_k = \frac{4\pi \rho_\ell \xi}{3 m_d} \sum_{k=1}^{N_{sd}} \left(R_k^3 - R_{d,k}^3 \right). \tag{4.18}$$

As the growth rate is used to update the values of R_k, the conservation of mass and energy laws demand that we update the other parcel properties accordingly. The conservation of mass imposes

$$\frac{dq_v}{dt} + \frac{dr_\ell}{dt} = 0, \tag{4.19}$$

and thus

$$\frac{dq_v}{dt} = -\frac{d}{dt}\left[\frac{4\pi\rho_\ell\xi}{3m_d}\sum_{k=1}^{N_{sd}}\left(R_k^3 - R_{d,k}^3\right)\right], \tag{4.20}$$

which can be integrated through one time step to obtain

$$q_v(t+\Delta t) = q_v(t) - \frac{4\pi\rho_\ell\xi}{3m_d}\sum_{k=1}^{N_{sd}}\left(R_k^3(t+\Delta t) - R_k^3(t)\right). \tag{4.21}$$

The last term on the right side of equation 4.21 is net change in the vapour mixing ratio due to condensation and evaporation processes happening on the surface of each droplet. It is essentially the same as the $\Delta_\ell = \langle\dot{C}\rangle\Delta t$ term in equations 3.12 and these can be used to update r_ℓ and θ as well, although a direct calculation of r_ℓ by means of equation 4.18 would be advised to avoid the accumulation of numerical errors.

4.3 Warm Parcel

So far we have covered all the equations necessary to simulate a warm cloud parcel. One of the key differences between simulating droplet growth via equation 4.4 and the saturation adjustment described previously, is that we now have a time scale associated with condensational growth and evaporation processes. Instead of instantly attaining equilibrium, the parcel now dynamically reacts to supersaturation as a driving force of condensational growth.

As a result, the particle-base model will always display a smaller amount of liquid water in the constant ascent simulation. As the droplet activation takes some time to initiate, supersaturation builds up. This can be observed in figure 4.3, where for any given height above the condensation level, the super-droplet model always has less liquid water than the bulk model.

One might be tempted to conclude that the saturation adjustment provides a theoretical upper limit to the amount of liquid water that the parcel should hold. However, note that if we were to reverse the vertical velocity, the super-droplet model would once again lag behind, retaining liquid water for longer and thus having more water than the bulk model for a given height. For the Lagrangian model, one can derive a time evolution equation for S_ℓ under the assumption of constant vertical velocity, which has the following form (Squires, 1952):

$$\frac{dS_\ell}{dt} = aW - \frac{S_\ell}{\tau}, \tag{4.22}$$

where W is the vertical velocity, and τ is the so-called phase relaxation time, given by

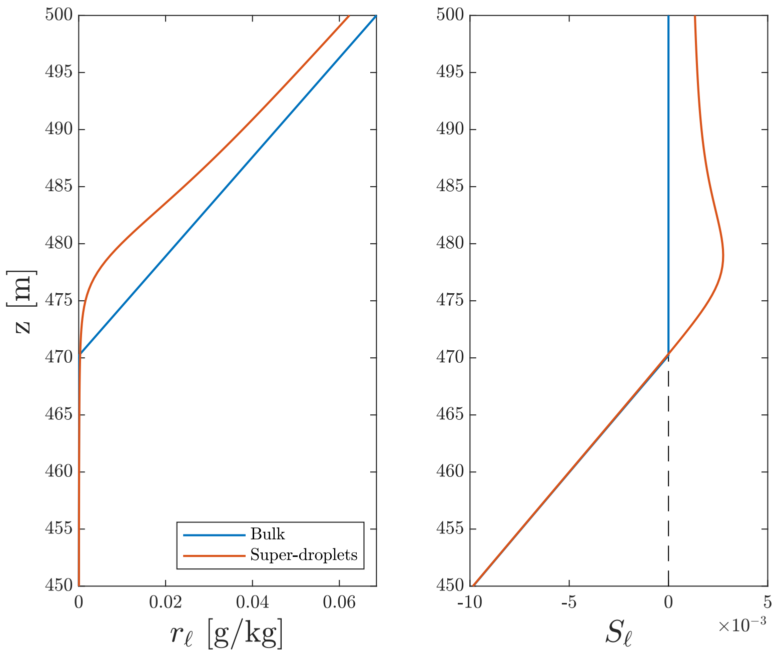

Figure 4.3: Liquid water mixing ratio and supersaturation profiles for an adiabatic parcel rising at a constant speed of 0.5m/s. Super-droplet results were obtained with an aerosol concentration of 2×10^8 particles per kilogram of dry air. The bulk model attains saturation instantly and thus is the theoretical upper bound for r_ℓ. The super-droplet model lags behind due to the response time of condensational growth to changes in saturation.

$$\tau = \frac{1}{b4\pi\rho_\ell Dn\langle R\rangle}. \tag{4.23}$$

The derivations for equations 4.22 and 4.23 as well as the coefficients a and b can be found in the book *A Short Course in Cloud Physics*, by Rogers and Yau (1989). The phase relaxation time is a measure of how fast the droplets are able to react to changes in saturation. Droplet concentration n and mean radius $\langle R\rangle$ are the two main variables that may significantly change τ, and the explanation is quite intuitive. In terms of the parcel's bulk behaviour, the assumption of saturation adjustment is equivalent to taking the limit of equation 4.22 with $\tau \to 0$, when vertical velocity becomes irrelevant and saturation instantly relaxes to zero.

4.4 Mixed-phase parcel

Solving the growth equation 4.4 for every super-droplet in our parcel enables us to compute the average condensation rate $\langle \dot{C} \rangle$, necessary for the parcel's mass and energy balances. When dealing with mixed-phase clouds, however, two other phase change processes come into play: deposition and freezing. As mentioned in chapter 2, these processes are represented in the balance equations by their mean rates $\langle \dot{D} \rangle$ and $\langle \dot{F} \rangle$ respectively.

Analogously to the warm case, computing $\langle \dot{D} \rangle$ requires solving the growth equation for the ice particles. For that purpose, we need to modify equation 4.4 accordingly: The diffusion coefficient D must be calculated using L_s instead of L_v, the surface tension effect removed, since it is no longer present in solid phase, and Raoult's effect may also be neglected, since the solute particles are trapped inside the ice lattice and water activity is quickly restored to unity as new layers of ice are formed around the crystal. Thus, we set $A = 0$ and $B = 0$ for the ice particles, i.e., there is no activation mechanism. Ice nucleation is not discussed in this study, as ice particles are assumed to be frozen cloud droplets or haze particles. Lastly, the effect of non-sphericity of the ice crystals may be taken into account by introducing a capacitance factor (Pruppacher and Klett, 1997), however, predicting the accurate shape of the ice particles as they grow and shrink inside a turbulent cloud is a formidable challenge certainly beyond the scope of this thesis. Hence, we assume spherical particles and a capacitance factor equal to unity. From equation 4.4, the general growth equation for mixed-phase clouds may be written as

$$R_k \frac{dR_k}{dt} = (1 - \varphi_k)\mathcal{D}_i \langle S_i \rangle + \varphi_k \mathcal{D}_\ell \Big[\langle S_\ell \rangle - S_{\ell,eq}(R) \Big], \tag{4.24}$$

where φ_k is the phase indicator attribute. If the k^{th} particle is a liquid droplet or a deliquesced aerosol, $\varphi_k = 1$, otherwise $\varphi_k = 0$. Once the radii are updated, one can calculate the liquid water and ice mixing ratios with the aid of the phase indicator attribute as follows:

$$r_\ell(t) = \frac{4\pi}{3} \frac{\rho_\ell \xi}{m_d} \sum_{k=1}^{N_{sd}} \varphi_k \Big[R_k^3(t) - R_{d,k}^3 \Big], \tag{4.25}$$

$$r_i(t) = \frac{4\pi}{3} \frac{\rho_\ell \xi}{m_d} \sum_{k=1}^{N_{sd}} (1 - \varphi_k) \Big[R_k^3(t) - R_{d,k}^3 \Big]. \tag{4.26}$$

The vapour mixing ratio can be obtained by simple conservation of mass. The condensation and deposition rates can be expressed in terms of the radial increments as

$$\langle \dot{C} \rangle(t) = \frac{4\pi}{3} \frac{\rho_\ell \xi}{m_d \Delta t} \sum_{k=1}^{N_{sd}} \varphi_k \Big[R_k^3(t) - R_k^3(t - \Delta t) \Big], \tag{4.27}$$

$$\langle \dot{D} \rangle(t) = \frac{4\pi}{3} \frac{\rho_\ell \xi}{m_d \Delta t} \sum_{k=1}^{N_{sd}} (1 - \varphi_k) \Big[R_k^3(t) - R_k^3(t - \Delta t) \Big]. \tag{4.28}$$

For the average freezing rate can be computed from the changes in the phase indicator attribute as

$$\langle \dot{F} \rangle(t) = -\frac{4\pi}{3} \frac{\rho_\ell \xi}{m_d \Delta t} \sum_{k=1}^{N_{sd}} R_k^3(t) \Big[\varphi_k(t) - \varphi_k(t - \Delta t) \Big]. \tag{4.29}$$

4.4.1 Freezing and Melting

The attentive reader might have noticed that we have been using the phase indicator attribute to compute several bulk quantities as well as to define a new generic version of the growth equation that applies for both ice and water particles. However, we have not defined how φ_k changes as a function of the environment in which the droplet is immersed. The simplest way to define φ_k would be to just verify whether the parcel's temperature is below or above that of water freezing for the current value of pressure $p(z)$. This approach, however, would fail to represent a particularity of cloud droplets, i.e. the fact that they are often significantly super-cooled. This happens because the aerosol particles, around which liquid water accumulates, are generally made of soluble substances. As a result, many of these droplets consist of a weak mineral solution, without any contact with solid surfaces that could eventually facilitate the nucleation of ice crystals.

There are a handful of mechanisms responsible for ice production, such as heterogeneous and homogeneous immersion freezing, riming, i.e., ice formation upon droplet-ice collision, and rime-splintering, which is a mechanism of secondary ice production (SIP) via small fragments (splinters) of ice formed during the riming process. The latter still lacks empirical evidence and a recent experimental study by Seidel et al. (2024) concludes it is not an efficient SIP mechanism. Heterogeneous and homogeneous freezing are considered to be the dominant modes in most mixed-phase clouds (Cui et al. (2006), de Boer et al. (2011)) and for that reason shall be the only ones implemented in our model.

In heterogeneous immersion freezing, ice nucleates on the surface of an ice nucleating particle (INP), which will be immersed into the water droplet. This will typically be a small amount of an insoluble substance, coated by the soluble mineral upon which the droplet was formed. The quantity of insoluble material in the aerosol particle can be parametrized by the insoluble dry radius $\hat{R}_d$. Thus, each aerosol particle is now characterized by a set of three parameters $(R_d,\ \hat{R}_d,\ \kappa)$.

The temperature at which heterogeneous freezing occurs is a random variable whose probability distribution depends on the amount of insoluble material present inside each droplet. In our study, we assume that 10% of aerosol particles contain a small amount of insoluble mineral, represented by $\hat{R}_d$. To determine the freezing temperature distribution, we follow Niemand et al. (2012) and use

$$F(T_f) = \exp\Big[- A\, n_s(T_f) \Big], \tag{4.30}$$

where A is the surface area of the insoluble material and n_s is the number of active nucleation sites per unit area. The function $n_s(T)$ is of the form

$$n_s(T) = \exp(aT + b), \tag{4.31}$$

where a and b are empirically determined coefficients. Figure 4.4 shows the freezing temperature probability distributions for different values of $\hat{R}_d$. The equations for these curves are obtained by simply differentiating equation 4.30 with respect to T_f. Larger values of $\hat{R}_d$ shift the distribution towards higher temperatures, as a result of the increased number of active ice nucleation sites present on the surface of the insoluble material. For simplicity, we use a constant value of $\hat{R}_d = 0.5$ µm for every particle, thus sampling all freezing temperatures from the same distribution.

The freezing temperature for each particle is a constant attribute, sampled from equation 4.30 similarly to the procedure done for R_d sampling. Both R_d and T_f are attributed to each super-droplet at the initialization stage of the simulation. Experimental studies have also shown that supersaturation S_ℓ also has an impact on the probability of freezing. Here, we follow Shima et al. (2020) and use a simplified model that defines three necessary conditions for droplet freezing:

$$\begin{aligned} i)&\ \ \langle T \rangle < T_f, \\ ii)&\ \ \langle S \rangle > 0, \\ iii)&\ \ \varphi_k = 1, \end{aligned} \tag{4.32}$$

where the third condition is simply a requirement that the particle is in liquid state.

Conversely, the conditions for melting to occur are

$$\begin{aligned} i)&\ \ \langle T \rangle > 0\,^\circ\mathrm{C}, \\ ii)&\ \ \varphi_k = 0. \end{aligned} \tag{4.33}$$

With the set of equations described in this section, we are now able to simulate a mixed-phase parcel model with a Lagrangian (particle-based) microphysical scheme. In figure 4.5, we can see the mixing ratio profiles for both bulk and super-droplet schemes for an adiabatic parcel rising at constant speed. The models start by exhibiting similar behaviour until ice starts forming at approximately

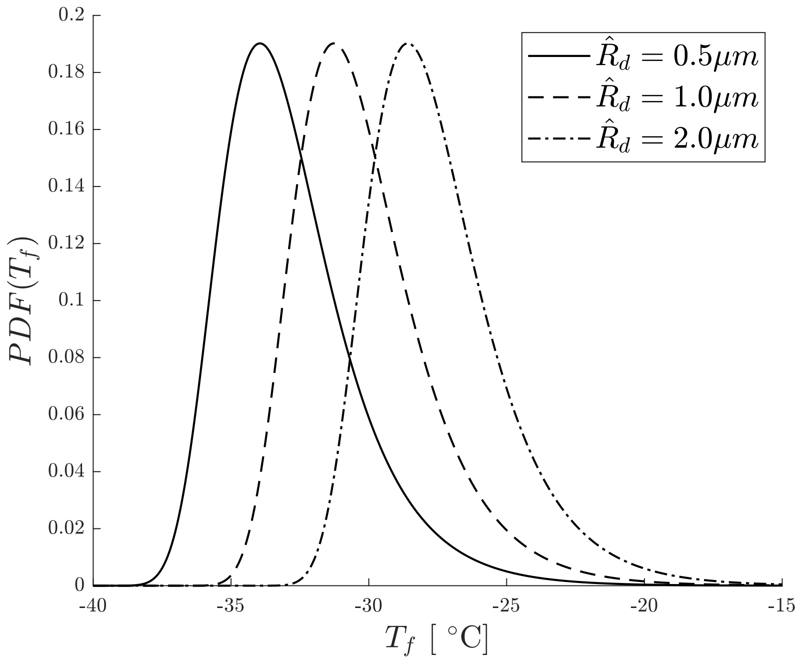

Figure 4.4: Freezing temperature probability distributions for different values of $\hat{R}_d$. Larger portions of insoluble material lead to higher freezing temperatures due to increased number of active nucleation sites, causing the distribution to shift right.

1500m. From this moment forward, ice particles grow very rapidly in the Lagrangian model, causing the remaining liquid droplets to evaporate. This is a well documented phenomenon, known as the Wegener-Bergeron-Findeisen (WBF) process [Wegener (1911); Bergeron (1935); Findeisen (1938)]. It occurs when ice particles and water droplets compete for the same ambient water vapour. Since ice is thermodynamically more stable at sub-zero temperatures, it grows quicker, causing the surrounding air to become sub-saturated with respect to liquid water. In contrast, the bulk model maintains a phase partitioning comprised mostly of liquid water, due to its temperature parametrization of $\mu(T) := r_\ell/r_c$, designed to keep the water-to-ice ratio compatible with mixed-phase cloud measurements.

The profiles of S_ℓ and S_i for both models is shown in figure 4.6, and they provide valuable insight about the fundamental differences between them. In bulk scheme, it is clear that the water phase experiences even more sub-saturation when compared to the super-droplet results, while maintaining a predominant water phase as a consequence of the parametrization of μ. For the same reason, the ice phase does not grow, even though it is subject to very high levels of supersaturation. This may sound counter-intuitive or even paradoxical (and it is), but the reader

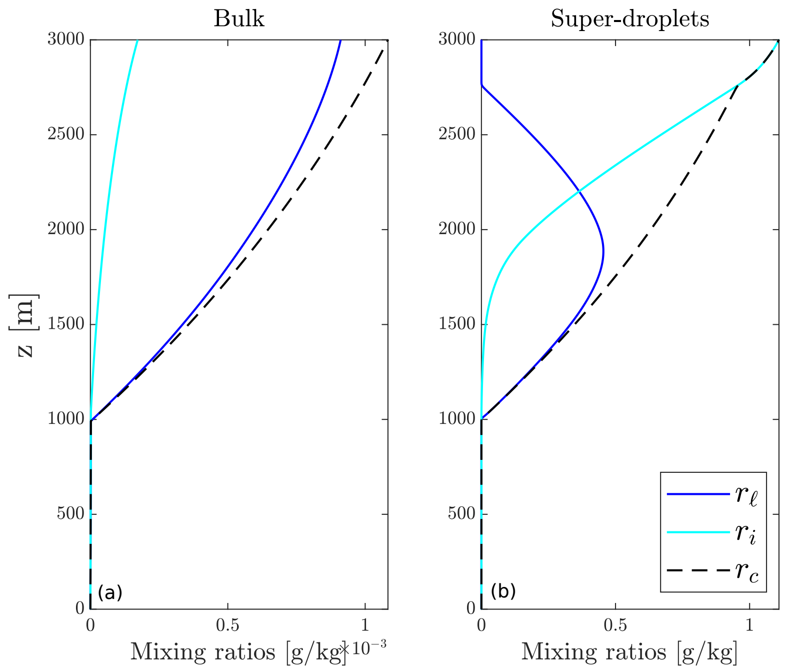

Figure 4.5: Condensate mixing ratio profiles comparison between bulk and mean-field super-droplet methods. With parametrized phase partition function, the bulk model exhibits a proportion between ice and liquid water that is dictated by temperature only. On the other hand, the super-droplets display an unstable behaviour that eventually leads to glaciation due to the WBF mechanism.

should bear in mind that the parametrization of μ is an attempt to circumvent the description of other physical processes that could explain the dominance of liquid water, thus leading to unphysical outcomes.

In the super-droplet model, the stark difference in saturation observed between ice and liquid water is directly reflected in the rate of growth of these two phases. This is expected, of course, as we are now simulating particle condensational growth as a function of environmental parameters. Note how $\langle S_\ell \rangle$ deviates very little from zero when the parcel height is between 1000m and 2750m approximately. The liquid water saturation profile is shown in greater detail on the left side of the Super-droplets panel. Up to 2000 m height, water droplets are preventing the increase of $\langle S_\ell \rangle$ by consuming vapour and consequently growing. Above that height, the droplets are evaporating and thus preventing $\langle S_\ell \rangle$ from deviating from zero as well. Only when water is depleted at approximately 2750m (see figure 4.6), do we observe the system shifting towards $\langle S_i \rangle \approx 0$.

The explanation for why we observe $\langle S_\ell \rangle \approx 0$ for the greater part of this

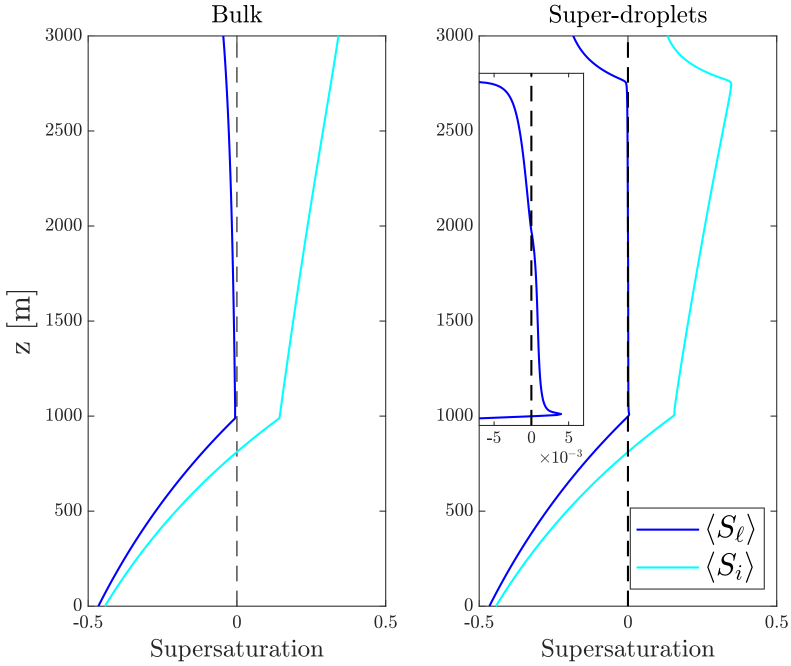

Figure 4.6: Supersaturation for liquid water and ice in both bulk and mean-field super-droplet approaches. In the particle-based model, the parcel is kept at $\langle S_\ell \rangle \approx 0$ until complete water evaporation, after which the system transitions towards ice saturation.

simulation lies on the difference in phase relaxation times between liquid water and ice phases. From its definition in equation 4.23, $\tau \propto (Dn\langle R \rangle)^{-1}$. The differences in coefficient of diffusion (D) are on the order of 10% and slightly favour the water phase. The particle number concentration of water droplets is much larger, i.e. $n_\ell \gg n_i$. This is largely due to the fact that Ice Nucleating Particles (INP) are only present in a small fraction of the aerosol. Therefore, initially we have $\tau_\ell \ll \tau_i$, so the water phase is able to react much faster, thus maintaining $\langle S_\ell \rangle \approx 0$. After a significant amount of water evaporates, with simultaneous growth of ice crystals, we reach a point where $\langle R \rangle_i \gg \langle R \rangle_\ell$. In other words, the much greater size of ice particles compensate for their reduced number, so that $\tau_\ell \approx \tau_i$. This allows the ice phase to significantly influence the bulk saturation of the parcel. The behaviour of $\langle S_\ell \rangle$ as a function of the ratio τ_ℓ/τ_i can be observed in figure 4.7.

The phase inversion observed in figure 4.5b is expected from the thermodynamic point of view, however it is in contradiction with the observational data, which motivated the phase partitioning parametrization used in the bulk model. We claim that the main cause of this contradiction is the assumption of complete homogeneity of the parcel scalar fields. In our particle-based model, we have assumed a homogeneous temperature and vapour mixing ratio throughout the entire parcel. This assumption is only reasonable for very small volumes of air. For large parcels, i.e. when the linear size Δ is much greater than the Kolmogorov length, the inhomogeneities of those fields cannot be neglected. The assumption of homogeneity artificially magnifies the WBF effect, creating an extremely fast, and large-scale glaciation. This same artefact is present in three-dimensional weather simulations (Furtado, 2018), where coarse grid resolutions and microphysics parametrizations are used to compensate for domain size. In the next chapter we will introduce a stochastic approach to representing scalar fields variability without the need to fully resolve turbulence.

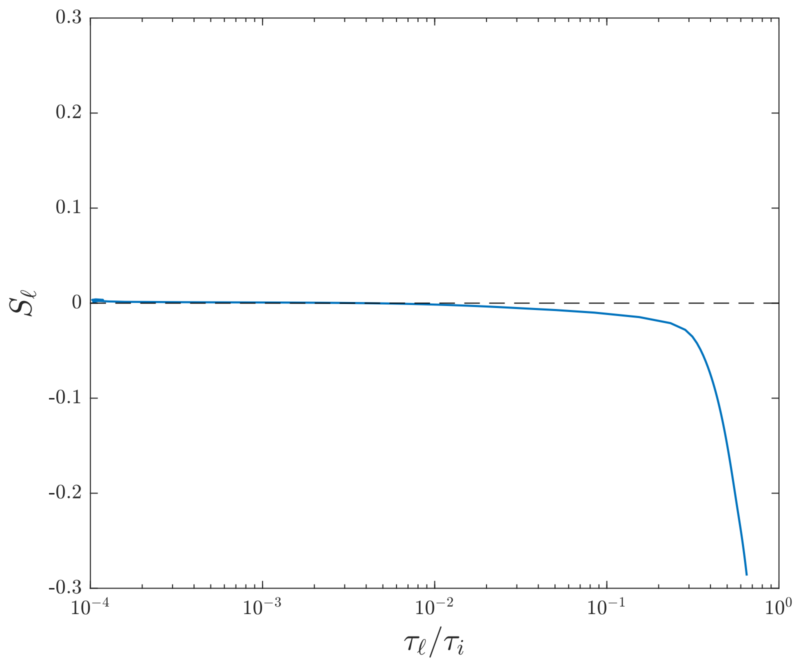

Figure 4.7: Liquid water supersaturation as a function of the ratio between phase relaxation times. The rising parcel remains close to liquid water saturation ($\langle S_\ell \rangle \approx 0$) as long as $\tau_\ell \ll \tau_i$. As we approach $\tau_\ell/\tau_i \approx 1$, the parcel deviates from $S_\ell = 0$ towards ice saturation.

5

Stochastic Lagrangian Microphysics

In chapter 4 we observed the stark contrast in phase partitioning behaviour when comparing the saturation adjustment scheme with parametrized liquid fraction μ against the explicitly resolved condensational growth in a homogeneous parcel. In this chapter, we discuss the importance of parcel's characteristic length scale for defining model assumptions and characterizing the microphysics environment. We then introduce our stochastic Lagrangian microphysical model, which we regard as an advance in representing the coupling between cloud microphysics and inertial-range turbulence, scales that are generally unresolved in large-eddy cloud simulations.

The microphysical model and the results described in this chapter constitute the core of this thesis. The result of this work has been peer reviewed and published in the *Quarterly Journal of the Royal Meteorological Society* [see Abade and Albuquerque (2024)]. Here, we present it in greater detail, with extended discussions on the motivation and interpretation of results.

5.1 Microphysical domain size: A crucial model parameter

The previous chapter showed that the homogeneity assumption leads to an artificial amplification of the WBF mechanism. This manifests as rapid cloud glaciation driven by intensified ice deposition growth, accompanied by droplet evaporation. The persistent bias towards glaciation is an inherent feature of many larger scale models [Furtado (2018), Cesana et al. (2012)] for the same reason – it is a direct consequence of the mean-field assumption, i.e., the assumption that a great collection of particles – water droplets and ice crystals alike – are subject to the same environmental conditions in a domain with an extent of several hundreds of meters in all three dimensions. Evidently, this assumption is adopted in numerical weather simulations for the lack of a better, technically feasible alternative. The consequence is a classical deficiency of the mean-field approach – its inability to explain the existence of long-lived mixed-phase clouds without other mechanisms such as precipitation, or the income of external liquid water.

Homogeneous parcel studies such as Korolev and Mazin (2003), Korolev and Field (2008), and Pinsky et al. 2014, 2015, 2018 suggest dynamical forcing as a necessary condition for obtaining a persistent mixed-phase state. In these studies, however, the parcel size is not a modelling parameter, as every quantity is computed on a per-unit-mass basis. Although not specified, nor acknowledged as a limitation, the parcel size in the aforementioned studies is bounded by model assumptions and physical constraints. For a detailed discussion, see Abade (2025).

On the lower bound, parcel size is limited by typically observed cloud droplet concentrations. Ideally, a cloud parcel should contain enough cloud particles for the relevant statistical moments of the particle size distributions to be well defined. As mentioned in chapter 4, moments of the particle size distribution are used to calculate several integral cloud properties of climatic interest, such as the extinction coefficient, relevant for estimating the rates of radiative transfer.

On the upper bound – and that's the central point of the discussion – homogeneous parcels are constrained by the Batchelor scale (Batchelor, 1959), which is essentially Kolmogorov's length scale, slightly modified to account for molecular diffusion:

$$\eta_B = \eta S_c^{-1/2}, \tag{5.1}$$

where $\eta = (\nu^3/\varepsilon)^{1/4}$ is the Kolmogorov length scale, where turbulent kinetic energy is dissipated into heat, and $S_c = \nu/\mathcal{D}$ is the Schmidt number, a measure of momentum diffusivity by viscosity versus molecular diffusivity of scalar fields. Here, ν is the kinematic viscosity, ε if the TKE dissipation rate, and $\mathcal{D}$ is the molecular diffusivity of the corresponding scalar field. For water vapour, $\mathcal{D}_v \approx 2.5 \times 10^{-5}$ $\mathrm{m^2\,s^{-1}}$ at 0 °C, while for heat diffusion in air, $\mathcal{D}_T \approx 2.0 \times 10^{-5}$ $\mathrm{m^2\,s^{-1}}$. The kinematic viscosity of air also at 0 °C is $\nu = 1.33 \times 10^{-5}$ $\mathrm{m^2\,s^{-1}}$. This yields $S_c \approx 0.6$, and therefore

$$\eta_B \approx \eta\sqrt{\frac{1}{0.6}} \approx 1.3\eta. \tag{5.2}$$

Using a typical value of $\varepsilon \approx 10^3$ $\mathrm{m^2\,s^{-3}}$, we conclude that the homogeneity hypothesis is a good approximation for parcel sizes on the order of 2 mm.

Recognizing this fact is crucial when interpreting the results of homogeneous parcel models. It indicates that the requirement for strong updraughts to activate water in the presence of ice particles is *a strictly local phenomenon*, and further implies that these particles must be close enough to share a volume of air smaller than 10 mm^3. Given typical cloud particle concentrations of a few hundred per cubic centimetre, a cube of 2 mm sides would contain one or two particles at any given time.

Our stochastic Lagrangian microphysics model – about to be detailed in the next section – aims to represent the effects of temperature and humidity heterogeneities at typical LES unresolved length scales on the condensational growth of droplets and ice crystals. Specifically, we are interested in how different adiabatic cooling rates (enabled by independent velocity fluctuations for each particle) and the introduction of a turbulent mixing time scale (as opposed to the instantaneous homogenisation implied by the mean-field assumption) can influence rate of glaciation through the WBF mechanism.

Naturally, then, our parcel linear extent Δ lies within the inertial range of cloud turbulence. This is important, because Δ specifies the extent of the sampling volume where all microphysical information is determined. Moreover, is the scale at which our cloud parcel is assumed to acquire its turbulent kinetic energy (TKE) at a given rate ε per unit mass. Together, Δ and ε will enable us to specify – through Kolmogorov scaling in the inertial range – crucial parameters to characterize both the distribution of velocity fluctuations and turbulent mixing mechanism.

5.2 The stochastic parcel model

This work ultimately aims to develop a microphysical scheme that overcomes the systematic neglect of subgrid turbulence effects on microphysics development in coarse-grained simulations. Numerical weather predictions (NWP) have come a long way, with steadily increasing accuracy (Bauer et al., 2015). Nevertheless, solving the primitive equations at the relevant temporal and spacial scales remains a substantial challenge, with cloud microphysics emerging as a critical area for further progress.

Even with the best high-performance computers available today, NWPs heavily rely on cloud parametrization schemes. The grid spacing of synoptic scale high-resolution models lies in the range of 10–25 km, which is often larger than the horizontal extent of individual clouds. For regional forecasts, resolutions of 1–5 km can be used (Kalnay, 2002).

In a recent study, Lam et al. (2023) achieved a landmark in global NWP, with a machine learning–based method trained on reanalysis data, capable o providing 10 days of global forecast in under 1 minute, with an angular resolution of 0.25°

($\approx$ 28 km) and improved accuracy in comparison to production models. Despite the impressive runtime, the model resolution in Lam et al. (2023) is bottlenecked by two factors: The resolution of the training data and the physical hardware limitations for data storage. On regional NWPs, Sze et al. (2022) reached sub-kilometre local resolutions with an unstructured grid model. Their model has variable grid spacing down to 200 meters, a resolution high enough to capture orographic effects.

Although impressive technical achievements, all these models are still orders of magnitude away from the turbulent mixing and microphysical scales relevant for the development of clouds, thus relying entirely on cloud parametrizations and/or historical data for model training and calibration.

On the climate research front, typical filter widths in Large Eddy Simulations (LES), commonly referred to as the Δ length, range from several meters to several tens of meters depending on the total domain size (Kalnay, 2002). Even though resolutions in this range are fine enough to accurately describe mean flow, and even distinguish updraught and downdraught regions within a single cloud, microphysical processes are highly sensitive to environmental heterogeneities at *millimetre* scale, and thus would require much finer resolutions to be explicitly resolved.

In order to study the subgrid microphysical cloudy states, DNS models in small periodic domains, as well as idealized cloud parcel models are often leveraged as ways of representing the smaller scales that remain otherwise unresolved in LES. This is based on the idea that the mean state of a grid box of characteristic size Δ consists of a statistical ensemble of smaller air parcels (or periodic DNS domains) that occupy its volume ($\approx \Delta^3$) [Abade (2025)].

To go beyond the mean-field description and represent sub-grid variability, we consider each cloud particle to be in a small volume of size $v = V/N$, where V is the total volume of the parcel (or grid box) and N is the total number of particles in that volume. As in Vaillancourt et al. (2001), we distinguish the local temperature and vapour mixing ratio – averaged inside the volume v – from their respective parcel averages. Here, we refer to these local quantities as T and Q respectively. Thus, each particle in our domain is given the Lagrangian attributes T_k and Q_k, where the index k denotes the k^{th} particle.

Furthermore, we allow the particle's updraught velocity to deviate from the parcel's mean velocity $\langle w \rangle$. These deviations are accounted for as another super-droplet Lagrangian attribute, w'_k. Figure 5.1 contains a simple illustration of the concept.

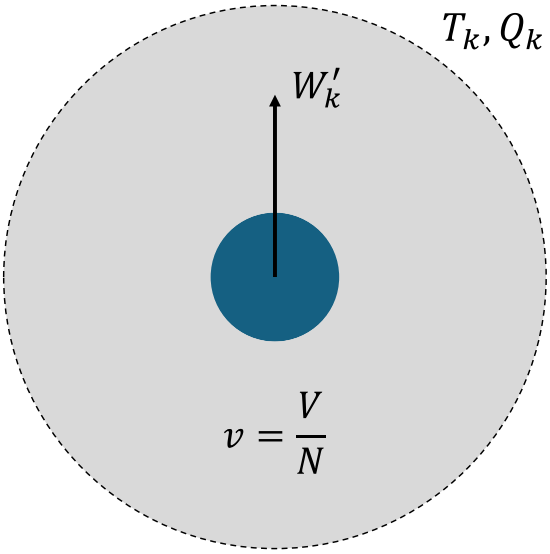

Figure 5.1: Local environmental variables in the stochastic Lagrangian model. The new droplet attribute w_k' accounts for turbulent velocity fluctuations around $\langle w \rangle$. T_k and Q_k are the local temperature and vapour mixing ratio respectively, which interact with the bulk values $\langle T \rangle$ and $\langle Q \rangle$ via the mixing model.

The sources of variation for these new attributes are similar to the ones we had in the previous mean-field model, i.e. adiabatic cooling and latent heat release / absorption affect T_k and phase changes between vapour and the condensed phases will affect Q_k. Finally, we model the process of turbulent mixing as linear relaxation to the mean, i.e., interaction by exchange with the mean or IEM (Pope, 2000). The equations for T_k, and Q_k are as follows:

$$dQ_k = -\frac{Q_k - \langle Q \rangle}{\tau_m} dt - dC_k + dD_k, \tag{5.3}$$

$$dT_k = -\frac{T_k - \langle T \rangle}{\tau_m} dt - \frac{g}{c_p}\Big[\langle w \rangle + w_k'\Big] dt + \frac{L_v}{c_p} dC_k + \frac{L_s}{c_p} dD_k + \frac{L_f}{c_p} dF_k, \tag{5.4}$$

where dC_k, dD_k and dF_k are, respectively, the contributions of condensation, deposition and freezing, given as

$$dC_k = \varphi_k(t) \frac{1}{\rho_d v} \rho_\ell \frac{4\pi}{3} \Big[R_k^3(t + dt) - R_k^3(t)\Big], \tag{5.5}$$

$$dD_k = [1 - \varphi_k(t)] \frac{1}{\rho_d v} \rho_\ell \frac{4\pi}{3} \Big[R_k^3(t + dt) - R_k^3\Big], \tag{5.6}$$

and

$$dF_k = -\frac{1}{\rho_d v}\rho_\ell \frac{4\pi}{3} R_k^3(t)\Big[\varphi_k(t+dt) - \varphi_k(t)\Big], \tag{5.7}$$

where ρ_d is the density of dry air.

The formulation above is analogous to equations 4.27, 4.28, and 4.29 in the homogeneous parcel model, except it is local to each super-droplet. The key difference is in the linear relaxation terms on the RHS of equations 5.3 and 5.4, which models the turbulent mixing. As a consistency check, if we take the mean of those equations, we recover equations 2.16 and 2.19 for the bulk quantities, as the mixing terms vanish and so do the contributions of velocity fluctuations in the adiabatic cooling term.

The τ_m parameter in the mixing terms of equations 5.3 and 5.4 is the characteristic mixing time scale for scalars, an adjustable model parameter.

In order to close the model, we must yet provide an equation for the velocity fluctuations w'_k. For this purpose, we assume that the cloud particles are small enough to have negligible inertia. Additionally, also based on the typical particle length scale, we neglect sedimentation effects. Since the droplet radius (R) is typically in the nanometre to micrometre range, the air flow around haze particles and small droplets has $Re \ll 1$ and thus can be well approximated by the Stokes equations. The equation of motion for such a particle can then be derived by using Stokes' law:

$$\mathbf{F}_h = 6\pi\mu R\Big\{\mathbf{U}[\mathbf{X}(t),t] - \mathbf{V}(t)\Big\}, \tag{5.8}$$

where μ is the air viscosity, $\mathbf{V}(t)$ is the particle velocity and $\mathbf{U}[\mathbf{X}(t),t]$ is the flow velocity at the particle position $\mathbf{X}$(t). By virtue of Newton's second law and after some rearrangement, the equation for $\mathbf{V}(t)$ reads

$$\dot{\mathbf{V}} = \frac{\mathbf{U} - \mathbf{V}}{\tau_p} + \mathbf{g}, \tag{5.9}$$

where $\tau_p = 2\rho_\ell R^2/9\mu$ is the particle response time, and ρ_ℓ is the liquid water density, considered to be equivalent to the particle's density.

For the purpose of this analysis, equation 5.9 may be scaled with the velocity and time scales associated with the parcel's (or grid box) linear extent Δ. Let the characteristic velocity of Δ-sized eddies be U_Δ. It follows, that the characteristic eddy turnover time is $\tau_\Delta = \Delta/U_\Delta$. Rewriting equation 5.9 in terms of the dimensionless velocities $\mathbf{V}^* = \mathbf{V}/U_\Delta$ and $\mathbf{U}^* = \mathbf{U}/U_\Delta$, and solving for $\mathbf{V}^*$ yields

$$\mathbf{V}^* = \mathbf{U}^* - St\dot{\mathbf{V}}^* + Sv\hat{\mathbf{e}}_g, \tag{5.10}$$

where $St = \tau_p/\tau_\Delta$ is the Stokes number, $Sv = \tau_p g/U_\Delta$ is the particle settling number, and $\tau_p g$ is the particle's terminal sedimentation velocity.

Since Δ is assumed to fall within the inertial range, then $U_\Delta = (\varepsilon\Delta)^{1/3}$, and $\tau_\Delta = (\Delta^2/\varepsilon)^{1/3}$, where ε is the turbulent kinetic energy (TKE) dissipation rate. In turbulent stratocumulus clouds, a typical value of ε lies around 10^{-3} $m^2 s^{-3}$ (Pinsky et al., 2008), Assuming a grid spacing of 100 m, typical in LES cloud simulations, and a particle size of 10 µm, $St \approx 6 \times 10^{-6}$ and $Sv \approx 2.7 \times 10^{-2}$. We may then approximate equation 5.10 by $\mathbf{V}^* = \mathbf{U}^*$, which is equivalent to taking the limit when $\tau_p \to 0$. This neglect of the particle's inertia, resulting in the assumption that its velocity $\mathbf{V}$ is indistinguishable from $\mathbf{U}$, is referred to in classical literature as the *tracer limit*. In this work, we have termed this the *mechanical equilibrium* assumption (Lozar and Mellado, 2014), when discussing bulk formulations in chapter 3. This assumption automatically implies that the distribution of $w_k \equiv \mathbf{V}^* \cdot \hat{\mathbf{e}}_z$ is identical to that of $\mathbf{U}^* \cdot \hat{\mathbf{e}}_z$.

We describe w'_k by means of a simple stochastic process (Haworth and Pope, 2011) given by

$$dw'_k = -\frac{w'_k}{\tau} + \sqrt{\frac{2\sigma^2}{\tau}} dW_k, \tag{5.11}$$

where τ is the Lagrangian integral velocity time scale and $\sigma^2 = \left\langle {w'_k}^2 \right\rangle$ is the vertical velocity variance. W_k denotes the Wiener process associated with the k^{th} particle (Van Kampen, 2007) and $dW_k = W_k(t+dt) - W_k(t)$ denotes its increment. The distribution of dW_k is Gaussian with $\langle dW_k \rangle = 0$ and $\langle (dW_k)^2 \rangle = dt$.

To fully define the stochastic process in equation 5.11, it is required to specify τ and σ^2, which are defined by the turbulence statistics inside our parcel domain. As mentioned in the beginning of this chapter, this is where the parcel's linear size Δ comes in as a crucial model parameter. Through Kolmogorov scaling for the inertial turbulence regime, and prescribing a TKE dissipation rate ε per unit mass, we may estimate these quantities as

$$\tau \sim \varepsilon^{-1/3}\Delta^{2/3}, \tag{5.12}$$

$$\sigma^2 \sim (\varepsilon\Delta)^{2/3}. \tag{5.13}$$

Finally, we may assume our mixing time scale τ_m relates to τ by

$$\tau_m = C_\tau \tau, \tag{5.14}$$

where C_τ is the scalar-to-velocity time scale ratio. The value of C_τ is flow-dependent, and estimating it is a non-trivial task that lies outside the scope of this thesis. Instead, we shall run a series of simulations over a wide range of values for C_τ and demonstrate that the stochastic parcel's mixed-phase persistence is robust.

In the context of an LES simulation, Δ would represent the grid box linear size and would therefore be a known – and in general constant – parameter defined by the mesh geometry. In our parcel simulation, Δ is defined as constant in time (parcel adiabatic expansion is neglected.). However, because we have implemented random vertical velocity fluctuations, this size grows by turbulent diffusion with the square root of time (Einstein, 1905). This poses an inconsistency with our base assumptions. As particles are advected by the turbulent velocity fluctuations, they eventually escape the sampling volume defined by Δ and spread vertically, artificially broadening the supersaturation distribution, while still interacting with each other via the turbulent mixing model at the *same* fixed mixing time scale. In practice, this is equivalent to sampling microphysical information from droplets that are far outside the boundaries of our Δ-sized parcel, while keeping all the model parameters constant. An in-depth discussion about this *implicit non-local sampling* and alternatives to address it under different simulation frameworks is provided in Abade (2025).

It is clear that this unbounded particle motion introduces several inconsistencies and contradictions in our formulation, even violating one of the basic premises of our parcel framework: that it is a closed system. To address this, we introduce reflective boundary conditions that keep our sampling volume (or rather the vertical extent across which particles are located) at the specified value. In doing so, we preserve not only the physical coherence of our model, but also the analogy with spatially discretized flow simulations, where grid box dimensions are fixed. To do that, we define

$$z'_k(t) = z_k(t) - \langle z \rangle(t) = \int_0^t w'_k(t)dt, \tag{5.15}$$

and enforce the condition $|z'_k| \leq L/2$ by means of reflective boundary conditions in both position and velocity.

5.3 Simulation Setup

With the objective of comparing the results of our stochastic model to those of the models previously described in this thesis, we have divided the simulations into three groups. In the first, parcels are under uniform vertical motion with varying velocities. In the second group, the parcel starts ascending uniformly from ground level and switches to oscillatory motion above the lifting condensation level.

We impose this motion by specifying a time dependent vertical velocity $\langle w(t)\rangle$ according to

$$\langle w(t)\rangle = \begin{cases} W & \text{for } t < t^* \\ W\cos[\Omega(t-t*)] & \text{for } t \geq t^* \end{cases}, \tag{5.16}$$

where $t^* = (\bar{z}-z_0)/W$ is the time it takes for the parcel to travel from its initial position z_0 to its average oscillation height $\bar{z}$. The oscillation frequency Ω is obtained by dividing the maximum velocity W by the oscillation amplitude Δz. Figure 5.2 shows the time evolution of the parcel height, as well as the corresponding variations in mean temperature. The objective here is to reproduce the periodicity of convective cells. By doing so, we are able to analyze the evolution of the system for long periods of time and assess the longevity of the mixed-phase state. In both the first and second groups of simulations, ice particles are initially not present and come into existence via the mechanism of immersion freezing. In the third group of simulations, we turned off the freezing mechanism and considered prescribed fractions of ice particles. Additionally we experimented with different vertical velocities and TKE dissipation rates to evaluate the influence of those parameters in the glaciation rate. For this group of simulations, the parcel starts above cloud base with $r_i = 0$ and all water droplets with a radius of 10 µm. The main differences between the three simulation groups are summarized in table 5.1 below.

5.4 Phase Partitioning and Supersaturation in a Steadily Rising Parcel

We begin by analysing results for the parcel in uniform upward motion. This framework provides a steady source of supersaturation due to a practically constant adiabatic cooling rate. In the previous chapter we saw that the traditional mean-field approach yields a very unstable system, in which the glaciation process by the WBF mechanism causes an inversion in the parcel's condensate composition (see fig. 4.5). In contrast, the stochastic model yields a more stable phase partitioning, as well as better agreement with the temperature-parametrized phase partitioning used in the bulk model.

The key to greater phase stability present in the stochastic model lies in its heterogeneity. With each super-particle having its own set of environmental variables, namely T_k and Q_k, one may define not only the average parcel saturation values $\langle S_\ell\rangle$ and $\langle S_i\rangle$, but also averages conditional to particle phase, i.e,

Table 5.1: Model parameters used in the three sets of simulations. Cloud parcels of linear extent $\Delta = 100$ m and total particle concentration of 200 mg^{-1} unless otherwise specified.

Simulation group	Parcel motion	W [$\mathrm{m\,s^{-1}}$]	ε [$\mathrm{m^2\,s^{-3}}$][a]	ϕ_i	INP fraction
1	Uniform ascent	0.5, 1, 2, 4	10^{-3}	prognosed	10%
2	Oscillation above cloud base [b]	0.5	10^{-3}	prognosed	10%
3	Oscillation above cloud base	0, 0.5, 1, 2, 4	$10^{-4}, 10^{-3}$	0.1%, 1%, 5%, 10%	-

[a] Only applies to stochastic simulations.

[b] Oscillation above cloud base follows ascent from the ground.

$$\langle S_\ell \rangle_\ell = \frac{\sum_{k=1}^{N} \varphi_k S_{\ell,k}}{\sum_{k=1}^{N} \varphi_k}, \tag{5.17}$$

$$\langle S_i \rangle_i = \frac{\sum_{k=1}^{N} (1-\varphi_k) S_{i,k}}{\sum_{k=1}^{N} (1-\varphi_k)}, \tag{5.18}$$

where φ_k is the particle phase indicator, defined in Section 4.4, while $S_{\ell,k}$ and $S_{i,k}$ are the local supersaturation values relative to water and ice respectively.

Under the homogeneity assumption, the conditional and unconditional average saturations are equivalent (i.e. $\langle S_\ell \rangle = \langle S_\ell \rangle_\ell$ and $\langle S_i \rangle = \langle S_i \rangle_i$). A relationship between the saturation values over water and ice can be obtained from equation 4.6 and reads

$$\langle S_i \rangle \approx \langle \gamma(T) \rangle \langle S_\ell \rangle + \langle \gamma(T) \rangle - 1, \tag{5.19}$$

where $\gamma(T) = e_\ell(T)/e_i(T) \geq 1$ is the ratio between the saturation vapour pressures over liquid water and ice respectively. The approximation in equation 5.19 comes from assuming that $\langle \gamma(T) S_\ell \rangle \approx \langle \gamma(T) \rangle \langle S_\ell \rangle$. This relation holds exactly under the assumption of a homogeneous environment, but only approximately if we consider the temperature and humidity inhomogeneities present in real clouds. As for the

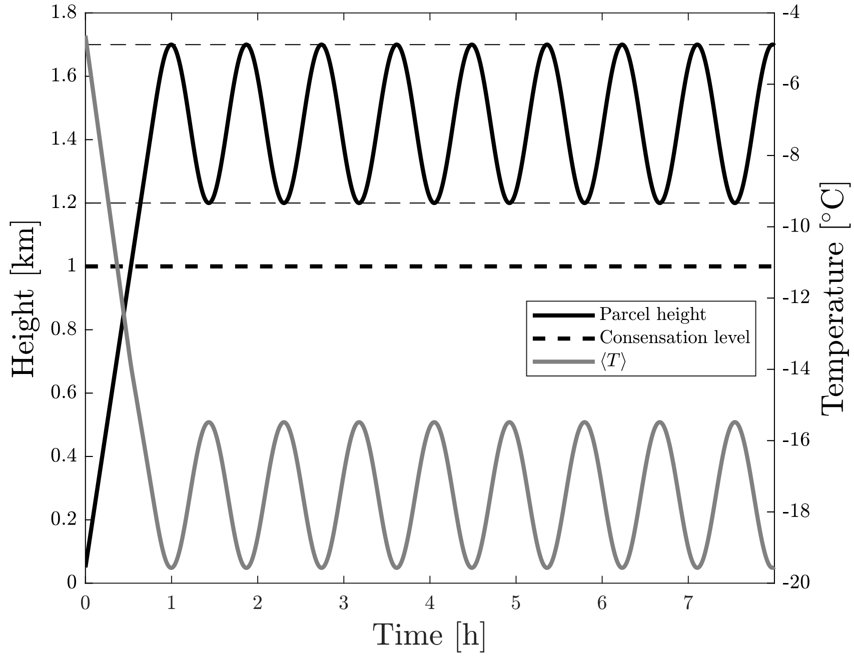

Figure 5.2: Time evolution of parcel height and average temperature for simulation group 2. The oscillatory movement above cloud base mimics the natural convection in clouds. Average oscillation position $\bar{z} = 1450$ m and oscillation amplitude $\Delta z = 250m$. External environmental conditions: $\theta = 269K$, $q_v = 1.5 \times 10^{-3}$.

conditional averages, there is no trivial algebraic relation that would allow us to diagnose them from the bulk (unconditional) averages, as these depend on the intricate turbulent mixing mechanism that couples with the microphysical model.

In general, the conditions for the WBF mechanism to occur on a bulk scale (i.e. effectively increasing the ice to liquid water proportion) are written in terms of the *conditional* averages, not the unconditional ones, i.e.,

$$\langle S_\ell \rangle_\ell \leq 0 \quad \text{and} \quad \langle S_i \rangle_i \geq 0. \tag{5.20}$$

Otherwise, the mechanism might act locally, but with no large scale glaciation effect.

Figure 5.4 shows the profiles of conditional and unconditional average saturation over liquid water and ice for the homogeneous and stochastic models. Apart from the sudden inversion in the slope of $\langle S_i \rangle$ in the homogeneous model (figure 5.4c), caused by liquid water depletion at $z \approx 2.75km$, both models exhibit qualitatively equivalent profiles, with $\langle S_i \rangle$ exceeding $\langle S_\ell \rangle$ by a few orders of magni-

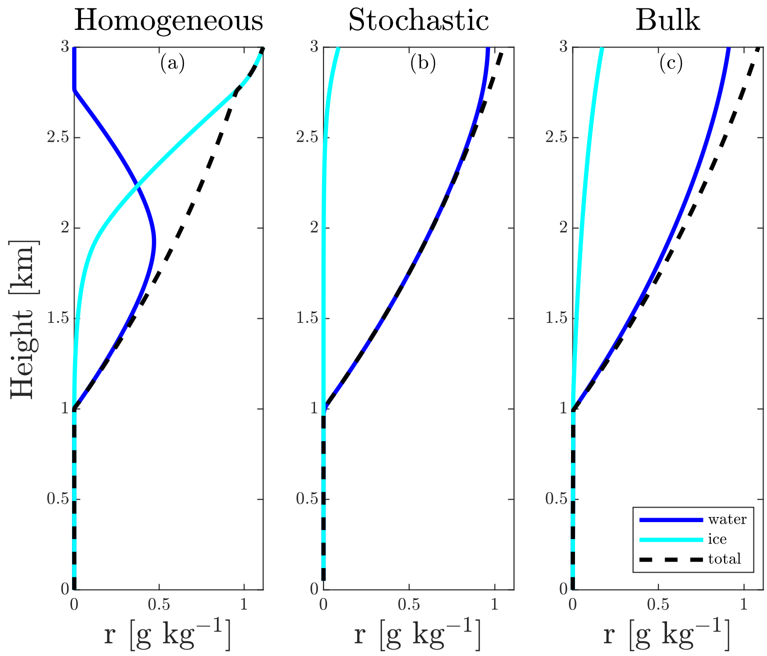

Figure 5.3: Profiles of liquid and ice mixing ratio for different models in the ascending parcel framework. (a) - Homogeneous parcel with super-droplets (deterministic). (b) - Stochastic Lagrangian parcel model. (c) - Bulk microphysics. The stochastic model presents a more stable phase partitioning and better agreement with the bulk model.

tude and $\langle S_\ell \rangle$ eventually becoming negative at around 2km. In the homogeneous model, this evidently leads to a fast glaciation of the entire parcel. In the stochastic model, however, we observe that the conditional averages $\langle S_\ell \rangle_\ell$ and $\langle S_i \rangle_i$ differ substantially from their bulk counterparts. For the ice phase, the bulk average is driven by the significantly larger liquid droplet population, while the conditional average is much lower due to the fact that ice crystals will consume the excess vapour much faster than the mixing mechanism is able to deliver it, driving the local values of S_i closer to saturation over ice. As for the liquid phase, the relation $\langle S_\ell \rangle_\ell \approx \langle S_\ell \rangle$ holds true only until the concentration of ice crystals is no longer negligible. As more and more droplets freeze due to temperature decrease, the two averages diverge, with $\langle S_\ell \rangle_\ell$ remaining positive.

Regarding the sensitivity to variations in the mean updraught velocity $\langle W \rangle$, the homogeneous and stochastic parcels respond differently. Figure 5.5 shows the results of the mixing ratios as a function of height for different values of $\langle W \rangle$ ranging from 0.5 to 4 $\mathrm{m\,s^{-1}}$. For the homogeneous parcel, r_ℓ (fig. 5.5a) is highly

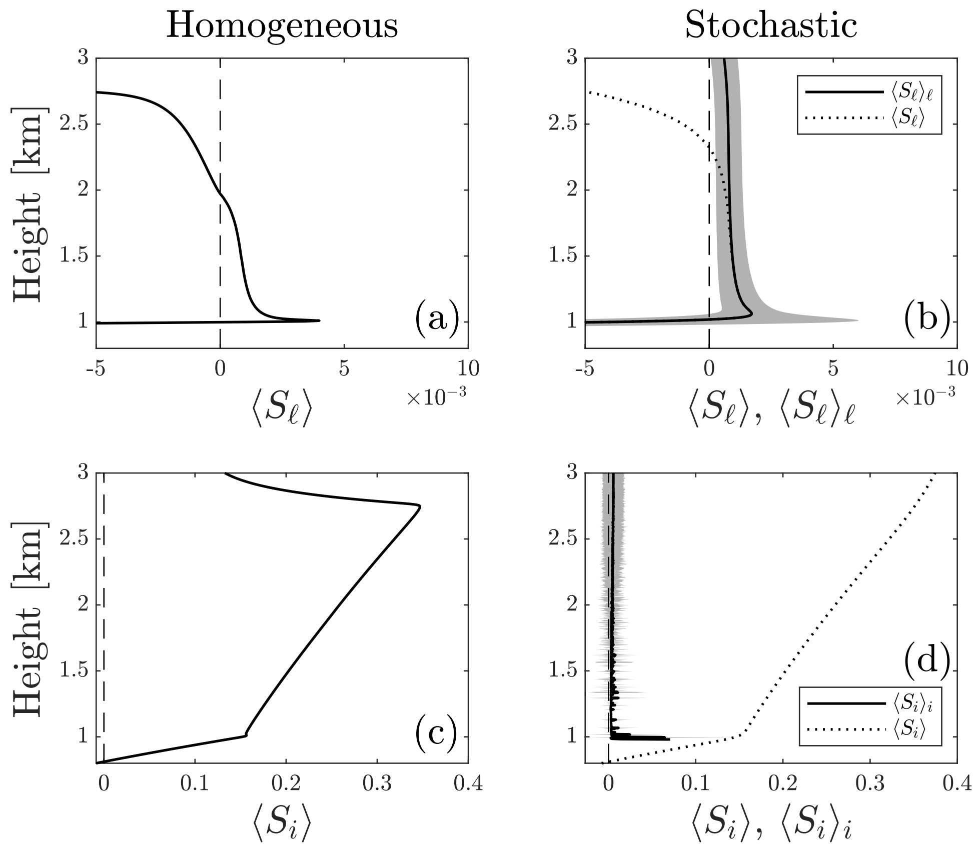

Figure 5.4: Vertical profiles of supersaturation (conditional and unconditional) for both homogeneous and stochastic models. The grey shades on panels (b) and (d) have the width of two standard deviations. The stochastic model allows for the distinction between the overall (or unconditional) average saturation $\langle S_\ell \rangle$ and the conditional average $\langle S_\ell \rangle_\ell$, computed only over the population of liquid droplets [see plot (b)]. The latter remains positive during the uniform ascent – which explains the sustained increase in r_ℓ – while $\langle S_\ell \rangle$ becomes negative, influenced by ice particles. In plot (d) it is shown that the local values of S_i seen by ice particles remain close to saturation conditions, despite the high values of the unconditional average $\langle S_i \rangle$. This explains the pronounced decrease in ice growth in comparison to the homogeneous parcel.

sensitive to $\langle W \rangle$, with higher velocities causing later onset of the WBF mechanism. For the two lowest velocities (i.e. 0.5 and 1.0 $\mathrm{m\,s^{-1}}$) the parcel is unable to maintain its mixed-phase state and a complete glaciation occurs before the homogeneous freezing temperature (-38 °C) is reached at about 4km. This is the expected behaviour under the mean-field assumption, in which mean updraught velocity is known to have a strong influence in the persistence time of the liquid phase (Heymsfield (1977), Korolev and Mazin (2003)). In the stochastic model, we observe a monotonic behaviour of r_ℓ even for the lowest value of $\langle W \rangle$ and a lower overall sensitivity to vertical velocity. In the profiles of ice mixing ratio (fig. 5.5b), we can see that ice growth is strongly suppressed in comparison to the homogeneous parcel.

By inspecting the saturation vertical profiles in fig. 5.5c we observe that both models attain the same quasi-equilibrium value after droplet activation. In the homogeneous model, this quasi-equilibrium state is short-lived, with $\langle S_\ell \rangle_\ell$ becoming negative between 2km (for $W = 0.5 \ \mathrm{m\,s^{-1}}$) and 2.5km (for $W = 4 \ \mathrm{m\,s^{-1}}$). In contrast, the stochastic model maintains $\langle S_\ell \rangle_\ell > 0$ around its quasi-equilibrium value until homogeneous freezing occurs, which explains the monotonic growth of liquid water despite the presence of ice.

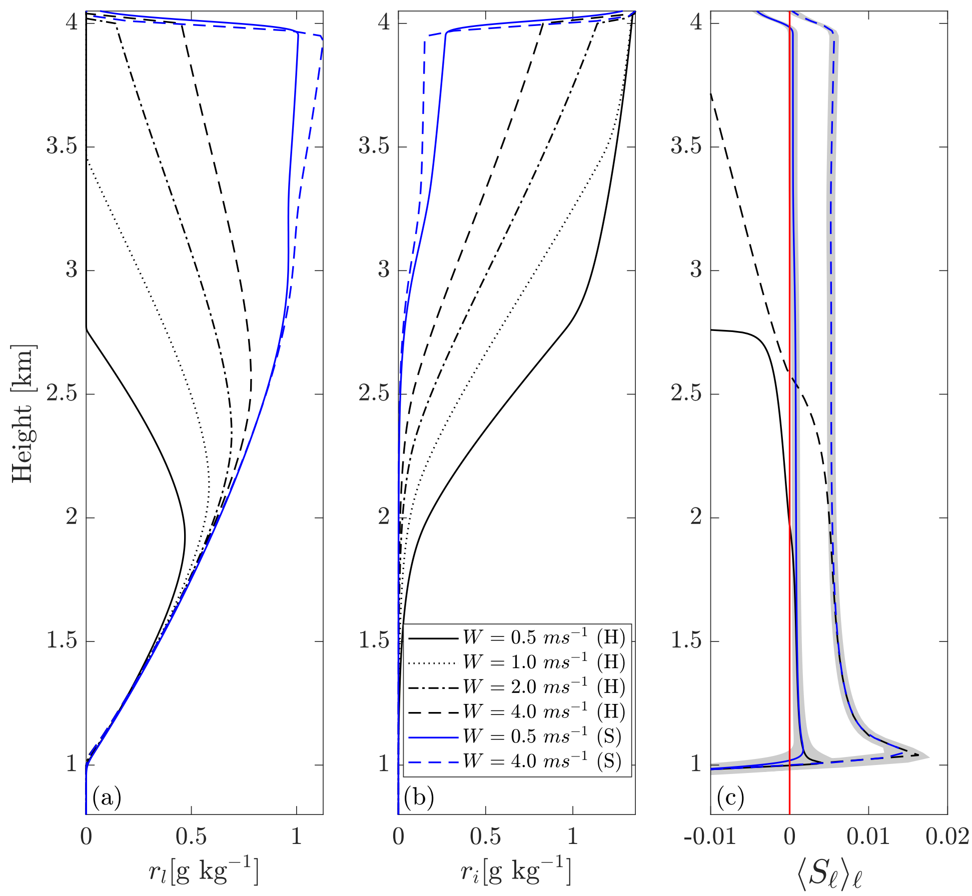

Figure 5.5: Mixing ratios r_ℓ and r_i and conditional average supersaturation $\langle S_\ell \rangle_\ell$ versus height for homogeneous (H) and stochastic (S) models in uniform ascent. (a) Liquid water mixing ratio; (b) Ice mixing ratio; (c) Mean supersaturation over liquid water experienced by liquid droplets. A greater vertical velocity will increase the height at which the water mixing ratio starts to reduce, by sustaining the liquid water saturation for longer. The stochastic parcel sustains a positive and quasi-steady value of $\langle S_\ell \rangle_\ell$ despite the presence of ice particles, even at relatively slow updraught ($W = 0.5\ \mathrm{m\,s^{-1}}$).

5.5 Stochastic droplet activation in turbulent environments

So far we have observed that our stochastic Lagrangian microphysics model upholds a significantly larger portion of liquid water in the presence of ice. To better understand the reason of this mixed-phase resilience, is it necessary to understand the role of turbulent fluctuations in cloud particle activation.

In an experimental and theoretical study, Prabhakaran et al. (2020) investigated CCN activation under different turbulent regimes. Through experiments in a turbulent cloud chamber, they were able to produce cloud formation in a mean-subsaturated environment, a result not reproducible by mean-field models. They interpret these results through the lens of a theoretical model of stochastic activation, developed for this purpose, and explicitly recognize the need to move beyond the uniform-parcel view of CCN activation, pointing to turbulence-based approaches as the path to better understanding interactions between aerosols, cloud droplets and turbulence.

In Prabhakaran et al. (2020), three main stochastic activation regimes are identified and classified. These regimes are schematically represented in figure 5.6, where the black vertical line marks the critical (or activation) supersaturation value, S_c, here treated as a single value for simplicity. We remind that our model exhibits a range of S_c because our aerosol population is sampled from an prescribed size distribution.

In regime 1, the average supersaturation is well above the critical value, such that $|\langle S_\ell \rangle - S_c| \gg \sigma_{S_\ell}$. In other words, no significant portion of the droplet population is found under the critical supersaturation value. In this case, we say the activation is mean-dominated, with fluctuations playing a minor role.

Regime 2 is characterized by a mean-supersaturated environment where $|\langle S_\ell \rangle - S_c| \sim \sigma_{S_\ell}$. In this scenario, a significant portion of the cloud particles experience momentary, fluctuation-driven subsaturation, which may lead to deactivation or suppress the activation of haze particles. This regime is called fluctuation-influenced activation, and may result in reduced cloud droplet concentration despite the mean-supersaturated environment.

Regime 3 is analogous to regime 2, but associated with a mean-subsaturated environment. Here – similarly to the fluctuation-influenced regime – we also observe $|\langle S_\ell \rangle - S_c| \sim \sigma_{S_\ell}$, causing the S_ℓ distribution to be divided in two regions around S_c. For this scenario, however, stochastic fluctuations in S_ℓ *enable* droplet activation events, instead of suppressing them. Regime 3 is called fluctuation-dominated activation. Under these conditions allow cloud formation in mean-subsaturated environments, and are able to explain the results obtained by Prabhakaran et al. (2020) in their cloud chamber experiment.

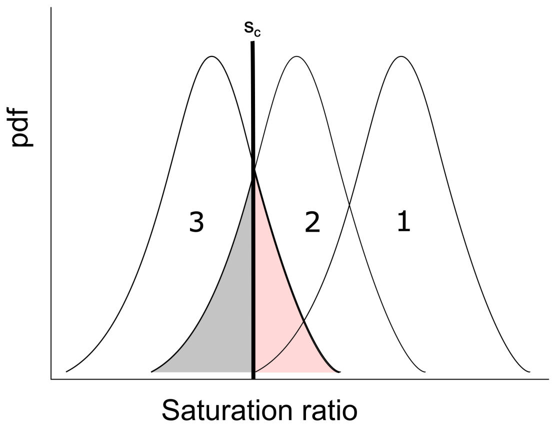

Figure 5.6: Supersaturation distributions under different activation regimes. Regime 1 is mean-dominated activation, where fluctuations play a minor role. Regime 2 is called fluctuation-influenced activation, characterized by $\langle S \rangle > 0$ with fluctuation-driven deactivation, and activation suppression. Regime 3 is fluctuation-dominated activation, where droplets may activate under $\langle S \rangle < 0$ through stochastic fluctuations. Source: Prabhakaran et al. (2020).

Understanding these activation regimes is particularly useful for understanding the resilience of the liquid phase in our stochastic model. As in the turbulent cloud chamber – and in contrast to mean-field microphysical models – the thermodynamic variables in our stochastic parcel are not characterized by single values, but by probability distributions.

Figure 5.7 shows in detail the moment of droplet activation, when the parcel crosses lifting condensation level (LCL), for two scenarios: pristine and polluted. These scenarios differ essentially in CCN concentration, where the polluted case has a concentration of 1000 mg^{-1}, while the pristine case has 200 mg^{-1}.

For the pristine case (top plots), both models activate the entire droplet population. However, in the stochastic model, activation events gradually occur over the course of a 200m parcel displacement. In the homogeneous parcel, activation occurs for all droplets almost simultaneously (see fig. 5.7a). This spread of the activation zone happens due to the stochastic fluctuations of temperature and vapour mixing ratio, induced by the turbulent velocity fluctuations in the model. The resulting distribution of S_ℓ is wide enough to allow the onset of droplet activation a few tens of meters before the LCL is reached, i.e. droplet activation in the stochastic model is initially *fluctuation-dominated.*

As the parcel enters the activation region, the supersaturation distribution significantly broadens. This happens because activated droplets quickly consume the

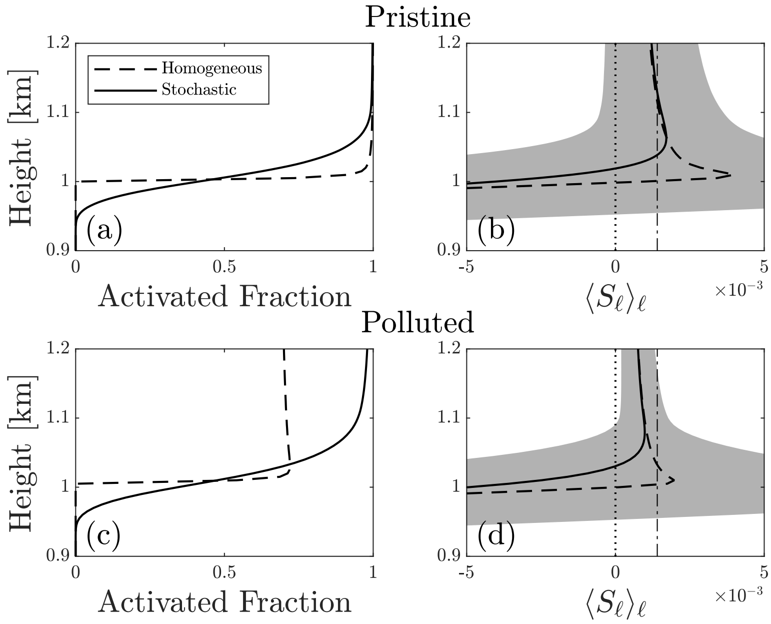

Figure 5.7: (a), (c) - Vertical profiles of the fraction of activated droplets; (b), (d) - Conditional average supersaturation $\langle S_\ell \rangle_\ell$ over liquid water experienced by the droplets. Results are for homogeneous and stochastic parcels, ascending with constant speed of 0.5 $\mathrm{m\,s^{-1}}$, for two total cloud particle concentrations: pristine (200 $\mathrm{mg^{-1}}$) and polluted (1,000 $\mathrm{mg^{-1}}$). The shading around the solid lines (corresponding to the stochastic parcel) in panels (b) and (d) has a width of twice the standard deviation σ_{S_ℓ} of S_ℓ experienced by the population of liquid droplets. The vertical dash-dotted line in panels (b) and (d) indicates the critical supersaturation S_c corresponding to $R_d = 75$ nm (the mode of the assumed R_d distribution) and $\kappa = 0.6$. The droplet activation in stochastic parcels is “fluctuation-influenced”, whereas in homogeneous parcels the droplet activation is “mean-dominated”. This explains why the stochastic parcels activate all available cloud condensation nuclei under both pristine and polluted conditions for the set of parameters considered in these simulations.

vapour in their vicinity, while droplets yet to be activated experience high supersaturation. Likewise, as the parcel leaves the activation zone, a considerable part of the droplets is still not activated, despite the mean-supersaturated environment. This portion of the activation zone is *fluctuation-influenced*.

Towards the end of the activation region, the distribution becomes narrower and σ_{S_ℓ} tends to a quasi-equilibrium value. The same happens in the polluted case, with a lower quasi-equilibrium σ_{S_ℓ} value due to the faster phase relaxation time caused by increased particle concentration.

In contrast, the homogeneous model droplet activation is *mean-dominated*. With every particle experiencing the same mean conditions, differences in activation time arise solely from small variations of the critical supersaturation value (S_c), as a consequence of the distribution of dry radii (see equations 4.9 and 4.11). However, the maximum value of S_c is approximately 2.6×10^{-3}, attained by the parcel only a couple of meters after LCL ($\langle S_\ell \rangle_\ell = 0$) is reached, resulting in the activation of the entire droplet population in a very short time span.

Another aspect of the stochastic droplet activation is that the mean supersaturation has a lower peak value. The early formed droplets, activated at $z < LCL$ gradually increase the consumption of water vapour along the activation zone, thus reducing the peak in $\langle S_\ell \rangle_\ell$. At the same time, this has a diminished influence on the activation of remaining (late) droplets, as the stochastic fluctuations in their local environments allow them to activate despite the lower mean value of supersaturation. The homogeneous model, on the other hand, maintains a steep growth of $\langle S_\ell \rangle_\ell$ until activation happens almost simultaneously across the parcel, resulting in a higher and sharper supersaturation peak (see figs. 5.7b and 5.7d).

In the Polluted scenario, the droplets in the homogeneous parcel activate partially (about 72%), as a result of the shorter phase relaxation time (i.e. faster microphysics) caused by the increased droplet concentration. The lower τ_ℓ drives a reduction in the supersaturation peak (fig. 5.7d), which leads to a considerable part of the droplet population never reaching their critical supersaturation and remaining as haze particles. This is commonly referred to as the *lucky droplet effect*, in which the largest CCN activate first, preventing smaller ones from doing the same. Even though this effect makes perfect physical sense from a qualitative standpoint, it is quantitatively overestimated under the mean-field approximation for large collections of droplets. The constraint of having every single particle subject to the same supersaturation implies that every particle whose critical supersaturation S_c is larger than $\langle S_\ell \rangle_{max}$ will not activate.

The so-called lucky droplet effect is also present in the stochastic parcel, though significantly weaker. Instead of activation suppression, droplets with lower S_c experience an *activation delay*, resulting in the activation zone being asymmetrically positioned in respect to the LCL. Similarly to the homogeneous parcel, in the stochastic parcel a fraction of the droplets was unable to activate, albeit a much smaller one, about 0.12% (fig. 5.7c). The more efficient droplet activation in the stochastic model can be explained by a separation of time scales. The introduction of a mixing time scale and the distinction between local and average conditions enables early droplet activation without immediate changes in $\langle S_\ell \rangle$. Activation is a fast process, which enables droplets to overcome the activation barrier (S_c) in a short time span, without significant changes in $\langle S_\ell \rangle$.

Due to the decoupling of local and bulk values of supersaturation, as well as the introduction of a mixing time scale, the effect of early droplet activation on $\langle S_\ell \rangle_\ell$ is delayed, making it possible to activate a larger portion of droplets despite the higher droplet concentration.

Finally, figure 5.7b,d shows that the variance of S_ℓ does not monotonically decay, but attains a quasi-steady value after droplet activation. This results from a balance between variance decay, driven by the microphysics and mixing, and variance production stemming from vertical velocity fluctuations via the adiabatic cooling/warming effect. In the polluted case (fig. 5.7d), the variance is smaller due to the shorted phase-relaxation time (faster microphysics).

5.5.1 Oscillating Parcel in the Cloud Layer

In this section, we analyse the results of the second group of simulations performed (see table 5.1), in which we prescribe an oscillatory motion to the parcel after it crosses the lifting condensation level. Our goal here is to observe the long term behaviour of our stochastic microphysics formulation under periodic forcing.

Figure 5.8 shows the evolution of liquid water fraction with time. The dashed blue line shows the behaviour of the homogeneous model, which transitions from pure liquid to pure ice in a matter of minutes. As in the previous case, we have the results for the bulk model as a reference, this time marked with the dashed black line. Because of the neglected time scales of condensation and mixing, this model is not time-sensitive and the properties of the parcel depend on height alone. For this reason, the liquid water fraction oscillates around a constant mean value, so long as the parcel's height does the same. We recall that the parametrization of liquid fraction used in this model attempts to reproduce observed steady-state partitioning which is the net result of a multitude of unrepresented processes. Finally, we have the results of the stochastic model, which exhibits a robustly persistent mixed-phase state, consisting predominantly of liquid water for a wide range of values for the C_τ proportionality constant (see eq. 5.14). Logically, lower values of C_τ (i.e. faster turbulent mixing) lead to faster glaciation rates, as this intensifies the mass exchange between liquid and ice phases via vapour mixing. In this stochastic scenario, the WBF mechanism is intermittently active, causing the parcel to gradually decrease its liquid water fraction after each cycle. By comparing the peaks and troughs of the stochastic model to those of the bulk model, we notice that they are in opposition of phase. This is because in the bulk model, μ is a monotonically increasing function of temperature, which in turn decreases with height. This makes it so that μ peaks occur at the end of downdraughts, where the parcel is warmer, while troughs occur at the end of

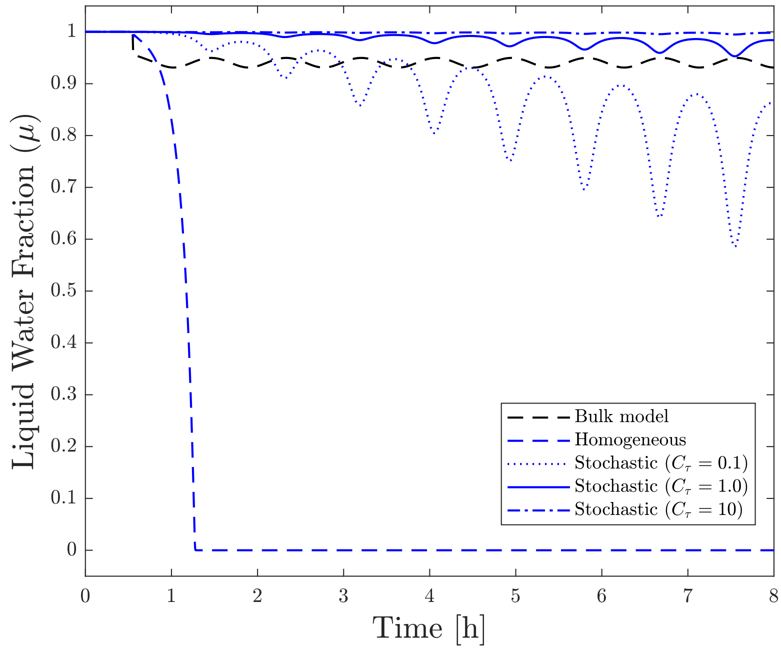

Figure 5.8: Liquid water fraction μ as a function of time for homogeneous, stochastic and bulk models. The stochastic parcel remains as a mixed-phase system for many hours, with predominance of the water phase for a wide range of values of the constant C_τ. Similarly, so does the bulk mode, which counts on a parametrisation that artificially maintains supercooled water. In contrast, the homogeneous parcel exhibits a sharp transition from water to ice-only cloud.

updraughts, when temperature is the lowest. Our stochastic model on the other hand, is time-dependent and its state depends on the history of motion. During updraughts, positive supersaturation is generated, leading to the activation of water droplets. This causes the local maxima of μ to coincide with the height maxima. Conversely, water droplets evaporate during downdraughts, making μ reach its local minima at the parcel's lowest position.

Figure 5.9 shows the bulk values of supersaturation versus height for both homogeneous and stochastic parcels. For the stochastic parcel, conditional averages are shown, i.e. $\langle S_\ell \rangle_\ell$ considers only the water droplet population, and $\langle S_i \rangle_i$ only ice particles. For the homogeneous case, the conditional and unconditional averages coincide. In both models, ice crystals are formed during the first updraught, with the difference that, in the homogeneous model, these crystals experience very high supersaturation and thus grow very rapidly. As a result, the parcel remains

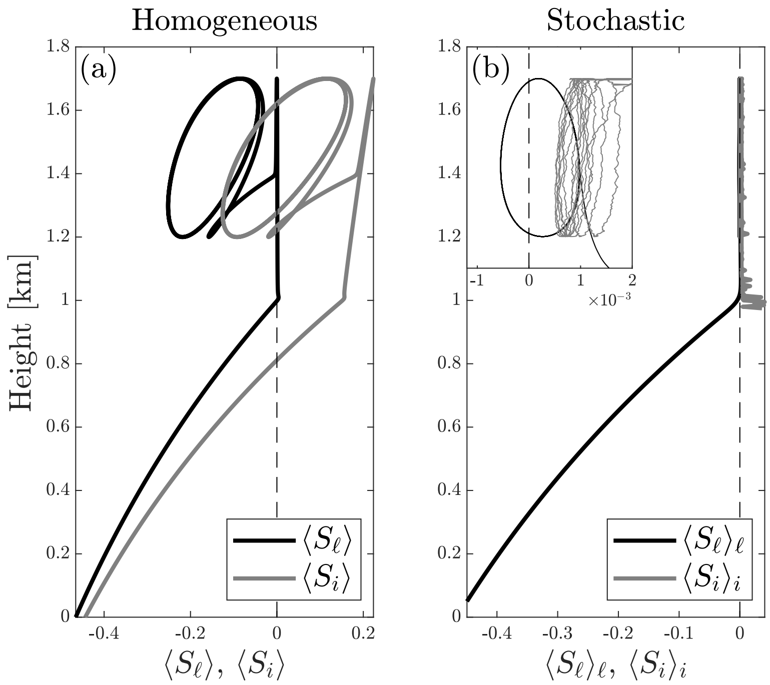

Figure 5.9: Average parcel supersaturations versus height for mixed-phase cloud parcels in oscillatory motion: (a) homogeneous parcel; (b) stochastic parcel. The inset in (b) shows the data for $\langle S_\ell \rangle_\ell$ and $\langle S_i \rangle_i$ in more detail for the stochastic parcel, indicating that the condition in equation 5.20 for the Wegener-Bergeron-Findeisen process applies (on average) during downdraughts only.

sub-saturated with respect to liquid water for the remainder of the simulation. In contrast, ice crystals in the stochastic model experience high supersaturation only momentarily after their formation, after which local values of S_i are brought closer to saturation. Likewise, S_ℓ also remains close to saturation. On the inset in figure 5.9b, we observe that water droplets experience positive supersaturation on average during updraughts, while negative supersaturation during downdraughts, which is in agreement with the periodic behaviour of μ in figure 5.8.

The time series of $\langle S_\ell \rangle_\ell$ and $\langle S_i \rangle_i$ for the stochastic model are shown in figure 5.10a, where once again we observe the intermittency of the WBF conditions, with $\langle S_i \rangle_i > 0$ at all times and $\langle S_\ell \rangle_\ell$ oscillating between positive and negative values. In contrast, the homogeneous model becomes irreversibly under-saturated with respect to liquid water soon after the first updraught. The spikes in $\langle S_i \rangle_i$ result from freezing events, after which the newly formed ice crystals quickly consume the excess of vapour around them. As the population of ice crystals increases, subsequent freezing events have diminishing influence on the average supersatu-

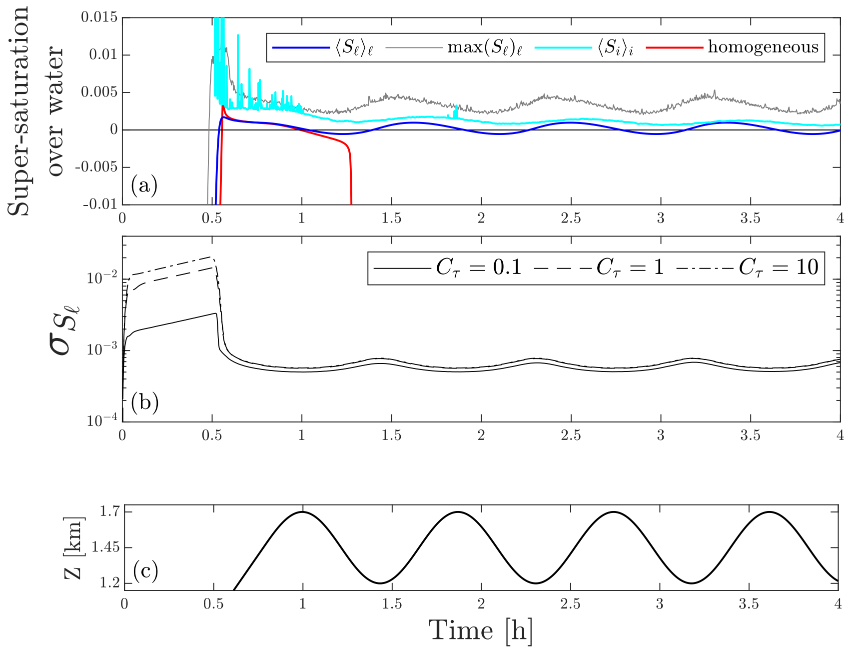

Figure 5.10: (a) Supersaturations experienced by cloud particles in the oscillating stochastic parcel. The dark blue line shows the conditional average supersaturation over liquid $\langle S_\ell \rangle_\ell$ experienced by the droplet population. The light blue line shows the conditional average supersaturation over ice $\langle S_i \rangle_i$ experienced by ice particles. Sharp peaks indicate the formation of new ice particles via heterogeneous freezing. The grey line shows the instantaneous maximum value (among the population of liquid droplets) of the supersaturation over liquid, which is always positive. The evolution of $\langle S_\ell \rangle$ for the homogeneous case is shown in red for reference. (b) Time evolution of the standard deviation σ_{S_ℓ} in the liquid water supersaturation (sampled over liquid droplets) for different values of the scalar-to-velocity time scale ratio C_τ. The shorter the mixing time scale is (smaller C_τ) the smaller is the dispersion in S_ℓ , as faster turbulent mixing more effectively damps out supersaturation fluctuations. To facilitate spotting updraughts and downdraughts, the lower panel shows the oscillating part of the parcel's trajectory.

ration. To give us a sense of the breadth of the S_ℓ distribution, maximum values have been plotted as well. Since this distribution is nearly Gaussian (as we shall soon discuss), the figure shows that, for any chosen instant, there is a significant portion of the droplet population subject to positive supersaturation, despite the presence of ice crystals.

The distribution of S_ℓ is narrower for lower values of C_τ (see fig. 5.10b), as faster turbulent mixing tends to dampen out supersaturation fluctuations. This is particularly more observable before the parcel reaches LCL, since non-activated haze particles have limited influence on supersaturation. After activation, the distributions are narrowed because of activated droplets' tendency to drive S_ℓ towards zero, either by condensational growth or evaporation. In the oscillatory phase, σ_{S_ℓ} is maximum after downdraughts, when the liquid droplet concentration is smaller and thus the micro-physics is slower. Conversely, the maxima are reached just after updraughts, when the higher concentration of droplets leads to faster micro-physics.

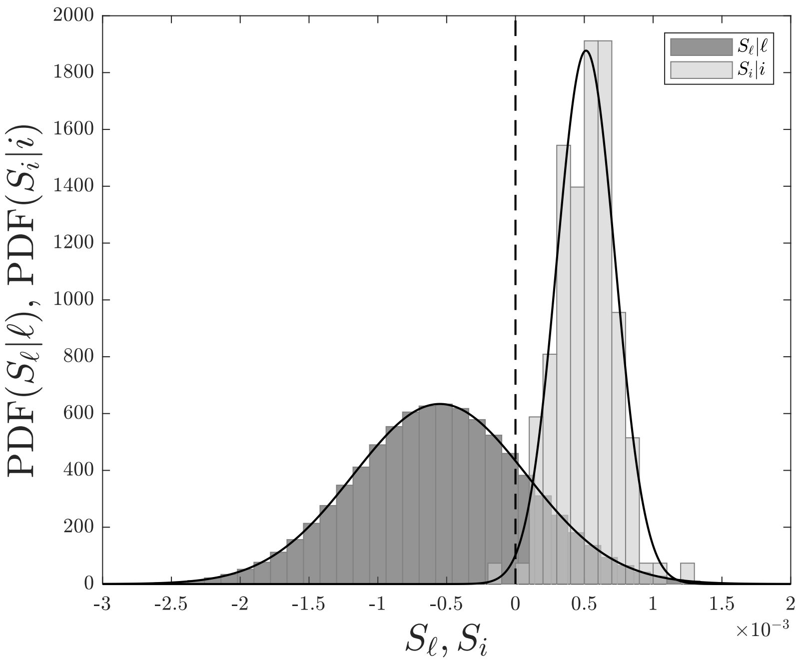

Figure 5.11: Conditional probability density functions of S_ℓ experienced by liquid droplets ($PDF(S_\ell|\ell)$), and S_i experienced by ice particles ($PDF(S_i|i)$) inside the stochastic parcel at a moment when $\langle S_\ell \rangle_\ell$ is locally minimum. The vertical dashed line indicates saturation, while the solid lines around the histograms correspond to the Gaussian distribution with the same mean and standard deviation. Although the condition in equation 5.20 for the Wegener–Bergeron–Findeisen process in the bulk applies, a significant part of the droplet population experiences positive supersaturation and grows.

By carefully inspecting figure 5.10 and comparing panels (a) and (c), one may notice that the height z and the oscillations in $\langle S_\ell \rangle$ and $\max(S_\ell)_\ell$ are approximately 90 degrees out of phase. This is even more noticeable in figure 5.9b. Mean saturation peaks and draughts closely follow the peaks and troughs in mean vertical velocity $\langle W \rangle$. This behaviour can be predicted from equation 4.22, which reads:

$$\frac{dS}{dt} = a\langle W \rangle - \frac{S}{\tau}. \tag{5.21}$$

This linearized equation represents a balance between the two main sources of change in supersaturation in the adiabatic parcel: Cooling and heating induced by the change in altitude under a hydrostatic pressure gradient, and condensational growth (or evaporation). Based on equation 5.21, the equilibrium supersaturation $S_{eq} = a\langle W \rangle \tau_s$ is directly proportional to the parcel's mean velocity. If we consider that $\langle W \rangle$ changes slowly compared to the phase relaxation time τ, then we may approximate $S(t)$ by a sequence of equilibrium states (quasi-equilibrium), where S(t) is proportional to $\langle W \rangle(t)$, a behaviour similar to the one observed in our simulations.

5.6 Probability Distributions of Supersaturation

One advantage of our stochastic model is that the distributions of supersaturation naturally arise from the microphysics. The probability distributions drawn in figure 5.11 are obtained at a local minimum of $\langle S_\ell \rangle_\ell$. In this scenario we have $\langle S_\ell \rangle_\ell < 0$ and $\langle S_i \rangle_i > 0$, which satisfy the conditions for the WBF mechanism in the stochastic framework. On average, water droplets are subject to a negative supersaturation, however the distribution of S_ℓ is sufficiently broad to enable a significant portion of the droplet population to experience condensational growth. Similarly, the ice particles are also subject to a range of saturation values, including negative ones. In fact, the entire $S_i|i$ distribution is drastically shifted towards zero in comparison to the homogeneous parcel, where $\langle S_i \rangle$ oscillates with great amplitude (see figure 5.9). As a result, we have an attenuated glaciation rate, causing liquid water to persist longer in the system. This scenario is impossible in the mean-field representation, where the homogeneous parcel model has only one value of $S_\ell < 0$ for all water droplets, i.e. the distribution is a Dirac's delta, which greatly accelerates the glaciation process.

The nearly Gaussian shapes of the distributions of $S_\ell|\ell$ and $S_i|i$ are ultimately connected to the Gaussianity of the velocity fluctuations w', imposed as an approximate distribution of turbulent velocity fluctuations. The temperature T and vapour concentration Q scalar fields are coupled to w' via the microphysics model and thus also present nearly Gaussian distributions, which are correlated due to latent heat. The actual shape of these distributions in clouds are not well established, however the near Gaussian assumption is reasonable in turbulent flows under certain conditions(Sreenivasan, 2019). Finally, supersaturation relates to T and Q through $S = Q/q_s(T) - 1$, where $q_s(T) \approx exp(-aT)$ where a is constant to good approximation (Rogers and Yau, 1989). Non-gaussianity in the distributions of $S_\ell|\ell$ and $S_i|i$ would arise from the non-linearity in $q_s(T)$ but is not noticeable due to the narrow range in temperatures, where $q_s(T)$ can be linearly approximated.

5.7 Long Term Cloud Particle Concentration

Next, we analyse the evolution of particle concentration in the oscillating parcel framework. Figure 5.12a shows the results for activated droplets. In both homogeneous and stochastic models, almost the totality of droplets are activated during the first updraught. In the homogeneous model, however, all of them evaporate during the first downdraught and remain deactivated for the remainder of the simulation. In the stochastic model, on the other hand, the population of activated droplets is very stable, with the activated fraction remaining above 99.75% at all times. This high proportion of activated droplets facilitates the recovery of liquid water fraction during updraughts, since for these droplets supersaturation does not need to rise above the critical value to reinitiate condensational growth. Additionally, we observe that droplet activation weakly depends on C_τ, with approximately the same amount of droplets activating after each cycle for all values simulated.

The evolution of ice crystal concentration, shown in figure 5.12b, is monotonic for all models. This because the mean temperature is always below 0 °C and melting is the only process in our model that could reduce the count of ice particles. In the stochastic model, melting could happen when $|\langle T \rangle - T_m| \approx \sigma_T$, in a *fluctuation-influenced* melting regime, where $T_m = 0$ °C. However, in our simulations temperature fluctuations are not sufficient to drive local values above the melting point. The growth in concentration observed between 0.5 and 1 hour of simulation is driven by the continuous decline of $\langle T \rangle$ as the parcel rises from ground level to the oscillating layer, which triggers the freezing of particles with progressively lower freezing temperatures. In the oscillating phase of the simulation, the homogeneous model displays a constant ice concentration due to its deterministic behaviour of the temperature field. In contrast, the stochastic model still exhibits occasional increases in ice concentration due to temperature fluctuations and to the fact that water droplets still experience supersaturation, which is one of the freezing conditions in our model (see eq. 4.32). An increased scalar mixing relaxation time (i.e. increased C_τ) leads to wider distributions of temperature and humidity, creating favourable conditions for more frequent freezing events.

5.8 Sensitivity Study

To better understand in which conditions the effects of unresolved-scale turbulence are most relevant, we have performed a sensitivity study. Here, we explore the model's parameter space to get a sense of which variables play an important role in the glaciation rate. In our setup, each simulation is assigned a set of values for mean vertical velocity $\langle W \rangle$, TKE dissipation rate ε, and ice particle concentration ϕ_i. The values used are described in table 5.1 under simulation group 3. The parcel is initialized above LCL and with liquid water fraction (μ) equal to unity. Liquid droplets start with a radius of 10 µm, while ICN particles start with zero ice mass. Additionally, freezing and melting are turned off. The parcel then proceeds with oscillatory motion in the cloud layer (or remains stationary, if $\langle W \rangle = 0$). Such initial conditions are designed to enable the observation of the glaciation rate due to the WBF mechanism.

We have considered five values for $\langle W \rangle$, two for ε, and four for ϕ_i, resulting in a total of 40 different simulations. Figure 5.13a shows the time evolution of the liquid water fraction for each of them. Ice concentration is indicated by line colours, and vertical velocity by line type. Stationary parcels are an exception to this rule, and are shown with solid black lines for easy distinction. Figure 5.13b shows the glaciation times, obtained from extrapolation of the black lines in panel (a). From these results it is evident that glaciation time is highly sensitive to the initial ice concentration, which can make it vary by several orders of magnitude. Higher ice concentration means a shorter ice phase relaxation time and thus its greater capacity to influence the bulk parcel saturation. Secondly comes the TKE dissipation rate, which expectedly produces faster glaciation rates when increased, as greater turbulence intensity accelerates the mixing process by which the ice and liquid phases exchange mass.

The results for variations in vertical velocity are perhaps the most interesting, as it becomes evident from figure 5.13a that W only momentarily affects μ, but does not significantly affect its long-term decay. This suggests that, for long-term mixed-phase persistence, the scalar variability produced by subgrid turbulence – by definition left unresolved in LES and other larger scale models – plays a larger role in the sustaining liquid water in mixed-phased clouds, when compared to cloud-scale convective motions.

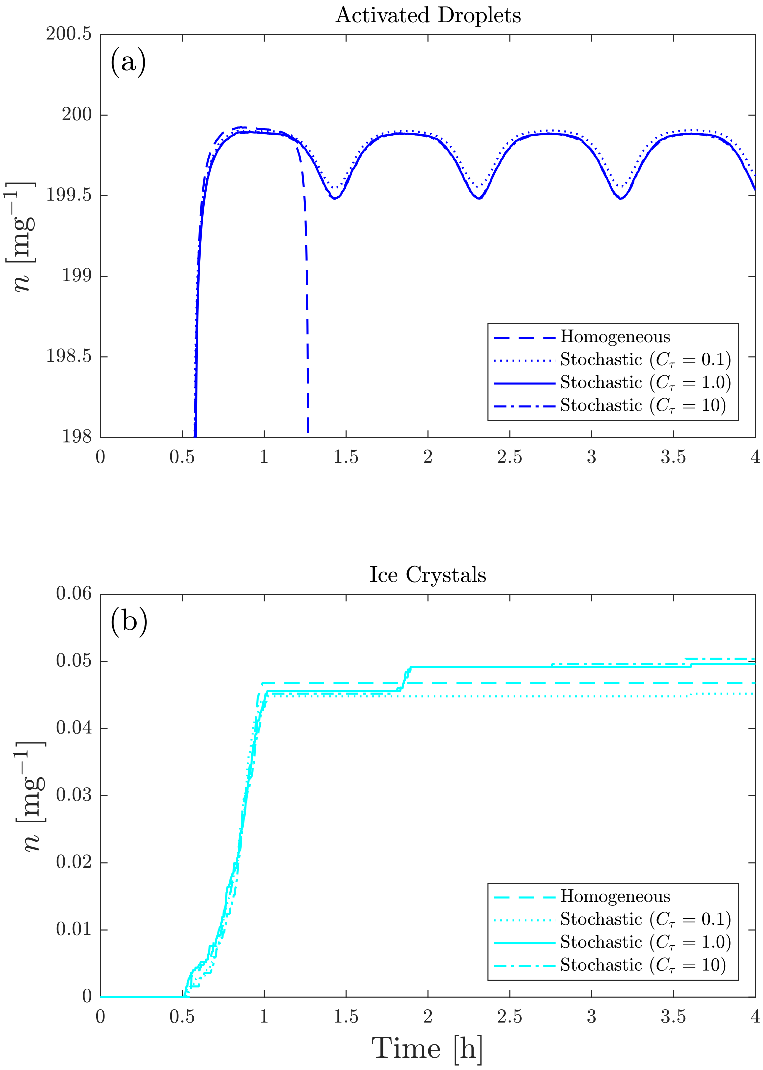

Figure 5.12: Particle concentration per milligram of dry air for mixed-phase cloud parcels (homogeneous and stochastic) in oscillatory motion: (a) concentration of water droplets; (b) concentration of ice crystals. The homogeneous model deactivates all droplets during the first downdraught, whereas in the stochastic model we observe the repeated reactivation of droplets during updraughts. Droplet freezing is more frequent in the stochastic parcel, because it permits that a population of droplets experiences non-negative supersaturation over liquid water, favouring ice nucleation.

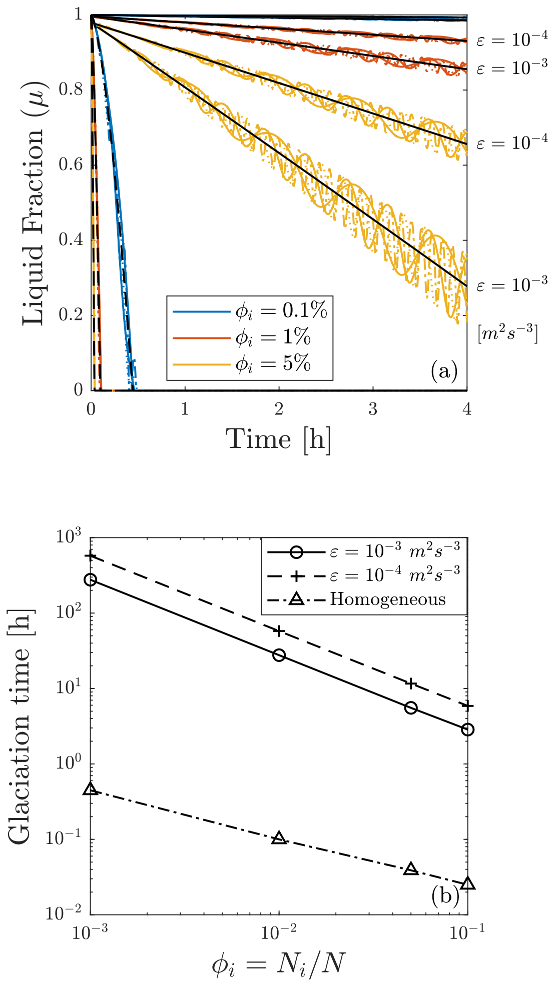

Figure 5.13: (a) Liquid water fraction evolution over time for different fractions ϕ_i of ice particles and different turbulent kinetic energy dissipation rates ε. All the curves to the left of the legend are for homogeneous cases. The black lines are plotted to guide the eye and correspond to non-oscillating parcels kept stationary at height $\bar{z}$. (b) Glaciation times as a function of the fraction of ice particles calculated from $\mu(t)$ from non-oscillating parcel simulations — the black lines of panel (a). Ice particle fraction ϕ_i has a strong influence on the glaciation rate, followed by the turbulent kinetic energy dissipation rate ε. The parcel oscillation period influences only the momentary values of liquid fraction, without significant influence on the total glaciation time.

6

Conclusions

This chapter synthesises the main findings of the thesis and places them in the broader context of cloud microphysics and turbulence. It highlights how the stochastic parcel framework advances our understanding of mixed-phase cloud resilience, revisits our refined criterion for the WBF process, and situates the model within a hierarchy of approaches. The discussion concludes with perspectives for applying this framework as a subgrid-scale scheme in larger-scale simulations.

6.1 Resilience of mixed-phase clouds through turbulent variability

In this work, we developed a stochastic microphysical model that accounts for the effects of inertial-range turbulence on the condensational growth of mixed-phase cloud particles. We have shown that accounting for the turbulent variability of temperature and water vapour – pronounced at the length scales unresolved in LES – can lead to significantly more persistent mixed-phase states compared to the standard mean-field approach. By representing the microphysics in a Lagrangian framework where each cloud particle experiences its own fluctuating growth history, our model mimics the effects of unresolved turbulence. In essence, a stochastic vertical velocity introduces random adiabatic cooling and warming for different particles, so that local temperature and vapour conditions vary from one particle to another. These local supersaturation conditions enable droplets and ice crystals to grow or evaporate at different rates. The interactions between particles and the environment – i.e., through latent heat and vapour exchange – influence primarily each particle's immediate surroundings, and propagate to other particles via a mixing model with its own characteristic timescale, tuned in accordance with inertial-range turbulence scaling laws.

In our stochastic parcel model, liquid droplet activation and growth become possible even when the mean supersaturation indicates subsaturation – as observed in cloud chamber measurements [Prabhakaran et al. (2020)] – meaning droplets can form and persist in conditions that a uniform model would deem unfavourable. As a result, our simulations show a more robust liquid phase, suggesting that the inclusion of variability and parameterised turbulence effects can significantly influence the glaciation rate by the Wegener-Bergeron-Findeisen (WBF) mechanism. The stochastic parcel maintains a long-lived mixed-phase state comprised predominantly of supercooled droplets, whereas an equivalent homogeneous parcel would rapidly lose all liquid water. This pronounced difference underscores how fluctuation-driven microphysics may prolong the coexistence of liquid and ice beyond the limits predicted by mean-field theory.

This finding stands in contrast to earlier descriptions of mixed-phase clouds that employed the mean-field assumption [Korolev and Mazin (2003); Korolev and Field (2008); Pinsky et al. 2014, 2015, 2018]. In homogeneous parcel models, liquid droplets and ice crystals are tightly coupled through a single supersaturation field, which tends to drive rapid WBF glaciation. Indeed, under mean-field conditions the persistence of supercooled liquid is found to require strong external forcing [Korolev and Field (2008); Pinsky et al. (2014)]. These formulations, however, do not include parcel size as an explicit parameter – effectively, one must assume that they *implicitly* simulate a volume of limited extent, so that the validity of the mean-field assumption is preserved. This suggests that their dynamical forcing thresholds for mixed-phase persistence should not be considered strict requirements for LES-scale mean flow.

The mean-field paradigm is physically realistic only for relatively small domains, where all particles share similar environmental conditions. In a larger cloud parcel (e.g. a typical LES grid box spanning tens of metres), turbulent motions prevent such homogeneity; updraughts and downdraughts within the volume create an intricate pattern of supersaturated and subsaturated regions. Consequently, even with a relatively weak overall updraught or oscillatory motion, parts of the parcel can sustain droplet growth while others allow vigorous ice growth. We have demonstrated that, under idealised conditions, a mixed-phase cloud parcel can maintain a persistent mixed-phase state without a strong mean updraught, provided that sufficient spatial variability of growth conditions is represented. In essence, what earlier models enforced through a bulk dynamical threshold *emerges naturally* in our stochastic model through the stochastic activation of droplets. Turbulent supersaturation fluctuations enable cloud droplets to nucleate and grow intermittently even in a mean-subsaturated environment, repeatedly renovating the liquid population. Our results indicate that the required dynamical forcing for liquid activation in the presence of ice can be produced by turbulent fluctuations under moderate mean updraughts. At the same time, it also indicates that these requirements might not be as strict as the mean-field theory suggests. The finite timescale imposed by turbulent mixing constrains the rate of vapour-mediated particle interactions, which implicates that local updraught requirements for liquid activation and growth are also less strict.

It should be emphasised that we do not claim that microphysics alone can indefinitely sustain mixed-phase clouds. In fact, this thesis focused on the dynamics of turbulent condensational growth, neglecting processes like collision-coalescence of droplets, aggregation of ice crystals, riming, and sedimentation. These simplifications were intended to isolate the effects of scalar fluctuations, on vapour-mediated interactions between ice and liquid water. Furthermore, the persistence of mixed-phase states in reality results from a complex interplay between microphysics and dynamics, and our results should be viewed within that broader context. Notably, "dynamics" in this discussion encompasses not only the mean updraught of the parcel but also the characteristics of the turbulent field. In our idealised simulations we assumed statistically stationary turbulence for simplicity, with a fixed intensity of fluctuations. Real clouds, on the other hand, may experience evolving turbulence intensity and intermittent bursts of mixing due to changing external conditions [Wacławczyk et al. (2022)]. Turbulence can be locally enhanced or dampened by processes like wind shear, buoyancy production, or energy dissipation. These temporal and spatial variations in turbulence will in turn modulate the microphysical interaction between liquid and ice. Thus, while our stochastic microphysics model represents a mechanism by which mixed-phase clouds can be more resilient than previously thought, it complements rather than negates the role of dynamical forcing. A sufficiently strong mean updraught or oscillation remains a clear path to sustain supercooled liquid in the presence of ice (as per earlier studies), but our results show that even in the absence of such forcing, turbulent fluctuations alone can maintain a long-lived mixed-phase balance.

6.2 A refined WBF criterion for stochastic mixed-phase clouds

A key theoretical insight of this work is a refined criterion for when the WBF process actively drives glaciation in a mixed-phase volume. We formulated this criterion in terms of conditional supersaturations, distinguishing the supersaturation felt by the liquid-water phase from that felt by the ice phase. In particular, we found that the persistence of a mixed-phase cloud is governed not by the grid-mean supersaturation alone, but by the condition that liquid water sees, on average, a subsaturated environment ($\langle S_\ell \rangle_\ell < 0$) while ice crystals see a supersaturated environment ($\langle S_i \rangle_i > 0$). In other words, within the cloud parcel, droplets on average experience conditions that favour evaporation, whereas ice crystals on average experience conditions that favour deposition growth. This dual condition is the essence of the WBF mechanism operating in a turbulent setting. Importantly, it is the conditional supersaturations $\langle S_\ell \rangle_\ell$ and $\langle S_i \rangle_i$ that govern the mixed-phase outcome, not the unconditional averages $\langle S_\ell \rangle$ and $\langle S_i \rangle$ that one would obtain in a homogeneous scenario.

Under mean-field assumptions, such a decoupling of supersaturation fields for liquid and ice is impossible – the model provides only a single uniform supersaturation at each moment. In a homogeneous parcel, $\langle S_\ell \rangle_\ell$ is identical to the overall $\langle S_\ell \rangle$, and if that mean becomes negative, *all* droplets evaporate simultaneously. Likewise, $\langle S_i \rangle$ is calculated based on the same temperature and vapour mixing ratio as $\langle S_\ell \rangle$, causing the ice phase to experience extremely high saturation values, and strongly intensifying the WBF process.

Mean-field models therefore cannot capture the scenario we observe in the stochastic model: a state where, within one parcel, droplets and ice effectively reside in *different saturation regimes*. This has important implications for interpreting both simulations and observations. For instance, a recent study by Khain et al. (2022) evaluated WBF activity in stratiform clouds by looking at the grid-mean supersaturation with respect to liquid and ice, that is, the unconditional averages $\langle S_\ell \rangle$ and $\langle S_i \rangle$. Because $\langle S_i \rangle$ can be regarded as a monotonic function of $\langle S_\ell \rangle$ in the mean-field approach, these criteria based on the unconditional averages are *not* independent – they are a single criterion, which effectively narrows the spectrum of circumstances in which a mixed-phase cloud can occur, for example, by denying the possibility of liquid water production in mean-subsaturated regimes.

We advocate that this approach may misdiagnose the cloud's state, since a negative $\langle S_\ell \rangle$ can hide the presence of pockets where $S_\ell > 0$. In our view, assessing the WBF process in a volume requires examining the conditional supersaturation averages and ensuring the criterion $\langle S_\ell \rangle_\ell < 0 < \langle S_i \rangle_i$ is met throughout the bulk of the volume. This insight is general and not limited to our particular model. However, conventional models lack a direct way to obtain $\langle S_\ell \rangle_\ell$ and $\langle S_i \rangle_i$ because they do not resolve subgrid variability, and there is no explicit relation between conditional and unconditional averages of supersaturations. The formulation of such a relation constitutes a formidable challenge for theoretical analysis. In this thesis, we sidestepped that difficulty by explicitly simulating the cloud's microscale variability. Our stochastic Lagrangian approach effectively provides a numerical closure for the conditional supersaturation problem, yielding physically consistent values of $\langle S_\ell \rangle_\ell$ and $\langle S_i \rangle_i$. This allowed us to interpret the model's mixed-phase stability in a more nuanced and physically transparent way than traditional bulk metrics.

Another merit of the stochastic model is that, by producing not just mean values but the full probability distributions of variables like supersaturation within the parcel, it offers further insight into the cloud's microphysical state. Notably, we found that under adverse conditions – for example, during a transient downdraught – the distribution of supersaturation over liquid water was broad enough to allow liquid activation and growth. In this particular setting, our criterion based on $\langle S_\ell \rangle_\ell$ and $\langle S_i \rangle_i$ indicates an active WBF mechanism, which is indeed observed by the momentary reduction of liquid water fraction (μ). However, the average glaciation rate is drastically reduced, with the liquid phase bifurcated into two coexisting groups: one that evaporates, while another grows inside supersaturated pockets. This concurrent growth and evaporation within the same parcel is a distinctive feature of our stochastic model. It explains, in part, the resilience of liquid water content in mixed-phase clouds by means of a weaker coupling between particles' growth conditions, mediated by turbulent mixing. In mixed-phase adiabatic parcel models, this paradigm is key to avoid the WBF collapse.

In addition to supporting droplet survival, turbulent fluctuations can also lead to enhanced ice formation, an aspect sometimes overlooked. In our simulations, the presence of fluctuations occasionally created conditions favourable for new ice nucleation that would not occur in a well-mixed parcel. For example, turbulent cooling spikes can locally drive the air to high supersaturation with respect to ice (or lower temperatures), activating additional ice nuclei, and further increasing the ice crystal number concentration. This stochastic ice activation provides a replenishing source of ice particles, which in a real cloud could influence longevity and precipitation. While increased ice crystal concentrations usually promote glaciation, in our stochastic system the simultaneous maintenance of liquid droplets means that the cloud can reach a new equilibrium with higher total particle counts of both phases. In other words, turbulence allows both more droplets and more ice crystals to form compared to a uniform scenario, leading to a richer microphysical state. Our model thus captures the dual role of fluctuations: they invigorate the liquid phase by intermittent droplet activation, and can also trigger ice phase initiation – via random nucleation events – beyond mean-field expectations. Together, these effects contribute to a more dynamic and stable mixed-phase cloud system, where the variability – created by turbulent velocity fluctuations and preserved by the finite mixing timescale – acts as a buffering mechanism. It dampens the unstable tendency of WBF glaciation, preventing abrupt collapse, and instead holding the system in a quasi-steady coexistence of phases.

6.3 Contribution within the hierarchy of cloud models

The notion of a model hierarchy, as discussed by Held (2005), underscores the value of constructing models with varying levels of complexity to better understand how physical processes influence system behaviour. Rather than relying solely on highly detailed simulations or overly simplified conceptual models, the goal is to establish intermediate steps that isolate key sources of complexity in a controlled way. These intermediate models, situated between comprehensive simulations and idealised theories, serve as stepping stones that clarify how model outcomes evolve as physical realism is incrementally added. Our stochastic parcel model fits into this philosophy, offering a structured way to interrogate the microphysical consequences of turbulence without the full burden of DNS.

The stochastic Lagrangian parcel model presented here can be viewed as a tool that bridges the gap between direct numerical simulation (DNS) and large-eddy simulation (LES) in the cloud model hierarchy. It is more sophisticated than oversimplified bulk schemes (which assume complete homogeneity), yet it is far less computationally intensive than explicit DNS, which resolves every eddy down to Kolmogorov scale. In the sense of Held (2005), our approach contributes to a hierarchy of models for mixed-phase cloud microphysics. At one end of this hierarchy, traditional bulk schemes focus on large-scale motions and scalar advection, treating a grid box as a single uniform parcel and thus leaving the interactions between microphysical processes and subgrid fluctuations unresolved. At the other end, DNS and laboratory experiments attempt to resolve or observe the detailed turbulence-microphysics interactions directly [Vaillancourt et al. (2001); Desai et al. (2019); Thomas et al. (2020)]. Our model occupies the in-between regime: it parameterises the effects of subgrid turbulence on scalar mixing and particle growth, capturing some of the stochastic variability that a coarse model would miss, but without resolving every tiny eddy as DNS would. By doing so, it offers new insight into how inertial-range turbulence (eddies on scales smaller than an LES grid, yet larger than the Kolmogorov microscale) influences cloud microphysics. For instance, our results demonstrated that eddies in this intermediate range can facilitate droplet activation and modulate the WBF process by sustaining pockets of vapour that allow droplets to persist. These are effects that a typical LES would not reproduce unless a subgrid scheme accounts for them. In this sense, our stochastic Lagrangian microphysical model provides a framework to translate the effects of unresolved turbulence on cloud microphysics into useful information that is accessible at larger model scales. It does so without incurring the prohibitive cost of DNS, while at the same time avoiding the excessive simplifications inherent in bulk mean-field schemes.

6.4 Outlook: Towards subgrid-scale cloud parametrisation

Beyond its standalone insights, our stochastic parcel model can serve as a basis for a subgrid-scale (SGS) microphysics scheme in larger-scale atmospheric models. Modern LES and cloud-resolving models typically grid-average their microphysics, meaning they assume each grid cell is internally homogeneous aside from what a diagnostic variability scheme might impose. Our results make the case that a prognostic Lagrangian SGS approach can fundamentally improve the representation of mixed-phase cloud processes. Instead of relying on explicit strong updraughts or continuously lifting to sustain liquid water, a stochastic SGS scheme would allow each grid box to maintain its own cloud variability, generating and preserving supercooled liquid through subgrid fluctuations and turbulent mixing. This is an attractive alternative to earlier "diagnostic" mixed-phase schemes [Field et al. (2014); Furtado et al. (2016)] which imposed fluctuations to mimic turbulence, while assuming microphysical homogeneity within sub-parcels with no inter-parcel mixing mechanism. Those schemes essentially treated a grid box as an ensemble of small homogeneous parcels [Furtado (2018)]. In such formulations, all particles in a given sub-parcel would share the same growth conditions, and respond in unison to fluctuations in the parcel-mean supersaturation. Thus, water activation is again constrained to happen only in the parcels that attain enough vertical velocity to compensate the presence of ice. Paradoxically, these models represent an ensemble of microphysical states where each one of them is constrained by the homogeneity assumption, forcing the liquid and ice phases to grow under the same conditions.

By contrast, our Lagrangian scheme represents a grid box as an ensemble of individual *droplets and ice crystals*, each interacting with an evolving grid-mean environment, but also carrying its own history of supersaturation exposure. This particle-based approach inherently captures the effects of subgrid spatial inhomogeneities on particle growth. By providing each particle with its own local environment and allowing them to interact only via a turbulent mixing model, we limit water-ice interactions to a physically-based timescale, compatible with the grid's size and turbulence intensity. Hence, the proposed formulation offers a means to improve the simulated longevity and phase mix of clouds in LES or climate models, which currently struggle to keep supercooled liquid water from being prematurely eliminated.

Implementing the stochastic Lagrangian microphysics as an LES subgrid scheme will require careful consideration of numerical and computational aspects, but it offers clear advantages. One advantage is the modularity of the mixing model. In our implementation, we used a simple mixing parameterisation (the IEM model, Interaction by Exchange with the Mean) characterised by a single timescale for turbulent mixing of scalars. This simplified mixing model is deterministic, but captures some integral properties of turbulent diffusion and stirring. We chose the IEM scheme for its numerical efficiency and clarity, but it is by no means the only choice. Other stochastic mixing models – such as the binomial Langevin model or the bounded Langevin model [Dopazo (1994); Pozorski and Wacławczyk (2020)] – offer different representations of turbulent eddy mixing and can be explored in future work. The modular design of our framework allows us to include these alternative models for the evolution of temperature and vapour fluctuations without altering the rest of the microphysics solver. This flexibility means we can progressively improve the fidelity of the turbulence representation (for example, including intermittency or multiple time scale eddies) and examine how it impacts cloud microphysical outcomes. We regard our turbulent mixing model as one of intermediate complexity: it lies between the oversimplified mean-field approach and more complex models like the linear-eddy model (LEM) employed by Hoffmann (2020). The LEM explicitly simulates 1-D turbulent advection and molecular diffusion of scalars by continuously rearranging an artificial 1-D scalar profile [Kerstein (1988)]. Hoffmann's mixed-phase LEM study showed that introducing 1-D inhomogeneities can delay the WBF-induced glaciation by limiting the vapour competition between droplets and ice. Our simpler stochastic model, while not resolving a spatial profile, also quantifies the effect of delayed glaciation through variability, even in scenarios with abundant ice. This agreement across models of different complexity builds confidence in the underlying physics: turbulent fluctuations tend to counteract the WBF-driven bias toward glaciation. Together with DNS and LEM results, our study helps establish a more complete picture of mixed-phase cloud physics across scales. In the future, continued DNS studies [Vaillancourt et al. (2001); Thomas et al. (2020)] and targeted laboratory experiments [e.g. Desai et al. (2019)] will be invaluable to constrain and validate stochastic microphysics models like ours. Such data can guide the choice of mixing parameters and ensure that the variability simulated in the model reflects real atmospheric turbulence statistics.

Despite the many avenues for further development, the core findings of our study are robust and carry important implications for atmospheric modelling. We expect that these conclusions remain valid in more elaborate scenarios as well. For example, if we relaxed the assumption of spherical particles: in reality, ice crystals often have non-spherical habits (plates, columns, dendrites, etc.) which have a higher surface-area-to-mass ratio and hence larger capacitance than equal-volume spheres. These shapes enable faster vapour deposition, so one would anticipate that including non-spherical ice would make a mixed-phase cloud less persistent (all else kept constant) because ice particles would consume vapour and reduce supersaturation more efficiently. Indeed, our idealised results for spherical ice likely represent a best-case scenario for liquid water retention. However, even if ice crystals grow faster, the fundamental benefit of variability should persist – the stochastic parcel would still retain more liquid than a homogeneous parcel under the same conditions. In other words, the baseline glaciation timescale might shorten with more efficient ice growth, but the ratio of timescales (stochastic vs. homogeneous) would still favour the stochastic model. This thought experiment is consistent with our main point: a reference mixed-phase state (for a given liquid fraction and ice number) will always be more resilient to WBF glaciation when internal fluctuations are represented.

Finally, it bears repeating that clouds, and mixed-phase clouds in particular, are a notoriously challenging regime for weather and climate models, and misrepresentations of these clouds lead to significant errors in simulated radiation and precipitation [Cesana et al. (2012); Tan et al. (2016); Furtado et al. (2016)]. The traditional approach of enforcing an external dynamic threshold to sustain liquid water hints at a gap in our modelling of cloud physics. This thesis contributes a novel approach to fill that gap by embedding stochastic microphysics within a Lagrangian framework, thus explicitly acknowledging and simulating the variability that real clouds possess. The insights gained here – such as the importance of conditional saturation balance ($\langle S_\ell \rangle_\ell$ vs $\langle S_i \rangle_i$) and the distribution-wide view of cloud states – can inform how we design the next generation of cloud parameterisations. We have demonstrated the potential for a prognostic subgrid scheme that does not rely on tuning mean updraughts to counteract biases, but instead uses physically-based fluctuations to achieve a long-lived mixed-phase condition. Moving forward, testing this approach in an actual LES setup will be an important step. By coupling our stochastic microphysics scheme to an LES and comparing the outcomes against observations or high-resolution simulations, one can assess its practical benefits for cloud forecasting. We are optimistic that such a scheme, once refined, will improve the fidelity of simulations of mixed-phase clouds, thereby enhancing our overall understanding of cloud-climate feedbacks.

In summary, this work places a spotlight on the critical role of variability in cloud microphysics. Through an idealised yet insightful model, we have shown how stochastic fluctuations in a cloud's thermodynamic conditions can fundamentally alter its microphysical trajectory – keeping clouds mixed-phase longer, against the odds set by simple theory. These findings underscore that to accurately predict cloud behaviour (and ultimately climate effects), models must move beyond the mean-field mindset. By embracing a stochastic, particle-based approach, we take a substantial step towards cloud models that are both more realistic and more predictive of the rich phenomena observed in nature. The methodologies and results presented in this thesis lay the groundwork for more advanced subgrid cloud schemes and highlight the fertile intersection between turbulence and cloud microphysics, inviting further exploration in both modelling and experimental studies.

References

Abade, G. C. (2025). On idealized models of turbulent condensation in clouds. *J. Atmos. Sci.*, 82(8). 44, 46, 50

Abade, G. C. and Albuquerque, D. G. (2024). Persistent mixed-phase states in adiabatic cloud parcels under idealised conditions. *Quart. J. Roy. Meteor. Soc.*, 150(763):3450–3474. 8, 43

Abade, G. C., Grabowski, W. W., and Pawlowska, H. (2018). Broadening of cloud droplet spectra through eddy hopping: turbulent entrainment parcel simulations. *J. Atmos. Sci.*, 75:3365–3379. 7, 29, 30

Batchelor, G. K. (1959). Small-scale variation of convected quantities like temperature in turbulent fluid part 1. general discussion and the case of small conductivity. *Journal of Fluid Mechanics*, 5(1):113–133. 44

Bauer, P., Thorpe, A., and Brunet, G. (2015). The quiet revolution of numerical weather prediction. *Nature*, 525(7567):47–55. 45

Bergeron, T. (1935). On the physics of clouds and precipitation. *In: Proc. Ve Assemblée Générale de l'Union Géodésique et Geophysique Internationale, Lisbon, Portugal, International Union of Geodesy and Geophysics*, pages 156–180. 3, 38

Boucher, O., Randall, D., Artaxo, P., Bretherton, C., Feingold, G., Forster, P., Kerminen, V.-M., Kondo, Y., Liao, H., and Lohmann, U. (2013). Clouds and aerosols. in: Climate change 2013: The physical science basis. contribution of working group i to the fifth assessment report of the intergovernmental panel on climate change. Technical report, Cambridge University Press, Cambridge. 1, 3

Cesana, G., Kay, J. E., Chepfer, H., English, J. M., and de Boer, G. (2012). Ubiquitous low-level liquid-containing arctic clouds: New observations and climate model constraints from calipso-goccp. *Geophys. Res. Lett.*, 39:L20804. 2, 3, 43, 81

Cui, Z., Carslaw, K., Yin, Y., and Davies, S. (2006). A numerical study of aerosol effects on the dynamics and microphysics of a deep convective cloud in a continental environment. *J. Geophys. Res.-Atmos.*, 111. 36

de Boer, G., Morrison, H., Shupe, M., and Hildner, R. (2011). Evidence of liquid dependent ice nucleation in high-latitude stratiform clouds from surface remote sensors. *Geophys. Res. Lett.*, 38:L01803. 36

Desai, N., Chandrakar, K. K., Kinney, G., Cantrell, W., and Shaw, R. A. (2019). Aerosol-mediated glaciation of mixed-phase clouds: Steady-state laboratory measurements. *Geophysical Research Letters*, 46(15):9154–9162. 78, 80

Dopazo, C. (1994). Recent developments in PDF methods. In Libby, P. and Williams, F. A., editors, *Turbulent reacting flows*, pages 375–474. Academic, New York. 80

Einstein, A. (1905). Über die von der molekularkinetischen theorie der wärme geforderte bewegung von in ruhenden flüssigkeiten suspendierten teilchen. *Annalen der Physik*, 322(8):549–560. 50

Field, P. R., Hill, A. A., Furtado, K., Korolev, A., and Shipway, B. J. (2014). Mixed-phase clouds in a turbulent environment. part 2: Stochastic subgrid parameterization. *J. of Adv. in Mod. Earth Sys.*, 6:1160–1174. 6, 79

Findeisen, W. (1938). Kolloid-meteorologische vorgänge bei neiderschlagsbildung. *Meteorol. Z.*, 55:121–133. 3, 38

Fridlind, A. M., van Diedenhoven, B., Ackerman, A. S., Avramov, A., Mrowiec, A., Morrison, H., Zuidema, P., and Shupe, M. D. (2012). A fire-ace/sheba case study of mixed-phase arctic boundary layer clouds: Entrainment rate limitations on rapid primary ice nucleation processes. *J. Atmos. Sci.*, 69(1):365 – 389. 4

Furtado, K. (2018). Subgrid representation of mixed-phase clouds in a general circulation model. In Andronache, C., editor, *Mixed-Phase Clouds*, pages 185–214. Elsevier. 2, 3, 41, 43, 79

Furtado, K., Field, P. R., Boutle, I. A., Morcrette, C. J., and Wilkinson, J. M. (2016). A physically based subgrid parametrization for the production and maintenance of mixed-phase clouds in a general circulation model. *J. Atmos. Sci.*, 73:279–291. 6, 79, 81

Grabowski, W. W. and Abade, G. C. (2017). Broadening of cloud droplet spectra through eddy hopping: Turbulent adiabatic parcel simulations. *J. Atmos. Sci.*, 74:1485–1493. 7

Grabowski, W. W. and Smolarkiewicz, P. K. (1990). Monotone finite-difference approximations to the advection-condensation problem. *Monthly Weather Review*, 118(10):2082 – 2098. 17

Haworth, D. C. and Pope, S. B. (2011). Transported probability density function methods for reynolds-averaged and large-eddy simulations. In Echekki, T. and Mastorakos, E., editors, *Turbulent Combustion Modeling*, chapter 6, pages 119–142. Springer. 49

Held, I. M. (2005). The gap between simulation and understanding in climate modeling. *Bulletin of the American Meteorological Society*, 86(11):1609 – 1614. 78

Heymsfield, A. J. (1977). Precipitation development in stratiform ice clouds: A microphysical and dynamical study. *J. Atmos. Sci.*, 34(2):367 – 381. 4, 56

Hoffmann, F. (2020). Effects of entrainment and mixing on the wegener–bergeron–findeisen process. *J. Atmos. Sci.*, 77:2279–2296. 6, 80

Kalnay, E. (2002). *Atmospheric Modeling, Data Assimilation and Predictability*. Cambridge University Press. 45, 46

Kaul, C. M., Teixeira, J., and Suzuki, K. (2015). Sensitivities in large-eddy simulations of mixed-phase arctic stratocumulus clouds using a simple microphysics approach. *Mon. Wea. Rev.*, 143(11):4393–4421. 7, 8, 21, 22

Kerstein, A. R. (1988). A linear-eddy model of turbulent scalar transport and mixing. *Combustion Science and Technology*, 60(4-6):391–421. 6, 80

Khain, A., Phillips, V. T. J., Ilotoviz, E., Prabhakaran, T., and Ryzhkov, A. (2022). On the role of large eddies in mixed-phase stratiform clouds. *J. Atmos. Sci.*, 79(1):151–171. 76

Korolev, A. and Field, P. R. (2008). The effect of dynamics on mixed-phase clouds: Theoretical considerations. *J. Atmos. Sci.*, 65(1). 5, 6, 9, 44, 74

Korolev, A. and Mazin, I. (2003). Supersaturation of water vapor in clouds. *J. Atmos. Sci.*, 60(24):2957–2974. 4, 7, 8, 9, 44, 56, 74

Korolev, A., McFarquhar, G., Field, P. R., Franklin, C., Lawson, P., Wang, Z., Williams, E., Abel, S. J., Axisa, D., Borrmann, S., Crosier, J., Fugal, J., Krämer, M., Lohmann, U., Schlenczek, O., Schnaiter, M., and Wendisch, M. (2017). Mixed-phase clouds: Progress and challenges. *Meteor. Monogr.*, 58:5.1–5.50. 6

Köhler, H. (1936). The nucleus in and growth of hygroscopic droplets. *Transactions of the Faraday Society*, 32:1152–1161. 28

Lam, R., Sanchez-Gonzalez, A., Willson, M., Wirnsberger, P., Fortunato, M., Alet, F., Ravuri, S., Ewalds, T., Eaton-Rosen, Z., Hu, W., Merose, A., Hoyer, S., Holland, G., Vinyals, O., Stott, J., Pritzel, A., Mohamed, S., and Battaglia, P. (2023). Learning skillful medium-range global weather forecasting. *Science*, 382(6677):1416–1421. 45, 46

Lozar, A. d. and Mellado, J. P. (2014). Cloud droplets in a bulk formulation and its application to buoyancy reversal instability. *Quarterly Journal of the Royal Meteorological Society*, 140(682):1493–1504. 17, 49

McCoy, D. T., Hartmann, D. L., Zelinka, M. D., Ceppi, P., and Grosvenor, D. P. (2014). Mixed-phase cloud physics and southern ocean cloud feedback in climate models. *Nature Geoscience*, 7:620–624. 2, 3

Niemand, M., Möhler, O., Vogel, B., Vogel, H., Hoose, C., Connolly, P., Klein, H., Bingemer, H., DeMott, P., Skrotzki, J., and Leisner, T. (2012). A particle-surface-area-based parameterization of immersion freezing on desert dust particles. *J. Atmos. Sci.*, 69(10):3077 – 3092. 37

Petters, M. and Kreidenweis, S. (2007). A single parameter representation of hygroscopic growth and cloud condensation nucleus activity. *Atmos. Chem. Phys.*, 7:1961. 28

Pinsky, M., Khain, A., and Korolev, A. (2014). Analytical investigation of glaciation time in mixed-phase adiabatic cloud volumes. *J. Atmos. Sci.*, 71(11):4143 – 4157. 5, 7, 8, 9, 44, 74

Pinsky, M., Khain, A., and Korolev, A. (2015). Phase transformations in an ascending adiabatic mixed-phase cloud volume. *J. Geophys. Res.: Atmospheres*, 120(8):3329–3353. 5, 7, 8, 9, 44, 74

Pinsky, M., Khain, A., and Korolev, A. (2018). Theoretical analysis of liquid–ice interaction in the unsaturated environment with application to the problem of homogeneous mixing. *J. Atmos. Sci.*, 75(4):1045 – 1062. 5, 7, 8, 9, 44, 74

Pinsky, M., Magaritz, L., Khain, A., Krasnov, O., and Sterkin, A. (2008). Investigation of droplet size distributions and drizzle forma- tion using a new trajectory ensemble model. Part I: Model description and first results in a nonmixing limit. *J. Atmos. Sci.*, 65:2064–2086. 49

Pope, S. (2000). *Turbulent Flows*. Cambridge University Press, Cambridge. 47

Pope, S. B. (1985). PDF methods for turbulent reactive flows. *Prog. Energy Combust. Sci.*, 11:119–192. 7

Pozorski, J. and Wacławczyk, M. (2020). Mixing in turbulent flows: An overview of physics and modelling. *Processes*, 8(11):1379. 80

Prabhakaran, P., Shawon, A., Kinney, G., Thomas, S., Cantrell, W., and Shaw, R. (2020). The role of turbulent fluctuations in aerosol activation and cloud formation. *Proc. Natl. Acad. Sci. (USA)*, 117(29):16831–16838. 58, 59, 74

Pruppacher, H. R. and Klett, J. D. (1997). *Microphysics of Clouds and Precipitation*. Kluwer Acad. 35

Raoult, F.-M. (1882). Loi générale des tensions de vapeur des dissolvants. *C. R. Acad. Sci. Paris*, 94:1030–1033. 27

Rogers, R. R. and Yau, M. K. (1989). *A short course in cloud physics*. Butterworth-Heinemann. 14, 27, 31, 34, 68

Sardina, G., Picano, F., L., B., and Caballero, R. (2015). Continuous growth of droplet size variance due to condensation in turbulent clouds. *Phys. Rev. Lett.*, 115:184501. 7

Sardina, G., Poulain, S., L., B., and Caballero, R. (2018). Broadening of cloud droplet size spectra by stochastic condensation: effects of mean updraft velocity and CCN activation. *J. Atmos. Sci.*, 75:451–467. 7

Seidel, J. S., Kiselev, A. A., Keinert, A., Stratmann, F., Leisner, T., and Hartmann, S. (2024). Secondary ice production – no evidence of efficient rime-splintering mechanism. *Atmos. Chem. Phys.*, 24(9):5247–5263. 36

Shima, S., Kusano, K., Kawano, A., Sugiyama, T., and Kawahara, S. (2009). The super-droplet method for the numerical simulation of clouds and precipitation: A particle-based and probabilistic microphysics model coupled with a non-hydrostatic model. *Q. J. R. Meteorol. Soc.*, 135:1307–1320. 26, 32

Shima, S., Sato, Y., Hashimoto, A., and Misumi, R. (2020). Predicting the morphology of ice particles in deep convection using the super-droplet method: development and evaluation of scale-sdm 0.2.5-2.2.0, -2.2.1, and -2.2.2. *Geoscientific Model Development*, 13(9):4107–4157. 37

Shupe, M. D., Matrosov, S. Y., and Uttal, T. (2006). Arctic mixed-phase cloud properties derived from surface-based sensors at sheba. *J. Atmos. Sci.*, 63(2):697 – 711. 4

Squires, P. (1952). The growth of cloud drops by condensation. part i. general characteristics. *Australian Journal of Scientific Research. Series A: Physical Sciences*, 5(1):59–86. 33

Sreenivasan, K. (2019). Turbulent mixing: a perspective. *Proceedings of the National Academy of Sciences*, 116(37):18175–18183. 68

Storelvmo, T. (2017). Aerosol effects on climate via mixed-phase and ice clouds. *Annual Rev. of Earth and Planetary Sci.*, 45:199–222. 2, 3

Sze, W.-P., Tang, S.-C., Cheung, C.-C., and Tam, C.-Y. (2022). Numerical weather prediction at 200 m local resolution based on an unstructured grid global model. *Earth and Space Science*, 9(10):e2022EA002342. 46

Tan, I., Storelvmo, T., and Zelinka, M. (2016). Observational constraints on mixed-phase clouds imply higher climate sensitivity. *Science*, 352. 2, 3, 81

Thomas, L., Grabowski, W. W., and Kumar, B. (2020). Diffusional growth of cloud droplets in homogeneous isotropic turbulence: DNS, scaled-up DNS, and stochastic model. *Atmos. Chem. Phys.*, 20(14):9087–9100. 78, 80

Thomson, W. (1871). Lx. on the equilibrium of vapour at a curved surface of liquid. *Philos. Mag. Ser. 4*, 42(282):448–452. 27

Tripoli, G. J. and Cotton, W. R. (1981). The use of ice-liquid water potential temperature as a thermodynamic variable in deep atmospheric models. *Mon. Wea. Rev.*, 109:1094–1102. 21

Ueda, S., Miura, K., Kawata, R., Furutani, H., Uematsu, M., Omori, Y., and Tanimoto, H. (2016). Number-size distribution of aerosol particles and new particle formation events in tropical and subtropical pacific oceans. *Atmospheric Environment*, 142:324–339. xi, 30, 31

Vaillancourt, P. A., Yau, M. K., and Grabowski, W. W. (2001). Microscopic approach to cloud droplet growth by condensation. Part I: Model description and results without turbulence. *J. Atmos. Sci.*, 58:1945–1964. 46, 78, 80

Van Kampen, N. G. (2007). *Stochastic processes in physics and chemistry*. Elsevier. 49

Wacławczyk, M., Nowak, J. L., Siebert, H., and Malinowski, S. P. (2022). Detecting nonequilibrium states in atmospheric turbulence. *J. Atmos. Sci.*, 79(10):2757 – 2772. 75

Wegener, A. (1911). Thermodynamik der atmosph. *Verlag Von Johann Ambrosius Barth, Leipzig 331 pp. (in German).* 3, 38

Zhang, D., Wang, Z., Kollias, P., Vogelmann, A. M., Yang, K., and Luo, T. (2018). Ice particle production in mid-level stratiform mixed-phase clouds observed with collocated a-train measurements. *Atmos. Chem. Phys.*, 18(6):4317–4327. 4